ENERGY-EFFICIENT LARGE MEDIUM-SPEED CATAMARANS: HULL FORM DESIGN BY FULL-SCALE CFD SIMULATIONS

by

Max Haase
Dipl-Ing (University of Rostock)

National Centre for Maritime Engineering and Hydrodynamics
Australian Maritime College

Submitted in fulfilment of the requirements
for the Degree of Doctor of Philosophy

Academic supervision:
A/Prof Jonathan Binns
Prof Giles Thomas
Prof Neil Bose

University of Tasmania
May, 2015

I declare that this thesis contains no material which has been accepted for a degree or diploma by the University or any other institution, except by way of background information and duly acknowledged in the thesis, and that, to the best of my knowledge and belief, this thesis contains no material previously published or written by another person, except where due acknowledgement is made in the text of the thesis.

Signed: _____

Date: 09/10/2015

Signed: _____

Date: 09/10/2015

"It is the direction and not the magnitude which is to be taken into consideration."
Thomas Paine (1737-1809)

ABSTRACT

Large medium-speed catamarans are currently under development as a new class of vessel for economically efficient and more environmentally sustainable fast sea transportation. Their design is based on current high-speed catamarans, to adopt advantages such as large deck areas and low wave-making resistance, but they will operate at lower speeds and carry a higher deadweight to obtain higher transport efficiency. They operate at speeds around the main drag hump, where the wave-making drag coefficient is at its maximum. Hence this speed range is usually avoided by boat designers no precise guidelines for hull form design of large medium-speed catamarans are present to operate efficiently in this generally unfavourable speed spectrum.

Literature has been surveyed to derive hull form parameters that provide low drag for monohulls and catamaran vessels. Based on these findings a hull form family was developed with demihull slenderness ratios ranging from 9 to 15 and the hydrodynamic performance was evaluated at Froude numbers from 0.25 up to 0.49 to derive design parameters with the lowest drag and highest transport efficiency. These parameters corresponds to vessel sizes from 110 m to 190 m and speeds of 16 to 41 knots. A novel CFD-based approach has been developed to provide more accuracy to the final drag prediction at full scale. It was verified using results of model scale experiments of a 98 m and a 130 m catamaran and validated with results obtained from sea trial measurements, in deep as well as in shallow water. Furthermore, its capability to replicate the flow past a typical deep partially ventilated transom has been investigated using model scale experiments. The key advantage of this method is that the same computational mesh can be used for model-scale verification and full-scale predictions.

The computational full-scale simulation approach was found to be capable of predicting the drag force within 5% of results derived from full-scale measurements and extrapolated model test data. In addition it has been shown to correctly predict steady and unsteady shallow water effects. Also the ventilation process of the transom stern has been experimentally validated and the flow feature in the stagnant zone past the partially ventilated transom was identified as a non-shedding squashed horseshoe vortex. The lowest drag can be achieved for

catamarans with demihull slenderness ratios of 11 to 13 and hulls of 150 m in length provided highest transport efficiency for speeds of 20 to 35 knots at a light displacement, and 170 m and 190 m for a medium and a heavy displacement respectively.

Finally, when comparing the results to contemporary large and fast catamarans carrying equivalent deadweight and travelling at the same speed, fuel savings up to 40% can be achieved if a hull of 150 m instead of 110 m length is used. This demonstrates that large-medium catamarans have the potential to be a fuel-efficient alternative for a successful future of fast sea transportation.

ACKNOWLEDGEMENTS

With immense pride I would like to express my gratitude to everyone who has supported me during the course of this study and made this thesis happen. In particular I want to acknowledge the contributions of:

My supervisors: I want to thank you for giving me this exceptional opportunity to undertake this research. It has been challenging and enjoyable to work on such vessels in such a fantastic study environment. I will never forget your tireless advice during the course of this research, it has been a great pleasure to study under your guidance. You have not only been supervisors, but friends. Giles, Binnsie and Neil, thank you very much for this priceless experience.

Gary Davidson and Stuart Friezer: It has been brilliant to have you aboard this research project. I am grateful for your valuable feedback from the boat designer's perspective. Your advice has given this study its practical relevance.

Rebecca: Please, forgive for the late letting-you-know about my plans of moving to Tasmania, I promise to let you choose our next destination. I love you for being with me on this little island, for having a home far away from home, and for much, much else.

Konrad and Iwan: Thank you very much for sharing this special experience, it has been a pleasure to work with you on this project as research fellows and as friends. All the best to you for the time after graduation!

My RHD Hub Fellows: Many thanks for the great company during these years of research and for the lively discussions on numerical simulations and life to: Ahmed Swidan, Alan Belle, Alex Briggs, Alex Conway, Chris Polis, Jalal Rafiesharaki, Leong, Louciano Mason, Mahdi Ghiji, Mohammadreza Javanmadi, Philip Marsh, and Rahman Rahimi. Not less I want to thank all my friends that made the hub life special: Cecile L'Hermitte, Chris Mabin, Hadi Ghaderi, Mahinda Bandara, and Martin Grünenwald. Fingers crossed I have not forgotten anyone.

The AMC Towing Tank: I would like to thank Tim for providing data and advice, Kirk for his efforts to help turning a Roger Whittaker tape into a scientific flow visualisation device, and Liam for his technical support. There is no proper ship hydrodynamics research without towing tank experiments!

TPAC: Without the *Tasmanian Partnership of Advanced Computing* all this number crunching would not have been possible. A warm thanks to Matt Armsby and Kym Hill for their support to keep the supercomputer up and running.

The Hydrodynamics Specialists: I also want to thank Prof Lawrence Doctors, Prof Michael Davis and Prof Kevin Maki for their priceless feedback on parts of this research.

My Parents: Last but not least I want to thank my parents Ronald and Sybille for their enduring love and support during the last 32 years.

Contents

Contents **i**

List of Tables **vii**

List of Figures **ix**

Nomenclature **xvii**

1 Introduction **1**

1.1 Current Large Catamarans 1

1.2 Fuel Consumption and Transport Efficiency 2

1.3 Speed Regimes 3

1.3.1 Low-speed Regime 3

1.3.2 Medium-speed Regime 3

1.3.3 High-speed Regime 3

1.4 Current State of Knowledge 4

1.4.1 Catamaran Design for Medium Speeds 4

1.4.2 Studies on Catamaran Design Parameters 5

1.4.3 Resistance Prediction Tools 6

1.5 Research Objectives 7

1.6 Thesis Layout 8

1.7 Contribution to Contemporary Ship Hydrodynamics 10

1.8 Statement of Contribution 11
1.8.1 Candidate's Responsibility 11
1.8.2 Particular Contributions 11
1.8.3 Co-author Agreement 14
1.8.4 Additional Publications 15

2 Macro Hydrodynamic Design Aspects 16

Abstract 17
2.1 Introduction 18
2.2 Optimum Hull Form Coefficients 19
2.2.1 Froude Number 20
2.2.2 Demihull Slenderness Ratio 21
2.2.3 Prismatic Coefficient 22
2.2.4 Block Coefficient 23
2.2.5 Demihull Separation 24
2.2.6 Relative Breadth 26
2.2.7 Transom Immersion 27
2.2.8 Summary of Parameter Study 27
2.3 Overall Slenderness 28
2.3.1 Model Test Series 29
2.3.2 Evaluation Procedure 31
2.3.3 Results of Model Test Extrapolation 32
2.3.4 Validity of Model Test Results 32
2.4 Design Case 34
2.5 Conclusions 36
2.5.1 Recommendation for Future Work 37

3 Computational Full-Scale Resistance Prediction 38

Abstract 39
3.1 Introduction 40
3.1.1 Scope of Study 42
3.2 Full-scale CFD Approach 43
3.2.1 Numerical Simulation Tool 45
3.2.2 Computational Mesh Generation Strategy 45
3.2.3 Verification and Validation 46
3.3 Verification of CFD Simulations 46
3.3.1 Mesh Sensitivity Study 47
3.3.2 Presentation of Results 48
3.3.3 Model-Scale Results of 98 m Catamaran 48
3.3.4 Model-Scale Results of 130 m Catamaran 49
3.4 Verification of Near-Wall Flow 49
3.4.1 Shear Force on Rough Flat Plate 55
3.5 Validation of Full-scale Drag 56
3.5.1 Drag Force from Full-scale Sea Trials 58
3.5.2 Extrapolation of Model Test Data 58
3.5.3 Full-scale CFD Results 60
3.5.4 Comparison of Full-scale Drag for 98 m Catamaran 60
3.5.5 Comparison of Full-scale Drag for 130 m Catamaran 61
3.6 Discussion 63
3.6.1 Full-Scale Drag From Sea Trials 63
3.6.2 Correlation Allowance 65
3.6.3 Verification of CFD Simulations 66
3.7 Conclusions 66
3.7.1 Recommendation for Future Work 68

4 Resistance Prediction in Finite Water **69**

Abstract 70

4.1 Introduction 71

4.1.1 Scope of Study 72

4.2 Numerical Prediction Methodology 72

4.2.1 Numerical Simulation Tool 72

4.2.2 Verification of numerical model 72

4.3 Finite Water Effects 74

4.3.1 Steady Finite Water Effects 74

4.3.2 Unsteady Finite Water Effects 76

4.4 Implications on Full-Scale Resistance 81

4.4.1 Full-Scale CFD Approach 81

4.4.2 Case Study of a 98 m Catamaran 82

4.4.3 Case Study of the 130 m Catamaran 85

4.4.4 Practical Implications 86

4.5 Conclusions 88

4.5.1 Recommendations for Future Work 89

4.6 Where to next? 90

5 Transom Stern Ventilation **91**

Abstract 92

5.1 Introduction 93

5.1.1 Transom Stern Flow Predictions 93

5.2 Methodology 96

5.2.1 Numerical Set-up 97

5.2.2 Experimental Set-up 98

5.2.3 Empirical Prediction Method 99

5.3 Validation of Transom Flow 100
5.3.1 Physical Model Tests 100
5.3.2 Nummerical Prediction at Model Scale 100
5.3.3 Emperical Prediction 102
5.3.4 Qualitative Validation of Transom Flow 102
5.3.5 Steady Observations 103
5.4 Characteristics of Flow Past Transom 106
5.4.1 Flow in Stagnant Area 106
5.4.2 Process of Transom Ventilation 107
5.4.3 Results at Full-Scale 108
5.4.4 Impact of Transom Ventilation on Drag Force 110
5.5 Conclusions 111
5.5.1 Recommendations for Future Work 112
5.6 Where to next? 112

6 Full-Scale CFD for Design Space Exploration 114

Abstract 115
6.1 Introduction 116
6.2 Methodology 116
6.2.1 Design Rules 116
6.2.2 Simulation Technique 119
6.3 Results 121
6.3.1 Validation 121
6.3.2 Hydrodynamic Properties of Slender Hulls 121
6.3.3 Design Space Extrapolation 127
6.4 Discussion 138
6.4.1 Methodlogy 138

6.4.2 Influence of Draft on Drag 138
6.4.3 Influence on Shear Force 139
6.4.4 Demihull Interaction 139
6.4.5 Non-Dimensional Drag Force 139
6.4.6 Transport Efficiency 140
6.4.7 Recommendations for Future Work 140
6.5 Conclusions 140
6.5.1 Recommendations for Future Work 141

7 Conclusions **143**
7.1 Achievements 143
7.2 Recommendations for Future Studies 147

8 APPENDIX **148**

APPENDIX **148**

List of Tables

2.1 Fixed parameters of the demihulls of the model series under consideration. . . 29

2.2 Fixed demihull parameters of the model series under consideration. 30

2.3 Parameters of considered catamaran designs derived from the Dubrovsky series. 30

2.4 Parameters of considered catamaran designs derived from the Dubrovsky series. 36

3.1 Relative deviation of predicted drag for 98 m catamaran using CFD and extrapolated model test data corrected for shallow water by the approach of Schuster (1956) with and without form factor with respect to drag derived from full-scale powering measurements. k_S of 100 μm and 200 μm was considered. 61

3.2 Relative deviation of resistance components of 98 m catamaran determined by CFD and extrapolated model test experiment for a smooth hull. Positive values indicate that CFD prediction exceeds extrapolated quantity. 62

3.3 Relative deviation of resistance components of 130 m catamaran determined by CFD and extrapolated model test experiment. Positive values indicate that CFD prediction exceeds extrapolated quantity. 63

3.4 Relative deviation of resistance components determined by CFD and extrapolated model test experiment. Positive values indicate that CFD prediction exceeds extrapolated quantity. 64

4.1 Relative difference between numerical simulations and towing tank results of the 1:50 130 m catamaran. Negative values indicate that the CFD result is below the experimentally determined value. 74

4.2 Comparison of drag force at different length and depth Froude numbers of the 130 m catamaran at 1:50 model scale. * Indicates relative difference to $b/L = 3.8$ instead of $b/L = \infty$. 77

4.3 Relative deviation of predicted full-scale drag for 98 m catamaran using CFD and extrapolated model test data corrected for shallow water by approach of Schuster (1956) without form factor with respect to drag estimated from full-scale powering measurements. 84

4.4 Relative differences of extrapolated model scale results compared to CFD predictions for full-scale resistance of 130 m medium-speed catamaran in shallow water at $h/L = 0.24$. Positive values indicate higher prediction by CFD, model test data has been recorded in shallow $h/L = 0.24$ and deep water $h/L = 0.60$ including the latter corrected by the approach of Schuster (1956). 87

4.5 Relative differences of extrapolated model scale results compared to CFD predictions for full-scale resistance of 130 m medium-speed catamaran in shallow water at $h/L = 0.24$. Positive values indicate higher prediction by CFD, model test data has been recorded in shallow $h/L = 0.24$ and deep water $h/L = 0.60$ including the latter corrected by approach of Schuster (1956). 87

6.1 Main parameters of different catamaran designs with constant overall beam of $B_{OA} = 32$ m. Weight is relative to 130 m base line model. 118

6.2 Parameters of catamaran demihulls that solely depend on loading conditions. Demihull breadth remains constant $B_{dh} = 6.4$ m. 118

6.3 Minimum achieved non-dimensional drag and corresponding slenderness ratio. Slenderness ranges where normalised drag was within 5% of minimum value. 130

6.4 Appropriate speed range for different hull lengths and loading conditions within 10% and 5% of the highest achieved transport efficiency. 130

List of Figures

1.1 Humps and hollows in a typical resistance curve of a catamaran for different demihull separation ratios (s/L) with respect to Froude number (Millward, 1992). Speed regimes are stated and the medium-speed range is shaded in grey. 4

1.2 Arrangement of a large medium-speed catamaran proposed by Davidson et al. (2011b). 5

2.1 Transport efficiency over deadweight tonnes of recent high-speed catamarans, built in Australia (Austal, 2011; Incat, 2011) and a lately proposed medium-speed design of 130 m in length from Davidson et al. (2011b). 19

2.2 Selected ferries in operation displayed by length and velocity with data from Trillo (1991), Austal (2011), and Incat (2011) and a proposed 130 m design by Davidson et al. (2011b). Also the prospective design space for a highly efficient medium-speed catamaran is highlighted. 20

2.3 Recommendations for length-displacement ratio by Saunders (1957), Dubrovsky and Lyakhovitsky (2001), Ayre (Schneekluth and Bertram, 1998) and Schneekluth and Bertram (1998) and values of built catamaran demihulls by Insel (1990). 22

2.4 Demihull slenderness ratio of existing high-speed catamarans over length by Armstrong and Clark (2009). 23

2.5 Design recommendations for prismatic coefficient over Froude number by different authors (Rawson and Tupper, 2001; Jensen, 1994; Taylor, 1943; Dubrovsky and Lyakhovitsky, 2001; Saunders, 1957). 24

2.6 Recommendation for block coefficient for varying Froude number by Rawson and Tupper (2001), Jensen (1994) and Dubrovsky and Lyakhovitsky (2001) and values of built catamarans from Insel (1990). 25

2.7 Wave interference factor for different separation ratios at varying Froude numbers, expressed as the relative difference of the wave-making drag of a catamaran when compared to two single demihulls in isolation (Tasaki, 1962). . 27

2.8 Residuary resistance for catamarans with s/L = 0.3 and different transom immersion ratios (Hadler et al., 2009). 28

2.9 Total resistance coefficient for varying Froude numbers of extrapolated models of the Molland series (Molland et al., 1994). 30

2.10 Normalised resistance for the extrapolated models of the Dubrovsky series. . 33

2.11 Normalised resistance for varying velocity of extrapolated models of the Molland series. 33

2.12 Normalised resistance for catamaran configuration and single demihull in isolation at different demihull selnderness ratios at certain speeds. 34

2.13 Profile view and buttock lines of a possible design for a demihull of medium-speed wave piercing catamaran with a length of L = 110 m and a draft of T =6.1 m. 36

3.1 Proposed design of a 130 m medium-speed catamaran. 42

3.2 Image of the 98 m INCAT high-speed catamaran. 43

3.3 Flowchart to obtain full-scale resistance using computational grids verified at model scale. Top row contains simulations at model scale, middle row shows the assumptions made and bottom row contains simulations at full-scale Reynolds numbers. 44

3.4 Mesh layout shown for the coarse mesh and the 130 m catamaran. 46

3.5 Half model of the 98 m catamaran as it was tested in the AMC towing tank. 47

3.6 Resistance and its components was non-dimensionalised by displacement, density, gravity and further divided by Froude number squared. Drag for 98 m high-speed catamaran at 1:22 model scale determined by CFD (shown as vertical bars) and physical towing tank experiments (shown as hollow markers). 49

3.7 Sinkage and trim for 98 m high-speed catamaran at 1:22 model scale determined by CFD (shown as vertical bars) and physical towing tank experiments (shown as hollow markers). 50

3.8 Non-dimensional resistance for 130 m medium-speed catamaran at 1:50 model scale determined by CFD (shown as vertical bars) and physical towing tank experiments (shown as hollow markers). 50

3.9 Sinkage and trim for 130 m medium-speed catamaran at 1:50 model scale determined by CFD (shown as vertical bars) and physical towing tank experiments (shown as hollow markers). 51

3.10 Effect of varying mesh resolution on shear force coefficient for flow over flat plate at $log(Re) = 6.5, 7.5, 9.75$ (from top to bottom). Vertical line indicates first cell height for highest achievable shear stress. 53

3.11 Deviation in shear force coefficient for most appropriate y_1 for varying cell expansion ratios at different Reynolds numbers. 54

3.12 Results for shear force coefficient from present study compared to established correlation lines for model-ship extrapolation over a wide range of Reynolds numbers. 55

3.13 Integral values of shear force coefficient (C_V) for the flow over a flat plate being smooth (SM) and rough: $k_S/L = 1 \times 10^{-6}$ (SR1) and 2×10^{-6} (SR2). Results were obtained by CFD, ITTC (7.5-02-03-01.4) and empirically by estimating local skin friction by Schlichting (Schli.) for fully rough walls. 57

3.14 Relative increase of shear force coefficient ($C_V(SRi)/C_V(SM) - 1$) compared to hydraulically smooth plate (SM) for equivalent sand grain roughness of $k_S/L = 1 \times 10^{-6}$ (SR1) and 2×10^{-6} (SR2). Range of Reynolds number for a 98 m and a 130 m vessel at medium speeds ($Fr = 0.35 - 0.45$) are indicated. 57

3.15 Full-scale drag predictions for the 98 m medium-speed catamaran from model test experiments (EXP) (with and without form factor, * indicates usage of form factor of $(1+k) = 1.18$) and CFD (CFD) at $Fr = 0.20$–0.43 at two levels of surface roughness. SR1: $k_S = 100\mu$m, SR2: $k_S = 200\mu$m. 62

3.16 Full scale drag predictions for the 130 m catamaran from model test experiments (EXP) (with and without form factor, * indicates $(1 + k) = 1.10$) and CFD (CFD) of bare hull with no superstructure of the 130 m medium-speed catamaran at $Fr = 0.37$ and 0.45 at two levels of surface roughness. SR1: $k_S = 100\mu$m, SR2: $k_S = 200\mu$m. 64

4.1 Calm water resistance of a 1:50 scale model of the 130m medium-speed catamaran in shallow water ($h/L = 0.24$) for $Fr = 0.37$, 0.45 for heavy and light displacement subdivided into a frictional (RF, RV) and pressure related components (RR, RP). 73

4.2 Convergence of residuary resistance of a 130 m catamaran at 1:50 model scale with respect to varying tank dimensions for $Fr = 0.37$ and 0.45. The dashed lines show the relative difference of residuary drag at varying tank depth at original tank width ($b/L = 1.4$) compared to an infinitely deep tank. The dotted lines represent the relative difference of residuary drag for different values of tank width in shallow water conditions ($h/L = 0.24$) compared to an infinitely wide tank. 76

4.3 Fluctuation of trim for 1:22 model of slender catamaran normalised by its average value for Fr = 0.31, 0.39 and 0.44 during towing tank run. 79

4.4 Fluctuation of drag force for 1:22 model of slender catamaran normalised by its average value for Fr = 0.31, 0.39 and 0.44 during towing tank run. 79

4.5 Non-dimensional calm water pitch frequency with respect to length Froude number from model test experiments (EXP), numerical simulations (CFD) and full-scale measurements (FUL) for different water depths. The lines present the prediction by Havelock (1949) (solid line) and corrections for shallow water effects as proposed by Day et al. (2009) for $h/L = 0.24$ (long dashed line) $h/L = 0.35$ (normal dashed line) and $h/L = 0.6$ (short dashed line). 80

4.6 Flowchart to obtain full-scale resistance considering shallow water effects using a novel CFD approach in conjunction with model test experiments for verification. 82

4.7 Dimensionless drag at Fr = 0.31 obtained from CFD and model test extrapolation for two depths which were stated as extreme values for the sea trial measurements. Drag in deep water was added for comparison. 84

4.8 Full scale drag predictions for 130 m catamaran from model test experiments and CFD of bare hull with no superstructure of 130 m medium-speed catamaran at Fr = 0.37 and 0.45 in shallow water. Model test results were obtained at shallow water (EXP-shallow) and deep waterwith (EXP-deep-(S)) and without (EXP-deep) correction for shallow water by approach of Schuster (S). 86

5.1 Transom flow regimes as identified by Maki (2005) A: $Fr_T < 1$ resulting in a stagnant recirculating flow area that is separated by a shear layer. B: $1 < Fr_T < Fr_T(dry)$ produces an unsteady von-Karman street with large surface fluctuations. C: $Fr_T > Fr_T(dry)$ leads to a dry transom and a breaking roller building up behind separation point. D: $Fr_T >> Fr_T(dry)$ so that the breaking roller past the separation disappears. 95

5.2 Cell structure at the transom stern utilised in this study. 98

5.3 Experimental set up in the AMC towing tank. A single catamaran demihull is towed in close proximity to the tank wall. Also the positions of the cameras used and the stream tracers are highlighted. 99

5.4 Flow past the transom at different speeds of Froude numbers of $Fr = 0.24$, 0.30 and 0.36, corresponding to transom draft Froude numbers of $Fr_T = 1.56$, 1.97 and 2.38. 101

5.5 State of transom ventilation where 0 means fully wet and unity fully dry with respect to transom Froude number. Results are based on CFD simulation at model and full scale, experimental measurements and empirical predictions using Doctors et al. (2007) with and without taking limited B_T/T_T values into account. 102

5.6 Side view: Comparison of flow past partially ventilated transom at transom draft Froude number $Fr_T = 1.30$ and 1.37 between physical experiment (bottom) and numerical simulation (top). 104

5.7 Profile view: comparison of flow past partially ventilated transom at transom draft Froude number $Fr_T = 1.97$ and 2.01 between physical experiment (bottom) and numerical simulation (top). 104

5.8 Bottom view: comparison of flow past partially ventilated transom at transom draft Froude number $Fr_T = 1.30$ and 1.37 between physical experiment (bottom) and numerical simulation (top). 105

5.9 a) Squashed horseshoe structure of the flow inside the stagnant area behind the transom (A) at $Fr_T = 1.66$; b) Profile view indicates the reversing behaviour (B) of the stagnant flow; c) Plan view shows the two counter rotating vortices at the upper side of the stagnant area; d) Aft view indicates the rising streamlines (D) that will potentially form the characteristic rooster tail in the wake. 107

5.10 Mesh structure and predicted flow past transom and the distribution of volume fraction at the centre plane of the demihull. 108

5.11 Flow structure and free surface behind the transom undergoing the ventilation process at model scale. Red streamlines present recirculating flow and and a reduced streamline diameter indicates wave breaking. 109

5.12 Image of the transom including the built-up of a rooster tail at $Fr_T = 2.19$. The arrow points at a fluid portion that represents breaking flow recirculation. 110

6.1 Profile view (top) with corresponding water lines for light, medium and heavy displacement and plan view (bottom) with symmetry line of hulls under consideration. 118

6.2 Mesh setup cell density expressed by cell level. Dark shade indicates high mesh density. 120

6.3 Absolute of relative deviation between CFD and experiments for light and heavy displacement and median total uncertainty of DTMB 5415 model (Gorski et al., 2011). 122

6.4 Total resistance coefficient for hull forms under consideration for medium displacement with respect to Froude number. 123

6.5 Drag non-dimensionalised by buoyancy force and divided by Froude number squared presented with respect to Froude number. 124

6.6 Drag non-dimensionalised by buoyancy force and divided by Froude number squared presented with respect to Froude number. Shear force coefficient for medium displacement compared to ship-model correlation lines of Grigson and ITTC. 125

6.7 Heave normalised by draft presented with respect to Froude number for medium displacement. 126

6.8 Trim presented with respect to Froude number for medium displacement. . . 126

6.9 Free surface elevation of 130 m catamaran at medium displacement for Fr =0.25, 0.29, 0.33, 0.37, 0.41, 0.45, and 0.49 from top to bottom. Blue represents wave trough and red wave crest. 131

6.10 Wave elevation of large medium–speed catamarans at $Fr = 0.41$ of 110 – 190 m in length at medium displacement (top to bottom). Blue represents wave trough and red wave crest. 132

6.11 Free surface elevation of 130 m medium- speed catamaran at $Fr = 0.41$ for light (top), medium (middle) and heavy displacement (bottom). Blue represents wave trough and red wave crest. 133

6.12 Non-dimensional drag as a function of demihull slenderness ratio for a) $Fr = 0.29$ (top), b) $Fr = 0.37$ (middle) and c) $Fr = 0.45$ (bottom). 134

6.13 Transport efficiency for a) $Fr = 0.29$ (top), b) $Fr = 0.37$ (middle) and c) $Fr = 0.45$ (bottom). 135

6.14 Speed ranges of each vessel configuration within 10% (top) and within 5% (bottom) of highest achieved transport efficiency. 136

6.15 Comparison of transport efficiency at 28 knots of large medium-speed catamarans (LMSC) at light and medium displacement carrying less than 1,500 tonnes and a 112 m high-speed catamaran at the same speed carrying 1,500 tonnes. 137

8.1 Set-up for volume fraction. 150

8.2 Set-up for kinetic turbulent energy. 151

8.3 Set-up for eddy viscosity. 152

8.4 Set-up for point displacement. 153

8.5 Set-up for dynamic pressure. 154

8.6 Set-up for dissipation rate. 155

8.7 Velocity set-up. A time varying boundary condition at the vessel resembles a steady acceleration until the desired speed was achieved as defined in the *URamp* file. 156

8.8 Set-up for mesh motion restraints and constraints. 158

8.9 Set-up for gravitational acceleration. 159

8.10 Set-up for turbulence properties using a Reynolds-Averaged Stress model. . . 160

8.11 Set-up for fluid properties. 161

8.12 Set-up for turbulence properties. 162

8.13 Set-up for control parameters. 164

8.14 Specification of solvers. 165

8.15 Set-up for solver parameters 1/2. 166

8.16 Set-up for solver parameters 2/2. 167

Nomenclature

Abbreviations

Symbol	Description
AMC	Australian Maritime College
CFD	computational fluid dynamics
EEDI	Energy Efficiency Design Index
ITTC	International Towing Tank Conference
$k-\omega-SST$	name of turbulence model
NPL	National Physical Laboratory
OpenFOAM	name of open source CFD tool box: Open Field Operation And Manipulation
RANS	Reynolds-Averaged Navier-Stokes
SST	shear stress transport

Greek Symbols

Symbol	Description	Definition	Units
α	exponent	$log(Re)+0.56725$	
η_{dry}	transom ventilation	A_{TW}/A_T	–
$\eta_{propulsion}$	overall efficiency of propulsion plant	-	–
$\eta_{transport}$	transport efficiency	$\frac{dwt\times g\times V}{P_{installed}}$	–

λ	ship model scale ratio	-	–
ν	kinematic viscosity	-	m^2/s
ω	dissipation rate	-	m^2/s
ρ	density	-	kg/m^3
τ_W	wall shear stress	-	$kg/m/s^2$

Roman Symbols

Symbol	Description	Definition	Units
A_{Deck}	deck area	-	m^2
A_{proj}	projected frontal area of ship superstructure	-	m^2
A_T	transom area	-	m^2
A_{TW}	wetted transom area	-	m^2
A_X	cross sectional area amidships	-	m^2
B	demihull beam	-	m
b	water width	-	m
B_{OA}	overall vessel beam	-	m
B_T	transom beam	-	m
c	horizontal demihull clearance	-	m
C_{AA}	correlation allowance coefficient coefficient	-	–
C_B	block coefficient	$\frac{\nabla}{L \times B \times T}$	–
C_F	friction coefficient or model-ship correlation coefficient	$\frac{R_F}{1/2 \times \rho \times V^2 \times S_W}$	–
C_f	local skin friction coefficient	$\frac{\tau_W}{1/2 \times \rho \times V^2}$	–
C_P	prismatic coefficient	$\frac{\nabla}{L \times B \times T}$	–
C_{Pr}	pressure resistance coefficient	$\frac{R_P}{1/2 \times \rho \times V^2 \times S_W}$	–
C_R	residuary resistance coefficient	$\frac{R_R}{1/2 \times \rho \times V^2 \times S_W}$	–

C_T	total resistance coefficient	$\frac{R_T}{1/2 \times \rho \times V^2 \times S_W}$	–
C_V	shear force coefficient coefficient	$\frac{\int \tau_W dS_W}{1/2 \times \rho \times V^2 \times S_W}$	–
C_{WP}	wave pattern resistance	-	–
D	distance travelled in ship operation	-	nm
dC_F	friction force coefficient due to surface roughness	$\frac{R_R}{1/2 \times \rho \times V^2 \times S_W}$	–
$du,\ dv$	increase in flow velocity relative to vessel due to restricted water depth and width	-	m/s
dwt	deadweight tonnes	-	t
$(1+k)$	form factor	-	–
f	frequency of ship response	-	1/s
f_G	Grigson factor		-
Fr	Froude number	$\frac{V}{\sqrt{g \times L}}$	–
Fr_h	depth Froude number	$\frac{V}{\sqrt{g \times h}}$	–
Fr_T	transom draft Froude number	$\frac{V}{\sqrt{g \times T_T}}$	–
g	gravitational constant	9.81	m/s^2
h	water depth	-	m
k	kinetic turbulent energy	-	m^2/s^2
k_S	sand grain roughness height	-	μm
L	ship length	-	m
l	towing tank length	-	m
$L/\nabla^{1/3}$	hull slenderness ratio	$L/\nabla^{1/3}$	–
m	ship-tank cross section area ratio	$A_X/(b \times h)$	–
m_{fuel}	fuel consumption	-	t
$P_{required}$	required engine power	-	kW

R	resistance force	-	$\mathrm{kg} \times \mathrm{m/s^{-2}}$
R_A	wind resistance force	-	$\mathrm{kg} \times \mathrm{m/s^{-2}}$
$R_A A$	correlation allowance force	-	$\mathrm{kg} \times \mathrm{m/s^{-2}}$
R_{DCF}	additional drag force due to surface roughness	-	$\mathrm{kg} \times \mathrm{m/s^{-2}}$
Re	Reynolds number	$V \times L/\nu$	–
Re_T	transom draft Reynolds number	$\sqrt{g \times T_T^3}/\nu$	–
R_R	friction or model-ship correlation force	-	$\mathrm{kg} \times \mathrm{m/s^{-2}}$
R_R	residuary resistance force	-	$\mathrm{kg} \times \mathrm{m/s^{-2}}$
R_T	total resistance froce	-	$\mathrm{kg} \times \mathrm{m/s^{-2}}$
r_y	cell expansion ratio	y_{i+1}/y_i	-
s	horizontal demihull separation at centre lines	-	m
sfc	specific fuel consumption	-	g/kW/h
S_W	wetted surface area	-	$\mathrm{m^2}$
T	maximum vessel draft	-	m
T_T	transom draft	-	m
U	flow velocity	-	m/s
V	ship speed	-	$\mathrm{m/s}, \mathrm{kn}$
∇	volumetric displacement	-	$\mathrm{m^3}$
x, z	longitudinal and vertical ship hull coordinates	-	m
y_1	first cell height	-	m
y^+	dimensionless first cell heigth	-	–
$_{EXP}$	subscript indicating value obtained from physical experiments	-	–
$_{CFD}$	subscript indicating value obtained from CFD simulation	-	–

dh	subscript indicating value for a single demihull	-	–
FW	subscript indicating value for fresh water	-	–
SW	subscript indicating value salt water	-	–
$LIGHT$	subscript indicating value light displacement case	-	–
$MEDIUM$	subscript indicating value medium displacement case	-	–
$HEAVY$	subscript indicating value heavy displacement case	-	–
s	subscript indicating value for the full-scale ship	-	–
m	subscript indicating value for the model-scale ship	-	–
$sea\ trial$	subscript indicating value obtained from full-scale sea trials	-	–

Chapter 1

Introduction

Large medium-speed catamarans are a new class of ships for more fuel efficient RoPax transportation, evolving from current high-speed catamarans. This thesis focuses on the drag prediction and derivation of appropriate hull form properties for these novel craft with minimum resistance to promote economical and ecologically sustainable fast sea transportation.

1.1 Current Large Catamarans

Contemporary RoPax catamarans are characterised by two demihulls with a large superstructure to accommodate the payload. They are propelled by waterjets, have a length of up to 125 m and operate at speeds of 40 knots (Lingwood, 1996) and above, usually at Froude numbers of $Fr = 0.6 - 1.0$ (Yun and Bliault, 2010). Compared to monohulls, catamarans can use 30% less power to transport the same deadweight at high speeds (Martinez de Oses and La Castalls, 2005). Further significant advantages comprise high transverse stability and large deck areas in conjunction with slender demihulls that enable low wave-making resistance and cause low added resistance when encountering waves (Yun and Bliault, 2010). When combined with good manoeuvrability they allow for effective fast sea transportation. However, the high speed of these craft leads to high fuel consumption and substantial emissions (Psaraftis et al., 2009; Banawan et al., 2013). Expected high future fuel costs, society's increasing awareness of environmental sustainability, and official regulations of the *International Maritime Organisation* to limit emissions such as MARPOL 73/78 Annex VI (Resolution MEPC.176(58)) raise the demand for more fuel-efficient vessels without compromising the advantages of current high-speed catamarans. For example, it has been demonstrated that for a 72 m catamaran a 30% reduction in fuel consumption, and hence savings in fuel costs and emissions, per year can be achieved when a 30% reduction in speed is applied (Ba-

nawan et al., 2013). These savings may be less than expected when applying the power-speed law, however, this is based on measured data which also includes speed independent energy consumption. Furthermore, the speed reduction shifts the vessel from the high-speed regime into the medium-speed regime, where a higher drag coefficient can be expected (see Figure 1.1) and where the high-speed hull form may not be optimal.

1.2 Fuel Consumption and Transport Efficiency

The amount of required fuel (m_{fuel}) per distance (D) can be estimated by the specific fuel consumption (sfc), the required power ($P_{required}$), and the speed (V):

$$m_{fuel}/D = sfc \times P_{required} \ / \ V \tag{1.1}$$

The effectiveness of a ship hull for transportation can be defined as the transport efficiency which is the ratio of deadweight ($dwt \times g$) times speed (V) over required power:

$$\eta_{transport} = dwt \times g \times V \ / \ P_{required} \tag{1.2}$$

With these equations, the fuel consumption (m_{fuel}) per deadweight carried ($dwt \times g$) per distance travelled (D) can be expressed as:

$$m_{fuel}/(dwt \times g \times D) = sfc \ / \ \eta_{transport} \tag{1.3}$$

If it is assumed that the required power is the effective power over the overall efficiency of the propulsion plant ($\eta_{propulsion}$), and that effective power is defined as drag times velocity ($P_E = R_T \times V$), the transport efficiency for a certain speed can be defined as:

$$\eta_{transport} = \eta_{propulsion} \times dwt \times g \ / \ R_T \tag{1.4}$$

From a hull form design point of view, the drag force per deadweight carried must be minimised to effectively maximise transport efficiency and thus, to minimise the fuel consumption and emissions as these quantities are inversely proportional to transport efficiency. If the transport efficiency, when compared to current craft, can be significantly increased, large medium-speed catamarans have the potential to lead large catamaran technology into a promising future to promote economic viable fast sea transportation with reduced environmental impact. The key to high transport efficiency is the hydrodynamic design of such vessels to provide the lowest drag in their specific speed regime. Therefore the presented presentation of the results was preferred over the Energy Efficiency Design Index (EEDI) from the *International Maritime Organisation*.

1.3 Speed Regimes

The appropriate hydrodynamic design of a ship strongly depends on the speed regime in which it is designed to operate. These regimes are best characterised by the Froude number, which is the dimensionless velocity with respect to ship length. It is defined as:

$$Fr = \frac{V}{\sqrt{g \times L}} \tag{1.5}$$

where L is the boat's length and g the gravitational constant. Depending on the Froude number, the speed range can be subdivided into low, medium or high. In each regime, characteristic hydrodynamic properties and design requirements apply; an optimum hull form for one speed regime may not be appropriate for the others.

1.3.1 Low-speed Regime

Low speed can be understood as the speed range where the friction resistance dominates over the wave-making resistance of a ship. The lines of the ship have to be streamlined to avoid flow separation (Schneekluth and Bertram, 1998) and to reduce viscous pressure resistance (Bertram, 2000). The wetted surface area has to be minimised to reduce the friction force on the hull. Sinkage and trim remain negligibly small (Molland et al., 1994).

1.3.2 Medium-speed Regime

In the medium-speed range, a large portion of the drag of the hull will comprise of wave-making resistance and sinkage and trim can change considerably with changing speed (Molland et al., 1994). The latter can amplify if the hull features convex buttock lines (Lewis, 1988). The magnitude of wave-making resistance will strongly depend on the Froude number as the interference of the bow and stern waves lead to marked humps and hollows in the resistance curve (see Figure 1.1) where a major hump occurs at a Froude number of $Fr \approx 0.5$ (Lewis, 1988). Generally, an increased slenderness of the boat will be beneficial for its resistance properties at medium speeds (Tupper, 2004), but general guidelines state that Froude numbers in the range of $0.25 < Fr < 0.27$ and $0.37 < Fr < 0.50$ should be avoided in boat design (Jensen, 1994) as these speeds feature unfavourable humps in the resistance curve.

1.3.3 High-speed Regime

The speed past the drag hump ($Fr > 0.6$) can be considered as high-speed where the hull enters the planing regime. Lift is provided by hydrodynamic forces as well as by the volume

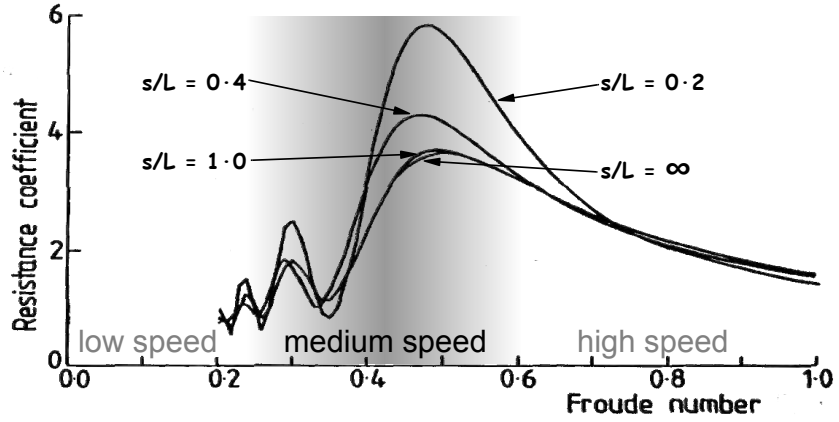

Figure 1.1: Humps and hollows in a typical resistance curve of a catamaran for different demihull separation ratios (s/L) with respect to Froude number (Millward, 1992). Speed regimes are stated and the medium-speed range is shaded in grey.

displacement of the hull and friction becomes the main contributor towards the total resistance (Bertram, 2000). Compared to displacement hulls the buttock lines should be straight and cut off at the transom stern to provide beneficial lift and drag properties (Lewis, 1988) and a reduction in wetted surface area supports reducing the viscous resistance (Faltinsen, 2005) and therefore the total resistance. Characteristically, the coefficient of wave-making resistance reduces with increasing speed and the centre of gravity rises while the change in trim angle is small when compared to the medium-speed regime (Molland et al., 1994).

1.4 Current State of Knowledge

1.4.1 Catamaran Design for Medium Speeds

Davidson et al. (2011b) proposed a design for a 130 m medium-speed catamaran (Figure 1.2) and stated that an increase in size and reduction in speed is beneficial for a high transport efficiency, which was shown to exist in comparison with monohull designs with similar deadweight, deck area and speed. Furthermore, the increased length and reduced speed is favourable for ship motions and therefore passenger comfort (Itabashi and Michida, 2001) and also structural design requirements when compared to current high-speed catamarans. The novelty of this type of vessel is that they operate at critical speeds where the overall resistance consists of a significant amount of wave-making, and residuary resistance is at a maximum. Usually this speed range, called hump speed, is avoided by boat designers and due to the lack of experience design requirements are not well understood and accurate hull

Figure 1.2: Arrangement of a large medium-speed catamaran proposed by Davidson et al. (2011b).

form design guidelines are missing. However, the study of Davidson et al. (2011b) has shown that catamarans with slender demihulls providing low wave-making resistance can be an appropriate feature for low residuary drag around the speed hump, as the distinct humps and hollows in the resistance curve become less pronounced when compared to contemporary high-speed catamarans. They concluded that large medium-speed catamarans are competitive when compared to conventional fast monohull vessels, but more details on the hull form design are required.

1.4.2 Studies on Catamaran Design Parameters

Matsui (1993) and Molland et al. (1994) highlighted that the slenderness ratio of a demihull $\left(L/\nabla_{dh}^{1/3}\right)$ is the most important hull form parameter that influences the resistance of fast displacement catamarans. In their studies they investigated slenderness ratios ranging from $6.3-9.5$. Dubrovsky and Lyakhovitsky (2001), Saunders (1957) and Ayre (Schneekluth and Bertram, 1998) indicated optimum values for demihull or hull slenderness around hump speed of $L/\nabla^{1/3}=8-9$. In contrast, Davidson et al. (2011b) investigated a medium-speed catamaran demihull with a slenderness ratio of 12 for beneficial performance at hump speed and Miyata et al. (1991) experimentally studied the drag characteristics of demihulls with a slenderness of $L/\nabla_{dh}^{1/3}=10-13$ with benefits for reduced wave-making resistance at hump speed. However, whilst no conclusions towards an optimum slenderness for lowest drag around the major speed hump were drawn, in support of high slenderness ratios McKesson et al. (2000) proposed that catamarans with slender hulls potentially minimise the environmental impact. The influence of hull form variations on the drag force of displacement catamarans has been extensively studied in the past, with experimental investigations into the effect of changing demihull separation and/or slenderness by Matsui (1993), Molland et al. (1994), Dubrovsky and Lyakhovitsky (2001) and Caprio and Pensa (2007). Altering demihull separation and

its effect on the resistance was studied computationally by Eggers (1955), Tasaki (1962), Everest (1968), Millward (1992), Yeung and Wan (2008) and experimentally by Miyazawa (1979), Doctors (1993), and Broglia et al. (2014) and Zaghi et al. (2011) who also included numerical approaches. Murdijanto et al. (2011) and Utama et al. (2012) experimentally studied the influence of demihull separation and longitudinal offset that was also computationally investigated by Eggers (1955) and later by Söding (1997) and Tuck and Lazauskas (1998). The above-mentioned literature provides the guidance that an increase in slenderness, as well as an increase in demihull separation, can reduce the resistance significantly especially around hump speed which can be seen in Figure 1.1. Also a longitudinal offset of the demihulls by a half ship length provides significant reductions in drag in this speed range compared to a symmetric demihull configuration. These publications and a comprehensive survey of built catamarans by Insel and Molland (1991) provide a large base to determine appropriate hull form parameters for fast displacement catamarans. However, these studies mainly include demihulls with a slenderness of $L/\nabla_{dh}^{1/3} < 8$. Davidson et al. (2011b) proposed that high-speed catamaran hulls are not necessarily optimal for operation at medium speeds. Therefore, more research is required to investigate appropriate hull form parameters for catamarans with very slender demihulls that can operate efficiently at medium speeds in the Froude numbers of $Fr = 0.25 - 0.50$.

1.4.3 Resistance Prediction Tools

To study the resistance properties for a large range of hull forms accurate computational tools are desirable over model test experiments to avoid excessive model building and testing costs. Empirical, potential flow and finite volume methods are the most widely used tools for resistance prediction (Bertram, 2000). Empirical approaches being the cheapest to use, they have mainly been developed for resistance prediction purposes of high-speed catamarans, such as those of Sahoo et al. (2008), but their accuracy at medium and low speeds has been unacceptable for design purposes. Potential flow methods are more promising as they resolve the flow, but their application in the medium-speed range, such as by Salas et al. (2004), have shown that the drag predictions around the drag hump are less accurate when compared to experimental data, with reasons being that they are not able of inherently modelling the transom ventilation process, wave breaking and viscous pressure losses (Bertram, 2000). Finite volume approaches, such as computational fluid dynamics (CFD) based on RANS equations (Reynolds-averaged Navier Stokes) have been found to provide a good compromise between computational resource requirements and achieved accuracy. Some researchers have demonstrated the satisfactory prediction of hydrodynamic forces on catamarans at medium

speeds (Zaghi et al., 2011; Haase et al., 2011; Haase et al., 2012a; He et al., 2011). However, none of them investigated the capability of CFD of correctly predicting the partial transom ventilation, which occurs at medium speeds for hulls with a deep transom (Doctors et al., 2007), such as typical wave-piercing catamarans. Furthermore, CFD can provide better insight into flow characteristics when compared with standard model test experiments. Other important advantages of CFD over model test experiments are low model building costs, and the ability to study ship hydrodynamics without violating scaling laws (Raven et al., 2008; Haase et al., 2012a; Hochkirch and Mallol, 2013). Not only is the Froude number obeyed, which characterises the effects of wave-making, but also viscous effects, as characterised by the Reynolds number, such as friction on the wetted hull or flow separation (Bertram, 2000). The Reynolds number is defined as:

$$Re = \frac{V \times L}{\nu} \tag{1.6}$$

where V is the boat's velocity, L the boat's length and ν the kinematic viscosity. Nonetheless, one drawback of full-scale modelling is a lack of confidence in results, as it is difficult to validate them. Thus, a method needs to be developed that increases the confidence by including a verification procedure into the prediction methodology.

In addition, if a surface vessel operates, or is model-tested, in shallow water its drag, especially its wave-making drag, will increase (Tamura, 1972). Since medium-speed catamarans are likely to operate at the speed range that leads to the highest wave-making, shallow water may have a significant effect on their drag force. Powering requirements to maintain the speed achieved in deep water may double (Griggs and Woo, 2005; Davidson et al., 2011a). Hence, any resistance prediction tool needs to be able to correctly incorporate the effect of restricted water on the overall drag force.

1.5 Research Objectives

It has been proposed that if high-speed catamarans evolve to large medium-speed catamarans they can become highly fuel-efficient vessels and provide economically attractive and environmentally sustainable fast sea transportation (Davidson et al., 2011b). However, since the hydrodynamic regime at medium-speed is considerably different from the high-speed one, appropriate hull form characteristics need to be established because the currently available data is insufficient to efficiently design such vessels. To investigate the effects of different hull form characteristics on the vessel performance, accurate and resource efficient resistance prediction tools are required to evaluate the impact of even small changes in hull geometry. Therefore,

this study will investigate how current knowledge can be applied for the hydrodynamic design of large medium-speed catamarans to obtain initial values for hull from properties to provide minimum resistance. This research will also focus on the application of computational fluid dynamics for calm water performance prediction of full-scale catamarans in deep and shallow water and how these simulations can be verified and validated. Once a numerical model is established a hull form series will be developed and tested for the effect of variations in slenderness ratios, demihull separation, displacement and speed on the performance of the vessel. These results will then allow the derivation of conclusions for design guidelines for large medium-speed catamarans with high transport efficiency.

This thesis aims to answer the following research questions:

- To what extent can the current state of knowledge contribute to designing hull forms for medium-speed catamarans with minimum resistance?
- How can computational fluid dynamics be verified and validated to accurately predict the resistance force of a full-scale large medium-speed catamaran?
- How can finite water depth and width in operation and model testing of large medium-speed catamarans be quantified and taken into account when predicting full scale performance?
- How can the stagnant flow past a partially ventilated transom stern be investigated and characterised?
- What are desirable values for hull form parameters such as demihull slenderness, demihull separation ratio and transom immersion for providing low resistance and high transport efficiency for large medium-speed catamarans?

Each question has been addressed in a separate chapter of this thesis.

1.6 Thesis Layout

This thesis follows a thesis by publication strategy, which implies that each chapter stands as an independent research paper that has been published, has been accepted for publication, or is currently in the revision process.

Chapter 1 General information on the current state of the art of large medium-speed catamarans and the scope of this research is outlined.

Chapter 2 Focussing on the issue of determining hull form parameters which provide low drag, the literature has been reviewed and appropriate hull form coefficients have been derived. Also, a design case has been set up to establish if either a wide and short or a long and slender catamaran layout is suitable for carrying a certain payload on a required size of deck area. This was achieved by extrapolating existing experimental data from a hull form series with constant deadweight and constant deck area, but varied slenderness and demihull separation ratios, to full-scale to evaluate the transport efficiency of different configurations. Finally, by using the presented methodology, a hull form for a large medium-speed catamaran at a certain speed has been derived which maximises transport efficiency.

Chapter 3 An approach to utilise CFD simulations in conjunction with model test experiments is introduced to predict the full-scale drag of a large catamaran. It is verified with model test experiments and the resulting full-scale drag is validated with extrapolated model test data and results from sea trial measurements of large catamarans at medium-speeds. The key advantage of this novel method is that for verification at model scale and prediction at full scale identical computational meshes can be used.

Chapter 4 The developed CFD approach is now applied for the full-scale performance prediction for vessels operating in shallow water. Steady and unsteady shallow water effects are discussed including depth and width requirements for scale models in deep and shallow water to minimise unfavourable finite water effects. Furthermore by comparing CFD results to extrapolated model test data, conclusions for powering and full-scale drag prediction are drawn.

Chapter 5 The flow around the transom stern of a medium-speed vessel is investigated using CFD at model and full-scale, and experimental techniques. Observations of experiments and simulations are compared and distinctive flow features are characterised for the partially ventilated state. The process of quasi-steady transom ventilation is shown.

Chapter 6 The drag of a series of full-scale catamarans of lengths from 110 m to 190 m, but with similar payload capacities, is studied using the developed CFD approach. Each length corresponds to a certain slenderness ratio of the demihull, where the demihull and

overall beam of the vessel remains constant. The full-scale prediction approach is utilised to investigate the vessel performance at Froude numbers ranging from $0.25 < Fr < 0.49$ to derive the most appropriate slenderness ratios for lowest drag and highest transport efficiency for large medium-speed catamarans operating around the drag hump speed.

Chapter 7 The main findings of the above chapters are summarised, and the limitations and implications of the work are stated. An outlook for future research directions is also given.

1.7 Contribution to Contemporary Ship Hydrodynamics

The key contribution of this work is the development of a new approach to utilise CFD simulations, in conjunction with model-scale experiments, to accurately predict full-scale vessel drag. This technique can be used for model-ship extrapolation without needing empirical input such as model-ship correlation lines, a form factor or corrections for finite waters, or surface roughness allowance. Alternatively, it can be utilised as an approach for hull form studies at full-scale Reynolds numbers, once a base model has been verified by model test experiments. The method has been successfully validated using sea trial data from existing large catamarans.

Investigations on the calm water resistance in restricted waters have shown that finite water effects, including steady ones like increasing drag and unsteady ones such as an increase in the period of disturbing oscillations in drag and running attitude, can be replicated in CFD when compared to model test experiments and full-scale ship data. While the unsteady effects are especially an issue during transient drag prediction, as less than a full cycle of the oscillation may be recorded, the steady effects may lead to a doubling in power requirements if the vessel operates in shallow water. Hence, the numerical tool can be used to predict the drag of the ship in shallow water and also to appropriately size a physical test model to avoid undesirable finite water effects.

Furthermore, this research has derived appropriate design parameters such as demihull slenderness, demihull separation and transom immersion ratio for large medium-speed catamarans, based initially on a literature survey and subsequently through a comprehensive numerical study of a medium-speed hull form family. The latter provides information on a design space that has not been covered by earlier studies and hence provides novel insights into the design of medium-speed catamarans with low drag. The results will allow boat designers to choose appropriate hull form parameters for hulls with minimum resistance, or

highest transport efficiency, for economic benefits and ecologically sustainable vessels with the length of 110 m to 190 m that operate at Froude numbers of $Fr = 0.25 - 0.49$.

The investigation of the flow past a partially ventilated transom showed that numerical simulations can replicate the flow characteristics in the stagnant area and the quasi-steady process of ventilation. It also demonstrated that full ventilation occurs at lower speeds at full-scale Reynolds numbers. It has been shown that differences in transom ventilation at constant speed induce significant differences in drag that vanish in fully wet or dry stages.

The outcomes of this thesis is of particular interest to naval architects involved in designing large catamarans for fast sea transportation, to ship hydrodynamicists who evaluate the performance of full-scale ships based on model test results, to maritime engineers using CFD simulations for performance predictions of full-scale appliances, to towing tank operators who determine appropriate model sizes based on speed and towing tank dimensions.

1.8 Statement of Contribution

1.8.1 Candidate's Responsibility

Chapters 2 - 6 have been published or are in the process of publication as papers in engineering journals as stated in the beginning of each chapter. As the leading author the candidate claims to have taken overall responsibility for:

- Conceptual design of the study in each paper
- Survey of relevant literature
- Design of numerical or experimental test matrices
- Conduct of numerical analyses
- Conduct of towing tank experiments for Chapter 5
- Interpretation of results
- Preparation of manuscript

1.8.2 Particular Contributions

However, guidance and support was given by supervisors and other collaborators, hence they are named as co-authors. In particular they contributed as follows:

Chapter 2

Original manuscript citation:

M. Haase, G. Davidson, S. Friezer, J. Binns, G. Thomas, and N. Bose (2012c). "On the Macro Hydrodynamic Design of Highly Efficient Medium-speed Catamarans with Minimum Resistance". In: *Transaction of the Royal Institution of Naval Architects, Part A - International Journal of Maritime Engineering* 154.A3, pp. 131–142

Gary Davidson defined the vessel specifications for which the case study was conducted. Together with Stuart Friezer he provided top-level consultancy. Jonathan Binns, Giles Thomas and Neil Bose assisted with high-level advice and manuscript preparation.

Work load: Candidate: 85%; Gary Davidson, Stuart Friezer, Jonathan Binns, Giles Thomas, Neil Bose: 15%

Chapter 3

Original manuscript citation:

M. Haase, K. Zürcher, G. Davidson, J. Binns, G. Thomas, and N. Bose (2015e). "Novel CFD-Based Full-Scale Resistance Prediction for Large Medium-Speed Catamarans". In: *Ocean Engineering* under review

Konrad Zürcher provided the model test data of the 98 m catamaran and assisted with analysing sea trial data to obtain values for the thrust force based on shaft power measurements. Giles Thomas supported the manuscript preparation and top-level advice. Also top-level consultancy was provided by Gary Davidson, Jonathan Binns and Neil Bose.

Work load: Candidate: 85%; Konrad Zurcher: 5%; Giles Thomas: 5%; Gary Davidson, Jonathan Binns and Neil Bose: 5%

Chapter 4

Original manuscript citation:

M. Haase, G. Davidson, J. Binns, G. Thomas, and N. Bose (2015a). "Full-Scale Resistance Prediction in Finite Waters A Study Using CFD Simulation, Model Test Experiments and Sea Trial Measurements". In: *Proceedings of the Institution of Mechanical Engineers, Part M: Journal of Engineering for the Maritime Environment* under review

Giles Thomas supported the manuscript preparation and top-level advice. Also top-level consultancy was provided by Gary Davidson, Jonathan Binns and Neil Bose.

Work load: Candidate: 90%; Giles Thomas: 5%; Gary Davidson, Jonathan Binns and Neil Bose: 5%

Chapter 5

Original manuscript citation:

M. Haase, J. Binns, G. Thomas, and N. Bose (2015f). "Wave-piercing Catamaran Transom Stern Ventilation Process". In: *Ship Technology Research / Schiffstechnik* in press

Giles Thomas, Jonathan Binns and Neil Bose supported the manuscript preparation and provided top-level advice.

Work load: Candidate: 90%; Giles Thomas, Jonathan Binns and Neil Bose: 10%

Chapter 6

Original manuscript citation:

M. Haase, G. Davidson, S. Friezer, J. Binns, G. Thomas, and N. Bose (2015c). "Hydrodynamic Hull Form Design Space Exploration of Large Medium-Speed Catamarans Using Full-Scale CFD". in: *Transaction of the Royal Institution of Naval Architects, Part A - International Journal of Maritime Engineering* 157.A3, pp. 161–174

Gary Davidson and Stuart Friezer established the medium-speed hull form family which was investigated. Giles Thomas, Jonathan Binns and Neil Bose assisted with top-level advice and manuscript preparation.

Work load: Candidate: 85%; Gary Davidson and Stuart Friezer: 10%; Giles Thomas, Jonathan Binns and Neil Bose: 5%

1.8.3 Co-author Agreement

With our signature we agree that the stated work load correctly reflects the synthesis of each paper.

_____
Prof Giles Thomas

_____
A/Prof Jonathan Binns

_____
Prof Neil Bose

_____
Gary Davidson

_____
Stuart Friezer

_____
Konrad Zürcher

1.8.4 Additional Publications

During the course of this research, the findings have been published or accepted in high-quality engineering journals or at international conferences. The following titles have also arisen from this study but did not form a part of this thesis. These articles comprise:

M. Haase, G. Davidson, G. Thomas, J. Binns, and N. Bose (2012b). "On the Design and Resistance Prediction of Large Medium-Speed Catamarans". In: *Proceeding of International Conference on High-Performance Vehicles*. Duisburg, Germany, pp. 78–89

M. Haase, J. Binns, G. Thomas, and N. Bose (2012d). "Resistance Prediction of Medium-speed Catamarans Using Free-surface Viscous Flow Simulations". In: *15th Numerical Towing Tank Symposium*. Cortona, Italy, pp. 1–6

M. Haase, F. Iliopulos, G. Davidson, S. Friezer, G. Thomas, J. Binns, N. Bose, J. Lavroff, and M. R. Davis (2012a). "Application of RANSE Based Simulations for Resistance Prediction of Medium-speed Catamarans at Different Scales". In: *Proceedings of 18th Australasian Fluid Mechanics Conference*. Launceston, Australia, p. 270

M. Haase, G. Davidson, J. Binns, G. Thomas, and N. Bose (2013). "Practical Design Aproach and Resistance Prediction of Large Medium-speed Catamarans". In: *Ship Technology Research / Schiffstechnik* 60, pp. 4–12

M. Haase, G. Davidson, S. Friezer, J. Binns, G. Thomas, and N. Bose (2015b). "Full-Scale Simulation-based Hull Form Design of Large Medium-speed Catramarans with High Fuel Efficiency". In: *Proceedings of the 13th International Conference on Fast Sea Transportation*. Washington, D.C., US

M. Haase, G. Davidson, S. Friezer, J. Binns, G. Thomas, and N. Bose (2015d). "Maximising Transport Efficiency by Utilising Full-Scale CFD for the Initial Ship Design Process Validation and Application for Large Catamarans". In: *Proceedings of International Maritime Conference PACIFIC*. vol. I. Sydney, Australia

Chapter 2

On the Macro Hydrodynamic Design of Large Medium-speed Catamarans with Minimum Resistance

This chapter has been published and the citation for the research article is:

M. Haase, G. Davidson, S. Friezer, J. Binns, G. Thomas, and N. Bose (2012c). "On the Macro Hydrodynamic Design of Highly Efficient Medium-speed Catamarans with Minimum Resistance". In: *Transaction of the Royal Institution of Naval Architects, Part A - International Journal of Maritime Engineering* 154.A3, pp. 131–142

The current version of this chapter has been modified compared to the published version to guide the reader more conveniently through this thesis.

Chapter 3

Novel CFD-Based Full-Scale Resistance Prediction for Large Medium-Speed Catamarans

This Chapter has been submitted for publication and is under peer review. The current citation for the research article is:

M. Haase, K. Zürcher, G. Davidson, J. Binns, G. Thomas, and N. Bose (2015e). "Novel CFD-Based Full-Scale Resistance Prediction for Large Medium-Speed Catamarans". In: *Ocean Engineering* under review

---

The current version of this chapter has been modified compared to the published version to guide the reader more conveniently through this thesis.

Abstract

A novel CFD-based approach is presented that is used in conjunction with model test experiments to predict ship resistance at full-scale Reynolds and Froude numbers. It relies on verification using model scale experiments, including an agreement of integrated shear force with established model-ship correlation lines at model and full-scale, and includes surface roughness effects. One major advantage of the method is that the geometric dimensions of the CFD modelling remain at model scale. CFD simulation results were successfully verified considering the drag of two different catamarans at 1:22 and 1:50 model scale. Furthermore, it is shown that an identical near-wall mesh can be used for both model and full-scale simulations without compromising the accuracy of the shear force. At full-scale the deviation of resistance between CFD prediction, model test extrapolation and full-scale measurements of a 98 m catamaran was as low as 5% at $Fr = 0.40$ and 0.43. For a novel 130 m catamaran variations in full-scale drag for a smooth hull were also less than 5% when comparing extrapolated model scale experiments and CFD predictions. However, at such large Reynolds numbers CFD predictions for correlation and roughness allowance were significantly higher compared to estimates proposed in ITTC guidelines.

3.1 Introduction

In Chapter 2 it has been shown that for fast catamarans the transport efficiency, can be significantly increased by increasing size and reducing speed, which aligns with the findings of Davidson et al. (2011b). An image of this novel type of ship is presented in Figure 3.1. However, due to the novelty of this vessel type, experience in applying appropriate resistance prediction methods is lacking and therefore in the preliminary design phase of such vessels it is not currently possible for designers to confidently predict their resistance and hence powering requirements. A novel approach based on computational fluid dynamics aided by model test experiments has been developed and is presented here. It has been validated by successfully comparing results with predictions from extrapolated model test data and results from full-scale sea trials.

For a new class of ship there are several reasons why the accuracy of predicted full-scale resistance values, that are based on extrapolated model test data using the procedures established by the International Towing Tank Conference (ITTC), should be questioned. Particularly since no model-ship correlation data will be available to correctly predict full-scale drag based on model test results the extrapolation process is at the moment necessarily based on empirical input (Bertram, 2000).

Firstly, whilst recommended procedures and guidelines for full-scale resistance prediction based on model test extrapolation have been established by the ITTC for both conventional (7.5-02-03-01.4) and high-speed craft (7.5-02-05-01), they do not include explicit details on an approach for medium-speed catamarans. Even though medium-speed catamarans will operate at speeds of 20–35 knots, which are typical for conventional monohull ferries, their slender demihulls in close proximity of each other are rather a feature of high-speed craft. However, their hull forms and operating environment are quite different when compared to contemporary high-speed catamarans. The demihulls of medium-speed vessels have more convex buttock lines and significantly reduced transom immersion to account for operating around hump speed, where wave-making usually dominates the overall resistance. Therefore they cannot be clearly categorised as either high-speed craft nor conventional vessels.

Secondly, in the conventional resistance extrapolation approach of ITTC (7.5-02-03-01.4), which was based on the original proposal of (Froude, 1874), the total drag force is decomposed into the frictional component $C_F \times (1+k)$ and a residuary component C_R. C_F solely depends on Reynolds number, $(1+k)$ is a function of hull form geometry and C_R depends on Froude number and hull form geometry. The first two are assumed to be independent of the Froude number, while the latter two are assumed to be independent of hull size and Reynolds number.

However, in this study it was found that at medium speeds the Froude number also has an influence on the vessel's shear force, which is presented in Section 6.3.2. This can be understood as a form effect due to changes in the running attitude and waterline around the vessel. Traditionally the form effect is accounted for by the form factor $(1 + k)$, which is estimated at $Fr \rightarrow 0$. A large bow down trim is required to assure the dry transom condition is achieved to estimate the form factor according to ITTC guidelines. However, this corresponds to an impractical floating condition, which is an unrealistic ship operation and may lead to inapplicable values of $(1+k)$. Alternatively, an empirically determined value for $(1 + k)$ may be chosen (Lafeber et al., 2008). Furthermore, an effect of Reynolds number on the Froude dependent part of the total resistance is also expected, because the pressure recovery at the stern is potentially influenced by the boundary layer thickness.

Thirdly, to predict full-scale resistance from model test experiments a model-ship correlation line is used which is made up of the friction line of Hughes (1954) and an inherently included form factor of 12%. Furthermore, either an experience-based correlation allowance is added that takes the scale factor, hull surface roughness, ship type and other scaling effects into account. Alternatively, an empirical allowance can be estimated for conventional ships, which according to ITTC guidelines is based on surface roughness, ship length and full-scale Reynolds number. For this novel type of vessel it is assumed that the available data for the experience-based determination of factors for model-ship correlation will not be sufficiently accurate, because the ships are significantly different in hull form and size when compared to current fast ferries or high-speed catamarans.

Finally, the ITTC recommended procedures imply that the total resistance coefficient (C_{TS}) is linearly decomposed. So that the same form factor $(1 + k)$ is assumed to be valid for all Froude numbers, that the residuary resistance coefficient (C_R) solely depends on Froude number and will neither change with increasing Reynolds number and usually does not take changing wetted surface area into account. The wave-pattern and hence wave-making resistance is scaled linearly from model to full scale even though it is known that the Reynolds number will affect the wave-making (Raven et al., 2008). Finally, simply extra drag due to surface roughness (dC_F) or experience-based allowance (C_{AA}) can be added.

$$C_{Ts} = (1 + k) \times C_F + C_{Rm} + C_{AA} + dC_F \tag{3.1}$$

where it is assumed that the terms depend on:

$$(1 + k) = f(hull\ form)$$

$$C_F = f(Re)$$

$$C_R = f(Fr,\ hull\ form)$$

$$dC_F = f(surface\ roughness,\ ship\ length,\ Re)$$

$$C_{AA} = f(Re\ or\ experience)$$

These four attributes of the ITTC-based extrapolation method emphasise the need for a tool to predict the full-scale resistance of novel surface vessel and for medium-speed catamarans in particular. An approach based on using computational fluid dynamics (CFD) is instead proposed. Raven et al. (2008) showed that CFD can be used to predict the ship performance at both model-scale and full-scale and that a difference in drag force compared to ITTC methods exists which is usually overcome by an empirical correlation allowance. Hochkirch and Mallol (2013) highlighted that the consideration of varied Reynolds number is a key advantage for CFD in full-scale powering prediction. However, validation of full-scale simulation may be difficult (Bertram, 2000) due to spatial requirements of the testing facilities and experience in its applicability is currently insufficient.

3.1.1 Scope of Study

This study introduces an approach to run numerical simulations based on Reynolds-Averaged Navier-Stokes (RANS) equations at full-scale Froude and Reynolds numbers using meshes whose spatial resolution has been verified at model scale. The shear force on smooth and rough flat plates was verified over a large range of Reynolds numbers to derive near-hull mesh parameters applicable for accurate simulations at model and full scale. Full-scale results were validated by comparing them to extrapolated model test data and resistance derived from power measurements of full-scale sea trials of a 98 m catamaran shown in Figure 3.2.

Figure 3.1: Proposed design of a 130 m medium-speed catamaran.

Figure 3.2: Image of the 98 m INCAT high-speed catamaran.

3.2 Full-scale CFD Approach

CFD has been applied to full-scale ships scale ships including large high-speed catamarans (Haase et al., 2012a). However, these results can be only directly validated when comparing to the drag force obtained for the full-scale ship. Especially for large and fast vessels it is considered to be impossible to conduct a full-scale towing test and alternatively the drag force has to be derived from self-propelled sea trial measurements (Iliopulos et al., 2013). Therefore, the novel full-scale CFD approach incorporates model test experiments to verify a spatial resolution of the flow domain for a sufficiently accurate simulation. Also, the method obeys conformity with established model-ship correlation or friction lines to conclude validity of the drag force obtained for the full-scale vessel.

Before conducting simulations for the vessel at full-scale Reynolds numbers, the calm water resistance of a scale model of the ship needs to be obtained through both numerical simulations and physical model test experiments at an identical model scale factor (λ). The simulation procedure can be considered as being verified if the resulting total resistance, and sinkage and trim agree with the experimentally measured values. Furthermore it is required that the integral value of shear force over the wetted surface area is in agreement with established model-ship correlation lines ($C_V = C_F$). If the above agreements can be achieved, it is assumed that the flow around the vessel and its physical effects on the hull are resolved with sufficient accuracy and both pressure and shear force correctly predicted at model-scale.

The Reynolds number is then changed to its full-scale value by altering the viscosity of the fluid. It is assumed that the accuracy of the pressure drag solely depends on the spatial

domain resolution and is independent of Reynolds number. Without altering the linear dimensions, flow velocity or spatial resolution of the initial mesh, a simulation at full-scale Froude and Reynolds number can now be conducted. The fluid density remains unchanged and the vessel's displacement is kept constant. If again an agreement of the shear force coefficient with values from established model-ship correlation lines is found ($C_V = C_F$) and the pressure drag is close to the value predicted at model-scale Reynolds number, it was assumed that the results are physically adequate. If required, the simulation can be continued including a certain surface roughness applied to the ship hull to include the effect of paint and marine growth on the total resistance force. With the simulation conducted at full-scale Reynolds and Froude numbers the final results are readily applicable for the full-scale ship when treated non-dimensionally. However, since they are geometrically at model-scale the results need to be multiplied by λ^3 and a relative change in density (ρ_{SW}/ρ_{FW}) to obtain the dimensional drag force for the full-scale ship. Figure 3.3 summarises the numerical extrapolation process in a flow chart.

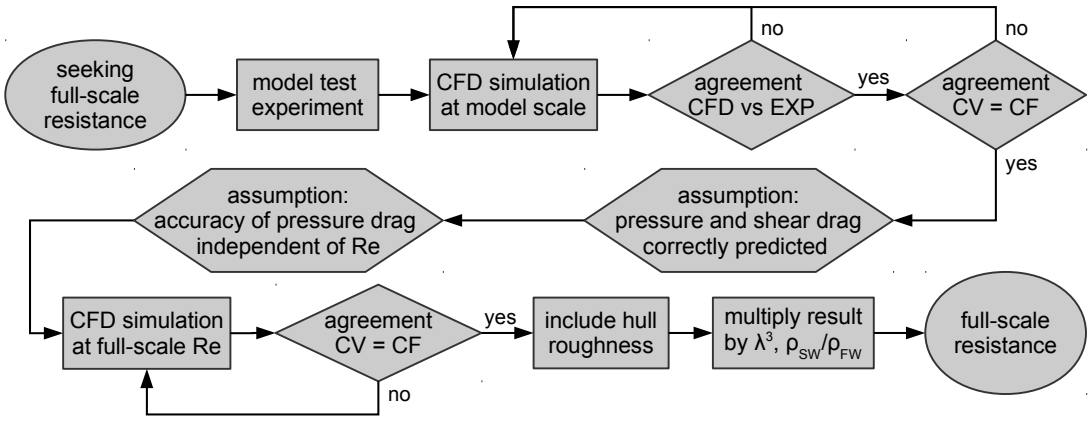

Figure 3.3: Flowchart to obtain full-scale resistance using computational grids verified at model scale. Top row contains simulations at model scale, middle row shows the assumptions made and bottom row contains simulations at full-scale Reynolds numbers.

Compared to the ITTC procedure, the numerical approach decomposes the resistance into normal (C_{Pr}) and tangential stresses (C_V), whereas both can freely change with changing Froude number, Reynolds number and hull form:

$$C_T = C_{Pr} + C_V$$

$$C_{Pr}, C_V = f(Fr,\ Re,\ hull\ form)$$

Furthermore, empirical corrections for surface roughness, finite water effects or form effects are not necessary as they are inherently included in the numerical model when solving the Reynolds-Averaged Navier-Stokes equations for the flow around the ship hull.

3.2.1 Numerical Simulation Tool

The transient solver *interDyMFoam* of the OpenFOAM CFD toolbox (version 2.3) was used for solving the RANS equations in this study unless stated otherwise. It features viscous free-surface flows and 6 degree of freedom motion to allow dynamic trim and sinkage of the vessel. *k-ω-SST* (shear stress transport) turbulence model and standard wall functions were used throughout, where wall shear stress was computed using tools from OpenFOAM version 2.0.

3.2.2 Computational Mesh Generation Strategy

The computational domain was discretised using the OpenFOAM toolbox meshing tools, including *blockMesh*, *snappyHexMesh* and *refineMesh*. It is based on a block-structured background mesh of where local refinements were made by hexagonal cell cuts, which feature hanging nodes to represent the port side of the catamaran. The distance from the demihull to the inlet as well as the width and depth of the domain was set to one hull length, and the outlet was set three ship lengths aft of the demihull. For verification with model test data, the depth and width was modelled according to the towing tank dimensions. Local refinements were made at the free-surface, in close proximity to the hull, between the demihulls, and at an area at which the Kelvin wave pattern was expected. A mesh of mainly cubic cells was developed around a model, which was longitudinally compressed by factor of four. Finally the mesh was longitudinally stretched by factor of four to obtain the desired dimensions. This meshing strategy allowed cells stretched in the main flow direction to keep the Courant number low and have a high concentration of cells in areas were high flow gradients or phase changes develop. The first cell height was chosen according to the results from Section 3.4 and set to values around $y_1 = 0.6 \times L \times 10^{-3}$ for both model and full-scale simulations with a cell expansion ratio of $r_y = 1.2$.

To identify the required number of cells a fine, medium and coarse grid were generated for the 130 m catamaran and the resulting drag force determined. The meshes consisted of 660k, 900k and 1.3M cells. Figure 3.4 shows the principle layout of cell refinement regions for the coarse mesh. Based on the results of the mesh refinement study, a typical size of 900k cells was chosen where for the 98 m and 130 m hull identical mesh strategies were used.

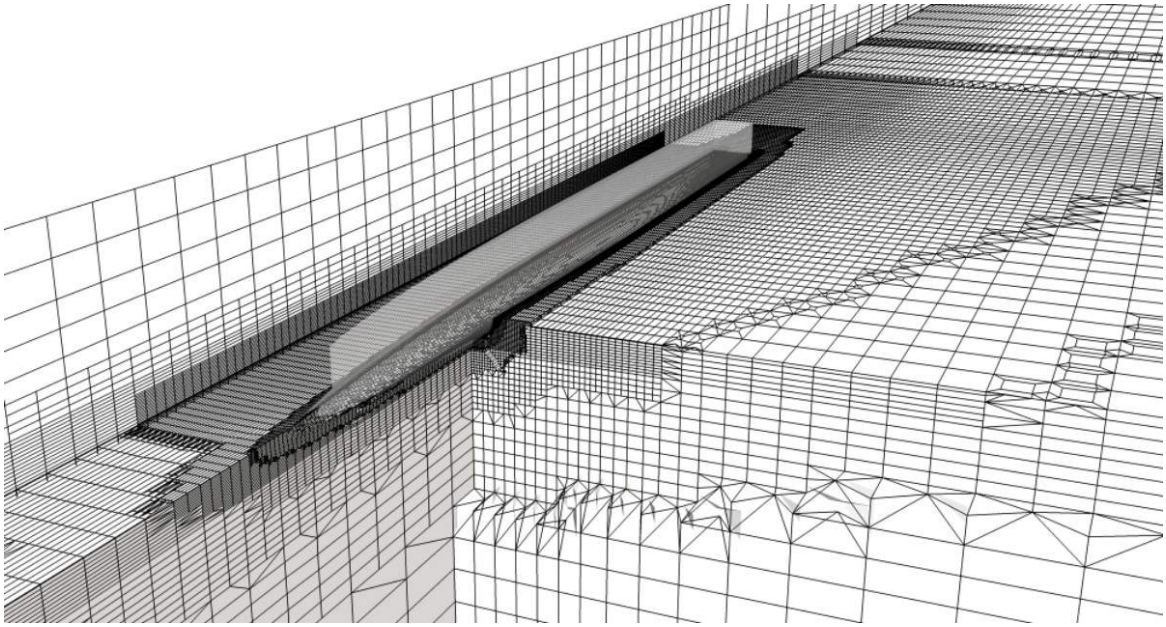

Figure 3.4: Mesh layout shown for the coarse mesh and the 130 m catamaran.

3.2.3 Verification and Validation

Before conducting CFD simulations at full-scale Reynolds numbers, the computational set-up was verified by using model-scale experiments to assure an adequate spatial resolution of the computational domain at model scale. In the current research the verification is based on towing tank experiments of a 1:50 130 m medium-speed (Davidson et al., 2011b) and 1:22 98 m high-speed catamaran (Zürcher, 2015) at Froude numbers of $Fr = 0.2 - 0.5$. Results are presented in the Section on Verification of CFD Simulations, more particularly in Section 3.3.3 and 3.3.4. The capability of accurately resolving boundary layer flows including surface roughness over a wide range of Reynolds numbers ($6.5 < log(Re) < 9.75$) is demonstrated in Section 3.4 (Verification of Near-Wall Flow). Finally, the full-scale drag value of the 98 m catamaran was validated based on power measurements from sea trials and furthermore, CFD predictions for both vessels were validated based on extrapolated model test data following ITTC guidelines (7.5-02-03-01.4). Results are presented in Section 3.5.4 entitled Comparison of Full-scale Drag for 98 m Catamaran.

3.3 Verification of CFD Simulations

Towing tank results of a 1:50 scale model of a 130 m medium-speed catamaran Davidson et al. (2011b) at displacement conditions corresponding to $L/\nabla_{dh}^{1/3} = 11.7$ and results of a

Figure 3.5: Half model of the 98 m catamaran as it was tested in the AMC towing tank.

98 m catamaran at 1:22 model scale by Zürcher (2015) were used to verify the accuracy of the CFD simulations. Both sets of experiments were conducted in the towing tank of the Australian Maritime College which is 100 m long, 1.6 m deep and 3.55 m wide, and both model were towed along the proposed thrust line. For the latter, the displacement was in accordance to a demihull slenderness of $L/\nabla_{dh}^{1/3} = 10.2$. Due to width restrictions in the towing tank only half of the hull was modelled for the 98 m vessel as can be seen in Fihgure 3.5 and consequently a single demihull was tested in close proximity to the tank wall where reflecting waves account for the hydrodynamic interaction of the opposing demihulls Zürcher et al. (2013). The distance of the demihull to the wall equalled half the demihull separation distance, an approach that was successfully utilised previously by Rovere (1997). The uncertainty for the 98 m model was reported to decrease from 3 – 1% for Froude numbers increasing from 0.2 – 0.4 (Zürcher, 2015). The main concern about this half-model approach is the limited water depth and tank length, which lead to the study in Chapter 4.

3.3.1 Mesh Sensitivity Study

The influence of the cell count on the resistance was studied using the 130 m medium-speed catamaran. Computational meshes of different spatial resolution ranging from 660k to 1.3M cells were investigated. When compared to the results for the finest mesh, the drag force obtained from the coarsest mesh deviated less than 1% for $Fr = 0.37$ and less than 2.5% for $Fr = 0.45$, and the medium sized mesh differed by no more than 0.5% at both speeds. In an earlier study Haase et al. (2012a) it was shown that accurate predictions can be made for catamarans at medium speeds over a wide range of Froude and Reynolds numbers using

comparable mesh sizes to the ones used in the current study. The same meshing routine has been used for both vessels as their principal hull form features are similar.

3.3.2 Presentation of Results

Comparisons of resistance determined by CFD and model test experiments are presented in Figure 3.6 and 3.8. While results from model test experiments are presented using hollow markers, where those of subsequent speeds were connected with thin lines for better readability, CFD results are shown by vertical bars. The total resistance (R_T) obtained from CFD was divided into a normal pressure contribution (R_P) and one from tangential stresses (R_V). In contrast, the experimentally determined drag force (R_T) was decomposed into residuary resistance (R_R) and frictional resistance (R_F) as estimated by using the ITTC model-ship correlation line. Resistance force, including its subdivisions, was non-dimensionalised by displacement, density, and gravity and further divided by Froude number squared.

3.3.3 Model-Scale Results of 98 m Catamaran

The 1:22 scale model of the 98 m vessel was simulated at Fr = 0.2, 0.31, 0.40 and 0.43 which corresponds to Reynolds numbers of $log(Re) = 6.8 - 7.1$. The results of numerical resistance predictions and model scale measurements are shown in Figure 3.6 where CFD under-estimated the total drag force by less than 5%, 8%, 8% and 2% for the respective speeds. The shear force over the wetted hull deviated by less than 10% from that predicted by ITTC model-ship correlation line, where a difference from that line was assumed to result from changing flow around the hull due to wave making, and sinkage and trim rather than uncertainties in the prediction methodology. The deep transom of the vessel leads to a major resistance hump around $Fr = 0.3$ that is not due to the interference of bow and stern wave systems, but rather is related to transom drag, as this contributes the majority of the pressure drag, as further discussed in Section 5.4.4. Figure 3.7 shows that sinkage and trim predicted by CFD and model test experiments show similar trends. However, the numerically predicted trim is up to 30% larger than the value measured in experiments and sinkage is up to twice as large as that found in the model scale experiments for $Fr \leq 0.4$. It should be noted that the towing tank length was a critical factor during data acquisition, because unsteady resistance effects occurred. ITTC guidelines (7.5-02-02-01) recommend to run the model for at least 5 cycles of those oscillations. However, due to the current set-up the number of recorded cycles was 3 for $Fr = 0.31$ and only half a cycle was resolved for $Fr = 0.43$. Therefore, deviations

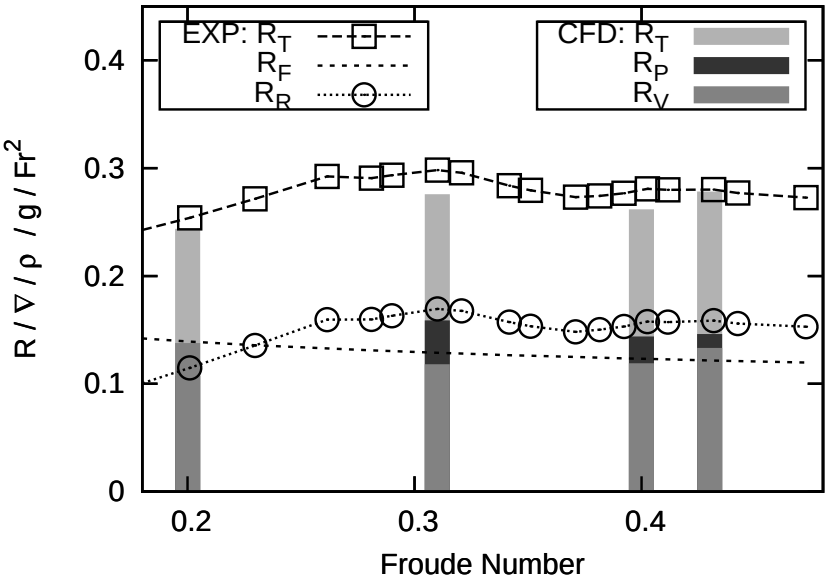

Figure 3.6: Resistance and its components was non-dimensionalised by displacement, density, gravity and further divided by Froude number squared. Drag for 98 m high-speed catamaran at 1:22 model scale determined by CFD (shown as vertical bars) and physical towing tank experiments (shown as hollow markers).

between fully converged solution from CFD simulations and model test experiments were expected.

3.3.4 Model-Scale Results of 130 m Catamaran

The calm water resistance for a 1:50 scale model of the 130 m catamaran was predicted for $Fr = 0.31 - 0.51$, which corresponds to Reynolds numbers of $log(Re) = 6.5 - 6.9$. The resulting total drag force is generally lower than that determined in the model test experiments by less than 4%, and the integral of shear stresses deviated by less than 3.5% from the ITTC model-ship correlation line. At $Fr = 0.30$ and 0.45 a hump in the resistance curve can be seen with a hollow at $Fr = 0.37$ (Figure 3.8). Furthermore, the change in dynamic attitude is well predicted by the simulation tool as shown in Figure 3.9.

3.4 Verification of Near-Wall Flow

To assess the changes in shear force coefficient with varied Reynolds number, and the conformity with established model-ship correlation or friction lines, the integral value of shear force coefficient over a two-dimensional flat plate was studied using CFD. The steady state

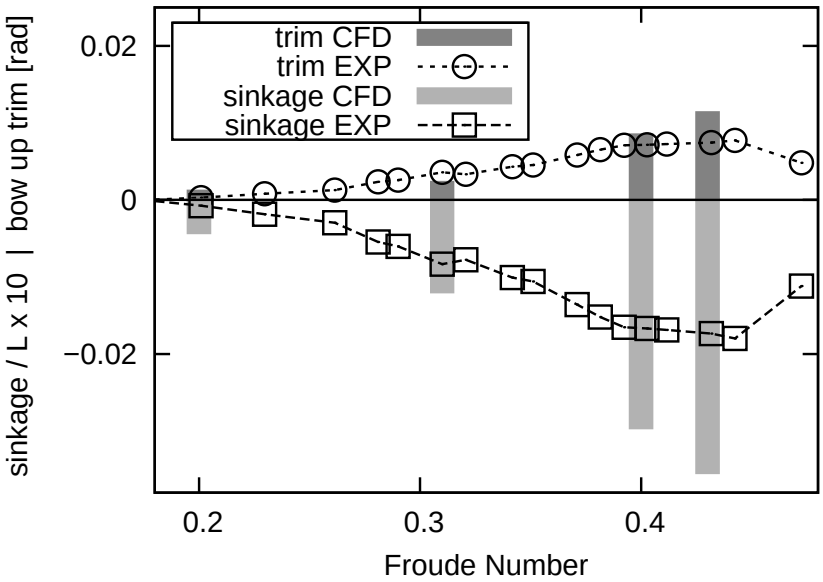

Figure 3.7: Sinkage and trim for 98 m high-speed catamaran at 1:22 model scale determined by CFD (shown as vertical bars) and physical towing tank experiments (shown as hollow markers).

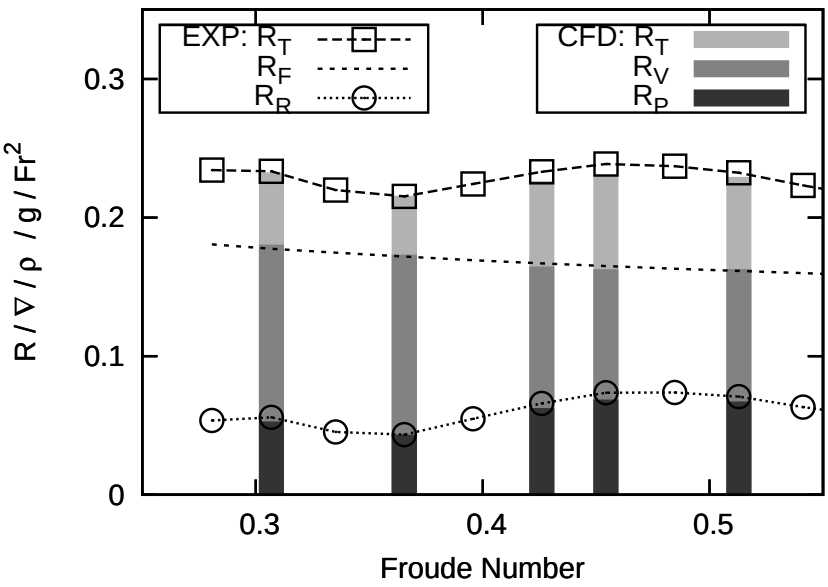

Figure 3.8: Non-dimensional resistance for 130 m medium-speed catamaran at 1:50 model scale determined by CFD (shown as vertical bars) and physical towing tank experiments (shown as hollow markers).

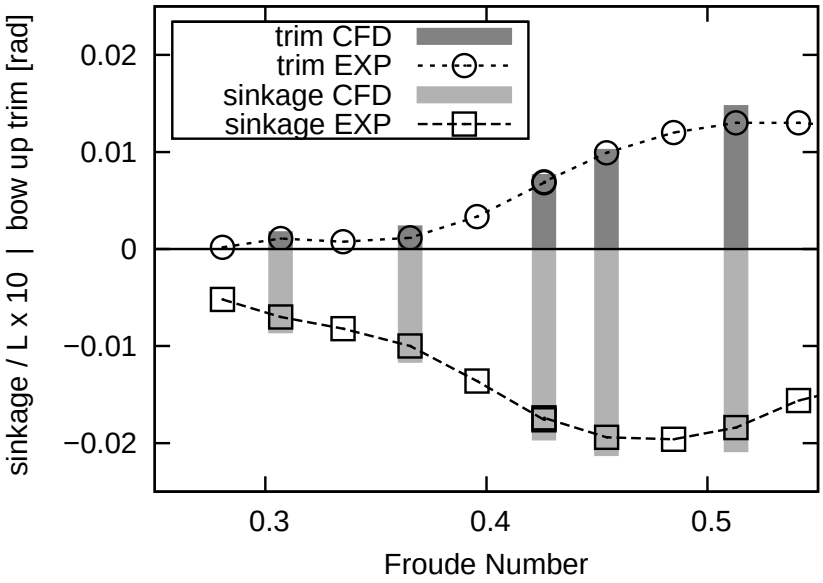

Figure 3.9: Sinkage and trim for 130 m medium-speed catamaran at 1:50 model scale determined by CFD (shown as vertical bars) and physical towing tank experiments (shown as hollow markers).

solver *simpleFoam* of the OpenFOAM CFD toolbox version 2.3 utilising SIMPLE algorithm (semi-implicit pressure-linked equation) was used for this study with standard wall function to model the near wall flow.

The flow over the flat plate was assumed to be two-dimensional to achieve an efficient simulation for a large number of variations and was conducted for $log(Re) = 6.5$, 7.0, 7.5, 8.75, 9.25, and 9.75 that correlates to Froude numbers of 0.2 to 0.5 for hull lengths of 2.5 to 200 m. This range therefore encompassed large medium-speed catamarans at both model and full scale. The flow was set to enter the domain two chord lengths in front of the leading edge of the plate and to leave five chord lengths behind the trailing edge. A free-slip wall was set one chord length opposite from the plate to bound the flow. According to White (2003) the turbulent boundary layer thickness for unity chord length was estimated to be: $y_{BL} = 0.382 \times Re^{1/5}$.

Reynolds number was effectively varied by changing kinematic viscosity, while speed and length were set to unity. Within the estimated zone of boundary layer thickness a finite number of cells was distributed with cell expansion ratios of $r_y = 1.0$, 1.1, 1.2, 1.3 and 1.5. Longitudinally the plate was resolved with 150 cells (Kouh et al., 2009), which was found to be sufficient for a mesh independent solution.

Usually, the dimensionless first cell height is expressed in terms of y^+, which conveys the distance from the wall based on the boundary layer characteristics. Resolving the boundary layer flow with $y^+ = 1$, where the velocity increases linearly with increasing distance from the wall, would require a relatively small first cell height that results in a very fine boundary layer mesh for flows at high Reynolds numbers. It can be shown that y_1 scales with $Re^{-0.93}$ which leads to a first cell height of 1,000 times finer at $log(Re) = 9.75$ compared to $log(Re) = 6.5$, which would increase the computational resource requirements and may cause numerical issues due to high aspect ratio cells (Stern et al., 2013). However, when using wall functions, the first cell height has to reach into the boundary layer where a logarithmic velocity applies. The y^+ of this region increases with increasing Reynolds number and reaches an order of magnitude of 2 at model-scale Reynolds number and an order of magnitude of 4 at full-scale Reynolds numbers. Therefore, the first cell height was made dimensionless by geometric means such as the plate length to achieve values that were comparable over a wide range of Reynolds numbers.

The results were compared against other experimentally and numerically derived friction lines, as well as model-ship correlation lines such as that of ITTC, noting that correlation lines express the change in viscous effects rather than the plain shear force on smooth flat plate. The value of numerically determined shear force coefficient (C_V) depends on the geometric properties of the computational grid, such as the first cell height (y_1) and cell expansion ratio ($r_y = y_{i+1}/y_i$) as previously shown by Eca and Hoekstra (2008). The present results led to the conclusion that for $r_y = 1$ a value of y_1 delivering the highest wall shear stress coefficient (C_{Vmax}) was the most accurate value and was used as a reference value to quantify the deviation in shear force coefficient for varying mesh parameters. Figures 3.10a -3.10c show the deviation of shear force coefficient with varying y_1 values for a range of cell expansion ratios and clearly indicate that both parameters influence the shear force coefficient. For $r_y = 1$, y_1 can be varied over a relatively wide range while still providing higher accuracy than could be ideally achieved with higher r_y values. However, if a certain deviation is acceptable, larger r_y values for resource sustainable meshes may be chosen. The first cell height providing the highest shear stress was found to be $y_1/L \times 10^3 = 1.7$, 1.0 and 0.5 for log(Re) = 6.5, 7.5 and 9.75, respectively.

This proves that an increase in Reynolds number requires a lower first cell height when using a wall function, but at a considerably lesser extent compared to when a wall function is not used. In addition it was found that the sensitivity towards increased r_y values decreases for higher Reynolds numbers. Meshes of $y_1/L \times 10^3 = 0.5 - 1.0$ with $r_y \leq 1.2$ can provide shear force coefficients with less than 2% deviation from the maximum achievable value for

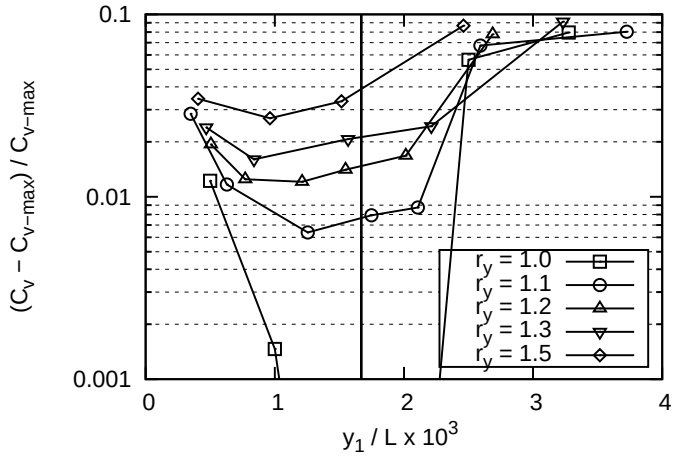

(a) $log(Re)$= 6.5

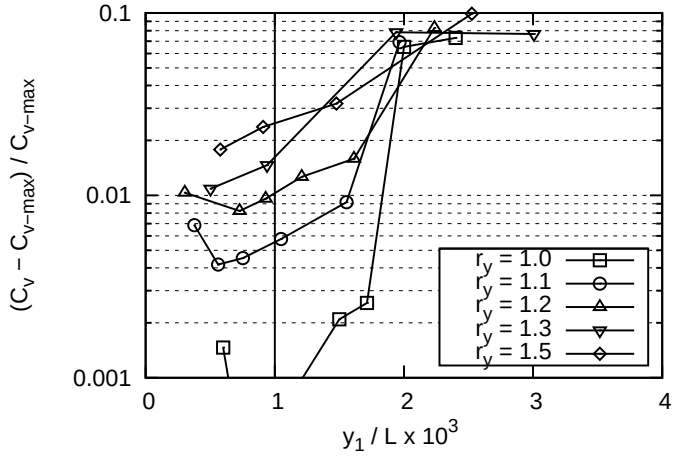

(b) $log(Re)$= 7.5

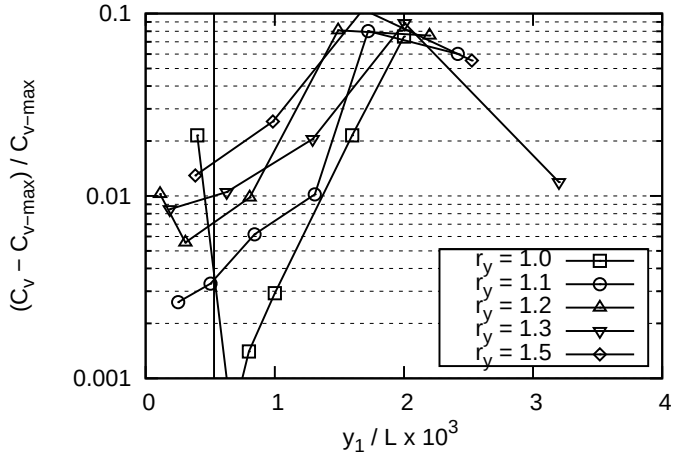

(c) $log(Re)$= 9.25

Figure 3.10: Effect of varying mesh resolution on shear force coefficient for flow over flat plate at $log(Re) = 6.5, 7.5, 9.75$ (from top to bottom). Vertical line indicates first cell height for highest achievable shear stress.

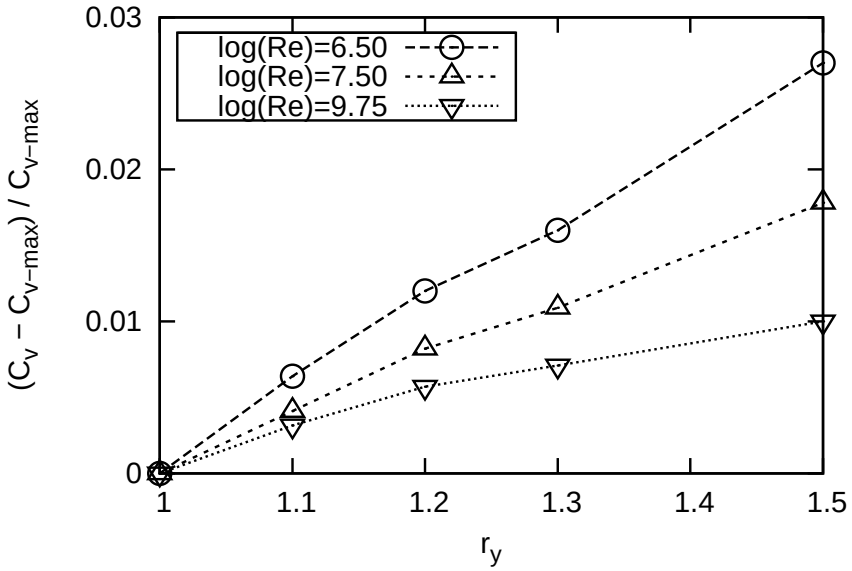

Figure 3.11: Deviation in shear force coefficient for most appropriate y_1 for varying cell expansion ratios at different Reynolds numbers.

the entire range of Reynolds numbers under consideration. This leads to the conclusion that the same mesh in the proximity of the wall can be used for both model and full-scale simulations provided that the first node height is chosen correctly. The relative deviation of shear force with respect to the highest achievable shear force with a certain cell expansion ratio was plotted at different Reynolds numbers (Figure 3.11). The curves show that the deviation at a certain cell expansion ratio is always lower at higher Reynolds numbers and leads to the conclusion that full-scale predictions are less sensitive to variations in near wall mesh properties. Even for the relatively large cell expansion ratio of $r_y = 1.5$ the shear force deviates only 1% from its most desirable solution. Therefore, at full scale higher cell expansion ratios may be allowed to reduce the cell count compared to simulations at model scale.

Finally, the results of shear force coefficient were compared to established friction and model-ship correlation lines such as those of ITTC (7.5-02-03-01.4) and Hughes (1954), Grigson (1999), and Katsui et al. (2005) Eca and Hoekstra (2008). The first four lines are defined as:

$$C_{F(ITTC)} = \frac{0.075}{(log(Re) - 2)^2}$$

$$C_{F(Hughes)} = \frac{0.067}{(log(Re) - 2)^2}$$

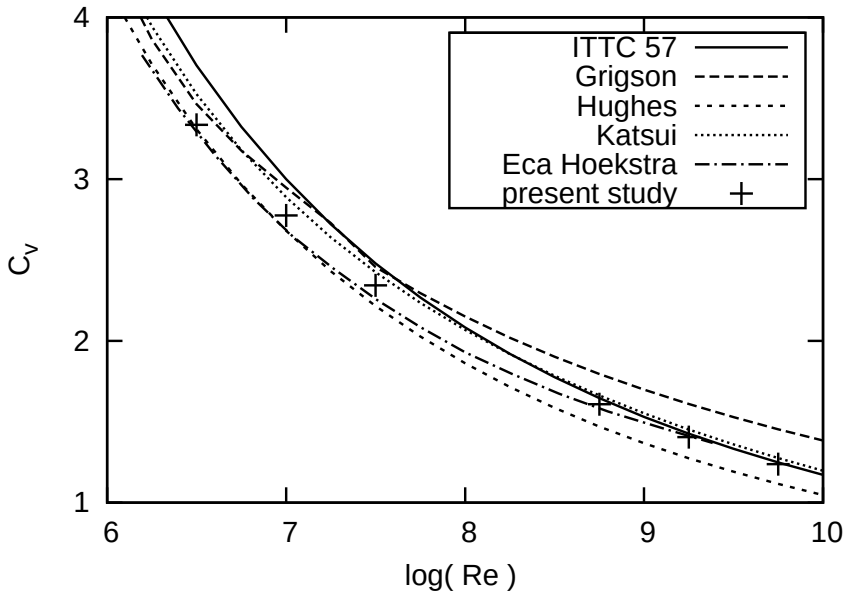

Figure 3.12: Results for shear force coefficient from present study compared to established correlation lines for model-ship extrapolation over a wide range of Reynolds numbers.

$$C_{F(Grigson)} = f_G \times C_{F(ITTC)}$$

$$f_G = \begin{cases} G_1 + G_2\left(log(Re) - F_1\right)^2 - G_3\left(log(Re) - F_1\right)^4, \ for\ 6 \leq log(Re) \leq 7.3 \\ G_4 + G_5\left(log(Re) - F_2\right) - G_6\left(log(Re) - F_2\right)^2, \ for\ 7.3 \leq log(Re) \leq 9 \end{cases}$$

$G_{1-6} = [0.93; 0.1377; 0.06334; 1.032; 0.081; -0.003273]$ $F_{1-2} = [6.3; 8.0]$

$$C_{F(Katsui)} = \frac{0.0066577}{(log(Re) - 4.3762)^{\alpha}}$$

$$\alpha = log(Re) + 0.56725$$

The line of Eca and Hoekstra (2008) was derived using CFD without using wall functions. The lines are compared in Figure 3.12 where good agreement between the current method and the results of Eca and Hoekstra were found over the whole range of Reynolds numbers. At model scale agreement with Hughes line was observed and at full-scale with the lines of ITTC, Katsui and Eca and Hoekstra.

3.4.1 Shear Force on Rough Flat Plate

A full-scale ship hull cannot be assumed to be hydraulically smooth, as its surface contains roughness due to paint, marine growth, plate dents and weld seams (Guiard et al., 2013;

Walker et al., 2014). In the numerical model the effect of surface roughness on the boundary layer flow was implemented Tapia (2009) and applied to the flat plate in terms of equivalent sand grain roughness height (k_S). Roughness values of $k_S/L = 1 \times 10^{-6}$ (SR1) and 2×10^{-6} (SR2) were chosen which correspond to a 100 μm and 200 μm sand grain roughness on 100 m long ship hull. In the range of full-scale Reynolds number ($8 < log(Re) < 10$) prediction for the shear force coefficient was made using CFD, ITTC (7.5-02-03-01.4) and an empirical estimate of Schlichting (1979). The latter assumes a fully rough wall for which the local friction coefficient solely depends on the surface roughness and not on the Reynolds number:

$$C_f = (1.89 - 1.62\ log(k_S/L)) - 2.5$$

Figure 3.13 shows that for CFD predictions at $log(Re) = 8.25-9.25$ the shear force coefficient increases with increasing Reynolds number. It branches from the curve of the shear force coefficient for a smooth flat plate and increases towards the value determined by Schlichting for a fully rough plate which corresponds to literature (White, 2003). For $log(Re) \leq 9.25$ predictions by CFD and Schlichting agree well and therefore it is assumed that the predictions are physically adequate. Contrary, the ITTC prediction for a rough surface monotonically decreases with increasing Reynolds number over the whole range of consideration. However, at $log(Re) = 8.75$ the predictions by ITTC and CFD are of comparable magnitude, whereas at lower Reynolds numbers ITTC predicts a larger impact of roughness on the drag force and a lower impact at higher Reynolds numbers. The relative increase in shear force for a relative roughness of k_S/L= 1 $\times 10^{-6}$ (SR1) and 2 $\times 10^{-6}$ (SR2) referring to equivalent sand grain roughness with respect to a smooth plate can be seen in Figure 3.14. This highlights the contrary trend of the shear force coefficient between numerical prediction and empirical estimate of ITTC for Reynolds numbers exceeding $log(Re) > 9$. Furthermore the range of Reynolds numbers for a 98 m and a 130 m at medium-speed Froude numbers of $Fr = 0.35 - 0.45$ were plotted to illustrate that the adverse effect of surface roughness is expected to be more pronounced at larger vessels or higher speeds. At $log(Re) = 9.25$ the values from CFD and Schlichting is larger by 18% and 27% for a roughness of $k_S/L = 1 \times 10^{-6}$ and 2 $\times 10^{-6}$, respectively. This emphasises that the ITTC value may either be only valid for a small range of Reynolds numbers or already includes a correlation allowance factor.

3.5 Validation of Full-scale Drag

Sea trial data and extrapolated model test data was used to validate the full-scale CFD predictions. Full-scale speeds of 12, 18, 23.5 and 25 knots for the 98 m catamaran were

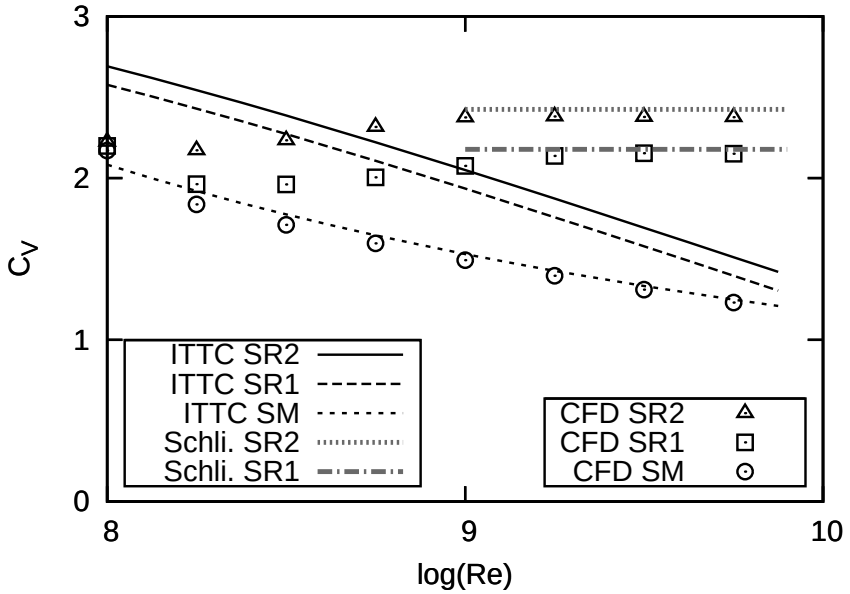

Figure 3.13: Integral values of shear force coefficient (C_V) for the flow over a flat plate being smooth (SM) and rough: $k_S/L = 1 \times 10^{-6}$ (SR1) and 2×10^{-6} (SR2). Results were obtained by CFD, ITTC (7.5-02-03-01.4) and empirically by estimating local skin friction by Schlichting (Schli.) for fully rough walls.

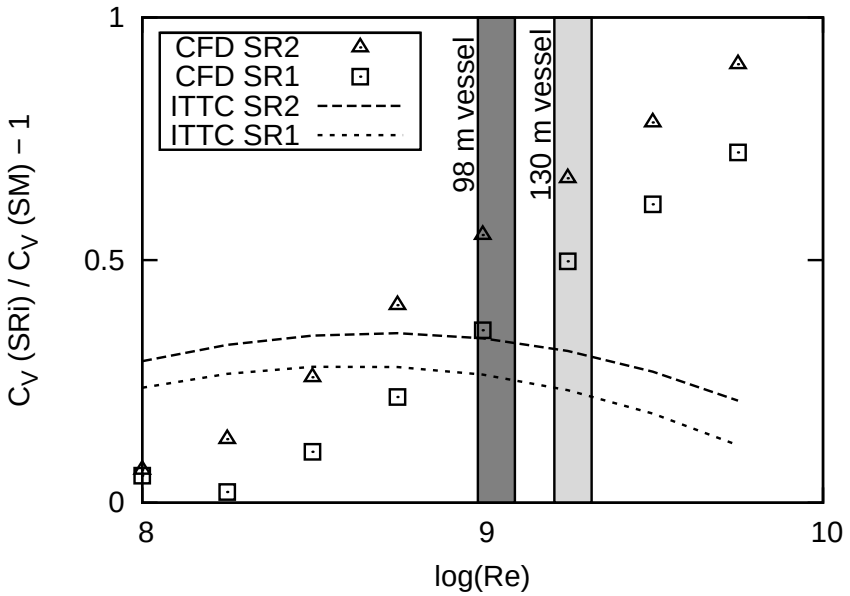

Figure 3.14: Relative increase of shear force coefficient ($C_V(SRi)/C_V(SM) - 1$) compared to hydraulically smooth plate (SM) for equivalent sand grain roughness of $k_S/L = 1 \times 10^{-6}$ (SR1) and 2×10^{-6} (SR2). Range of Reynolds number for a 98 m and a 130 m vessel at medium speeds ($Fr = 0.35 - 0.45$) are indicated.

considered which correspond to the model scale results at $Fr = 0.20$, 0.31, 0.40 and 0.43. The drag for the 130 m catamaran was predicted at hollow and hump conditions $Fr = 0.37$ and 0.45 which equals 25 and 30 knots for the full scale vessel. Reynolds numbers range from $log(Re) = 8.8 - 9.3$ when considering both cases.

3.5.1 Drag Force from Full-scale Sea Trials

Full-scale sea trials of a 98 m high-speed catamaran were conducted in the Gulf of Mexico, 80 nautical miles off the coast from Ingleside, Texas in November 2004 and the shaft power and associated speed was reported by Griggs and Woo (2005). The water was reported to be sufficiently deep ($h/L > 10$) and the weather marginal corresponding to a high sea state 2 with observed wind speeds below 25 knots and waves of 5 ft at a 7 s period . Shaft power was obtained for all four water jets using *Sensotec* clamp-on torsionmeters and averaged for each run. 2 – 3 runs per powering condition were then averaged to yield the final value. The torque measurement uncertainty was reported to be not exceeding 2% and the uncertainty of vessel and shaft speed measurement below 0.25%.

When referring to the thrust curves of the waterjet propulsors, which were made available by the manufacturer, the measured delivered power for a certain speed could be associated to a nominal thrust per waterjet unit. The obtained thrust value was considered as being equal to the resistance as it was assumed that both the thrust deduction and wake fraction were negligible, as proposed by Iliopulos et al. (2013).

3.5.2 Extrapolation of Model Test Data

Extrapolation for Deep Water

The measurements from the physical model test were extrapolated using the ITTC guidelines for conventional vessels (7.5-02-02-01.4) and high-speed marine vessels (HSMV) (7.5-02-05-01). The difference between the two methods is in their respective approaches to using a form factor, which is not recommended when utilising guidelines for HSMV due to the flow past a deep, dry transom and hence $(1 + k)$ is set as 1.0. The total resistance coefficient was calculated by:

$$C_{Ts} = C_{Tm}((1 + k) \times (C_{Fm}C_{Fs}) + dC_F + C_A + C_{AAS}$$

where C_{Tm} is the total resistance coefficient at model scale, C_F is the frictional resistance according to the model-ship correlation line of ITTC (7.5-02-02-01), dC_F the roughness allowance, C_A the correlation allowance and C_{AAS} the air resistance coefficient. The latter

coefficients can be determined as:

$$dC_F = 0.044\left((k_S/L)^{1/3} - 10Re^{-1/3}\right) + 0.000125$$

$$C_A = (5.68 - 0.6\ log(Re)) \times 10^{-3}$$

$$C_{AAS} = C_D A \times \rho_{air}/\rho_{water} \times A_{proj}/S_W$$

where k_S is the surface roughness which is assumed to be 100 and 200 μm, L the ship length, C_{DA} the drag coefficient of the superstructure which was assumed to be $C_{DA} = 0.446$ for a typical INCAT high-speed catamarans and a projected area of the superstructure of $A_{proj} = 0.04\ L^2$ (Oura and Ikeda, 2008). S_W denotes the wetted surface area. As an alternative, the Grigson line (Grigson, 1999) was utilised for model ship correlation, but the value of extrapolated resistance was between that of the two methods presented above, differing by $2-3\%$ for the speeds under consideration whereas a form factor higher than unity leads to lower results.

Finite Depth Corrections

For the model tests of the 98 m vessel the depth Froude number for the current case was relatively high ($Fr_h \leq 0.75$) and ITTC recommended procedures (7.5-02-02-01.4) were consulted for a correction of the model test experiments. The approach of Schuster (1956) was considered to correct the model test data for finite water effects such as blockage and increased wave-making to make the test data recorded in finite water applicable for unbounded water cases. The method considers the relative change of effective velocity (du/U) around the ship model, such as:

$$C_T = R_T/\left(\rho/2U^2\left(1 + du/U\right)^2 S_W\right) \tag{3.2}$$

where du/U is given by

$$du/U = m/(1 - m - Fr_h^2) + (1 - R_F/R_T)\ 2/3\ Fr_h^{10} \tag{3.3}$$

with $m = A_X/(b \times h)$. This formula predicts an increase in residuary resistance of 3% at Fr = 0.31 and 15% at $Fr = 0.43$ due to finite water effects. Since the finite water effects appear not to be negligible for the current case, this approach was utilised for extrapolation of the model-test data of the 98 m high-speed catamaran.

3.5.3 Full-scale CFD Results

The full-scale resistance from the CFD data was obtained by repeating the simulations using model-scale dimensions at full-scale Reynolds numbers, with an extended domain to ensure that finite water effects did not significantly affect the results. The depth of the domain was extended to $h/L = 1.0$ in accordance with ITTC guidelines (7.5-03-02-03) and surface roughness was taken into account in the numerical model (Tapia, 2009). Since the original surface roughness of the full-scale vessel at the time of operation was unknown, the values of $k_S = 100$ and 200 μm were used. Whilst according to ITTC recommended procedures (7.5-02-02-01.4), 150 μm should be chosen if the exact value is not known, using two values allows an estimate of varied surface roughness on the effective power, as the boundary layer around the ship is influenced by hull imperfections that add to the initial surface roughness, such as due to weld lines, plate dents, difference in plate thickness and marine growth.

A correction for air drag was added in an identical approach to that for the extrapolated model test data. This resistance component could also have been determined using CFD, but that was considered as being beyond the scope of this work. Furthermore, the air drag was neither subject to laminar-turbulent transition effects nor Froude number dependent scaling and therefore the current approach is considered to be appropriate.

3.5.4 Comparison of Full-scale Drag for 98 m Catamaran

A detailed comparison of resistance from the different prediction methods including 100 and 200 μm surface roughness can be seen in Figure 3.15. The resistance was subdivided as specified in section 3.2 with additionally taking into account the drag due to surface roughness (RdCF (ITTC)), correlation allowance (RA (ITTC)) and wind drag due to the superstructure (RAA (ITTC)), as proposed by ITTC (7.5-02-02-01.4). In the numerical simulation the drag due to surface roughness (RdCF (CFD)) was determined by the difference in drag due to tangential stresses for cases with and without surface roughness included, as it cannot be separately isolated.

For speeds at $Fr = 0.20$ and 0.31 the CFD prediction was below the result obtained from power measurements of sea trials by 20 – 23% and 5 – 10% depending on the surface roughness applied. For $Fr = 0.40$ and 0.43 the drag obtained from CFD deviated by 1 – 5% and -3 – 3%, respectively. For the latter two speeds the extrapolated model test data was within the numerically predicted values. Numerical differences of the different prediction methods are

Table 3.1: Relative deviation of predicted drag for 98 m catamaran using CFD and extrapolated model test data corrected for shallow water by the approach of Schuster (1956) with and without form factor with respect to drag derived from full-scale powering measurements. k_S of 100 μm and 200 μm was considered.

		Relative deviation of total resisitance CFD prediction and extrapolated model tests vs results from sea trials measurements				
		CFD		ITTC extrapol. model test		
Speed	$(1+k)$	N/A		1.0		1.18
$[kn]$	k_S	100 μm	200 μm	100 μm	200 μm	
12		-0.234	-0.197	-0.406	-0.399	-0.438
18		-0.098	-0.050	-0.125	-0.117	-0.158
23.5		0.005	0.049	0.009	0.018	-0.030
25		-0.026	0.030	0.007	0.017	-0.031

presented in Table 3.1. The deviations are relative to the value obtained from the sea trial measurements and expressed as: $R_{T(CFD)}/R_{T(sea\ trial)} - 1$.

The differences in resistance components are summarised in Table 3.2. For $Fr = 0.20$ the differences between pressure and residuary drag are between 49% and 104%, but the shear force over a smooth hull is only 1% larger in CFD. When considering surface roughness the relative difference increases to 10% and 23% for 100 and 200 μm of equivalent sand grain roughness. For speeds from $Fr = 0.31$ to 0.43 the maximum deviation of pressure resistance when compared to residuary resistance is less than 8% and 11 – 23% when using a form factor. If the latter is used the viscous drag force in CFD is under-estimated by 19% whereas this difference decreases to below 5% when no form factor was used for a smooth hull. When including surface roughness, CFD delivers results that are less than 4% higher than ITTC predictions for 100 μm and 15 – 16% higher when 200 μm of equivalent sand grain roughness is assumed. However, one has to bear in mind that the ITTC approach uses a friction line that includes a constant form factor, but does not take varying wetted surface are into account.

3.5.5 Comparison of Full-scale Drag for 130 m Catamaran

The numerical predictions were compared to the extrapolated model test data following ITTC recommendations with a form factor ($(1 + k) = 1.1$) and without, and a smooth surface as well as surface roughness of 100 and 200 μm of equivalent sand grain roughness was included.

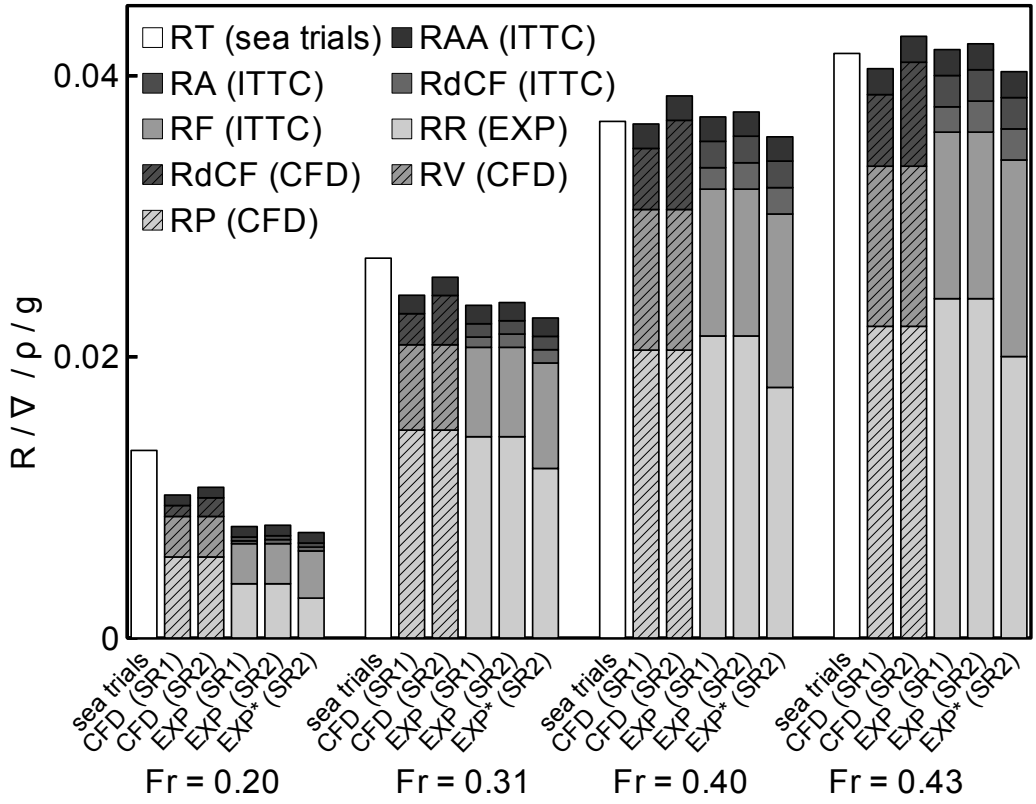

Figure 3.15: Full-scale drag predictions for the 98 m medium-speed catamaran from model test experiments (EXP) (with and without form factor, * indicates usage of form factor of $(1+k) = 1.18$) and CFD (CFD) at $Fr = 0.20$–0.43 at two levels of surface roughness. SR1: $k_S = 100\mu$m, SR2: $k_S = 200\mu$m.

Table 3.2: Relative deviation of resistance components of 98 m catamaran determined by CFD and extrapolated model test experiment for a smooth hull. Positive values indicate that CFD prediction exceeds extrapolated quantity.

		Relative deviation of resistance components CFD vs extrapolated model test results					
		RP/RR – 1			RV/RF – 1		
	$(1+k)$:	1.0		1.18	1.0		
Fr	k_S :	smooth				100 μm	200 μm
0.20		0.49	1.04	-0.15	0.01	0.10	0.23
0.31		0.03	0.23	-0.19	-0.05	0.03	0.16
0.40		-0.05	0.15	-0.19	-0.04	0.04	0.15
0.43		-0.08	0.11	-0.19	-0.04	0.04	0.15

Table 3.3: Relative deviation of resistance components of 130 m catamaran determined by CFD and extrapolated model test experiment. Positive values indicate that CFD prediction exceeds extrapolated quantity.

		Relative deviation of total resistance CFD vs. and extrapolated model test results				
		RT/RT – 1				
	$(1+k)$:	1.0	1.1	1.0		1.1
Fr	k_S :	0 μm, $C_A = 0$		100 μm	200 μm	
0.37		0.045	0.128	0.171	0.212	0.274
0.45		-0.047	0.022	0.113	0.140	0.218

At $Fr = 0.37$ the CFD-predicted resistance for a smooth hull was 5 – 13% larger than extrapolated model test results, depending if a form factor was used or not. The discrepancy increased to 17 – 27% if a surface roughness of 100 and 200 μm was taken into account. At $Fr = 0.45$ the difference between the CFD prediction and extrapolated model test data was below 5%, but reached values of 11 – 21% with surface roughness included in the prediction method.

Figure 3.3 shows the agreement between the CFD predictions and extrapolated model test results including a subdivision into resistance components and Table 3.3 shows a quantitative comparison of total resistance. Table 3.4 quantifies the relative difference in pressure related (RP) and residuary (RR) resistance when using form factor and when not for both speeds. Furthermore, it shows the relative differences in viscous resistance (RV) with respect to frictional resistance (RF) for a smooth hull and also with included roughness and correlation allowance as obtained by ITTC (7.5-02-02-01.4). Residuary resistance deviates up to 57% and 13%, while frictional resistance deviates below 11% and 5% when using and not using a form factor. For (1+k) = 1.0 the frictional resistance including roughness and correlation allowance is 44 – 56% higher in CFD prediction than it is compared to empirically determined values when following recommendations by ITTC (7.5-02-02-01.4).

3.6 Discussion

3.6.1 Full-Scale Drag From Sea Trials

A CFD-based approach, which uses verification with model test experiments, to determine the full-scale resistance of a surface vessel was presented in section 3.2. The results from using this approach for a 98 m catamaran were validated using resistance values obtained

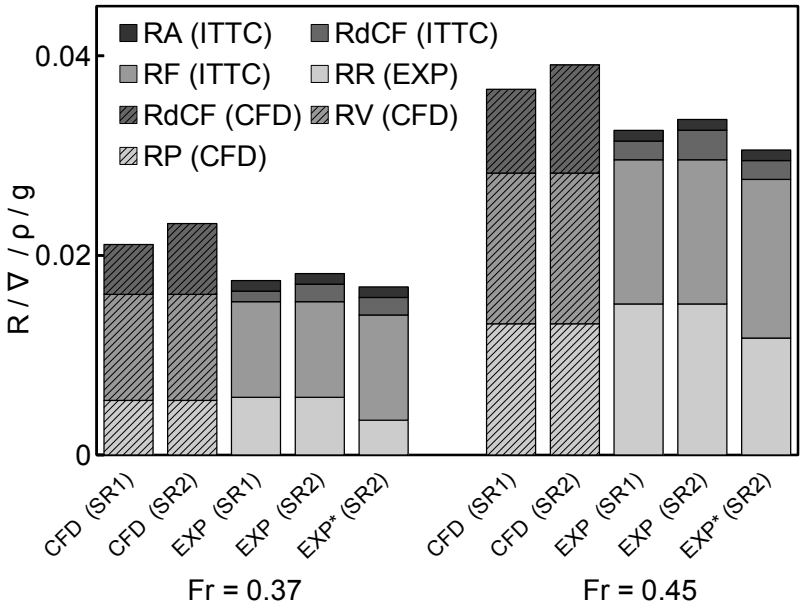

Figure 3.16: Full scale drag predictions for the 130 m catamaran from model test experiments (EXP) (with and without form factor, * indicates $(1 + k) = 1.10$) and CFD (CFD) of bare hull with no superstructure of the 130 m medium-speed catamaran at $Fr = 0.37$ and 0.45 at two levels of surface roughness. SR1: $k_S = 100\mu$m, SR2: $k_S = 200\mu$m.

Table 3.4: Relative deviation of resistance components determined by CFD and extrapolated model test experiment. Positive values indicate that CFD prediction exceeds extrapolated quantity.

	Relative deviation of resistance components: CFD vs extrapolated model test results					
	RP/RR-1			RV/RF 1		
$(1+k)$:	1.0	1.1		1.0		
k_S :	0 μm, $C_A = 0$				100 μm	200 μm
0.37	-0.05	0.57	0.11	0.01	0.47	0.56
0.45	-0.13	0.12	0.04	-0.05	0.44	0.49

from power measurements at full-scale sea trials. All three approaches (CFD simulation, model test extrapolation and sea trial estimates) showed a deviation below 5% for $Fr = 0.40, 0.43$. However, the resistance from the sea trials was larger at $Fr = 0.20, 0.31$ by up to 44%. To the candidate's knowledge the effect of thrust deduction can be considered as being negligible for $Fr > 0.35$ (Lafeber et al., 2008), but wake fraction will have values around $w = 0.1$, which is in accordance with estimates by Bulten (2006) and de Cock et al. (2011). For speeds of $Fr < 0.35$ values of thrust deduction may tend towards unity with decreasing speed while wake fraction remains unchanged (Lafeber et al., 2008). Taking wake fraction and thrust deduction into account resistance can be determined by: $R_T = (1-t)/(1-w) \times T$

Hence the resistance when utilising the proposed method will be under estimated by 10% for $w = 0.1$ and $t = 0.0$ and over estimated by 45% for $w = 0.1$ and $t = 0.5$. However, an agreement for $Fr \geq 0.4$ between the result from sea trials, when neglecting wake fraction and thrust deduction, and the CFD full-scale prediction and model test data extrapolation was shown. Thus it can be assumed that the effect of thrust deduction and wake fraction can either be neglected or is counteracted by environmental influences such as wind and waves, marine growth on the hull or mechanical losses resulting from assemblage of the propulsion plant. The deviation in drag predictions for speeds of $Fr < 0.4$ leads to the conclusion that the thrust drag equilibrium is not valid for this particular speed range, which may be explained by the not fully ventilated transom stern.

Iliopulos et al. (2013) state that neglecting wake fraction and thrust deduction to obtain resistance from thrust effectively is the inverse procedure of choosing a waterjet size for a given resistance. Therefore, this method has to be considered as being practical rather than physically accurate.

3.6.2 Correlation Allowance

The results for the 130 m catamaran show that the additional resistance due to a rough surface exceeds the correlation allowance estimated by ITTC (7.5-02-03-01.4). For large vessels the recommended correlation allowances, including roughness allowance can be smaller than zero (Bertram, 2000). This originates from the correlation of full-scale sea trials and model test experiments of conventional ships, but it is physically unreasonable that including surface roughness reduces the total drag. A possible reason could be that using the ITTC model-ship correlation line over-estimates the viscous and residuary resistance components at such large Reynolds numbers ($log(Re) > 9.0$) which needs to be compensated. However, considering the results in section 3.4 and 3.5.5 this would imply that near-wall flows for smooth and rough

surfaces are incorrectly predicted by CFD and empirical approaches under consideration. Another possibility is that the propulsion plant may be working more efficiently at such large Reynolds numbers due to reduced viscous losses. Therefore, a total resistance below the physically accurate drag force can be considered for choosing an appropriate engine size. Further research is required to numerically quantify added resistance due to surface roughness when Reynolds number exceeds $log(Re) > 9.0$.

3.6.3 Verification of CFD Simulations

The verification of the CFD set up was necessary to assure that the main flow features were sufficiently accurately resolved. For the current vessels these features may include the wave-making, the demihull interaction, and the flow separation at the transom stern. Therefore, a successful verification allows to use the spatial resolution specified at model scale for accurately predicting the full-scale resistance of similar ships that provide comparable geometric and hydrodynamic features. Based on the current example the candidate claims legitimacy of the set up for reasonable changes in slenderness, transom immersion, or draft. However, if the vessel shape is considerably different, such as being a monohull vessel or having features including a pronounced fore shoulder or strongly convex buttock or water lines in the aft section a reverification of the CFD set up may be required. A geometrically identical or at least similar hull form should be used to assure that results for the full-scale drag are physically meaningful.

3.7 Conclusions

A novel CFD-based methodology was developed and it was shown that it is capable of accurately predicting the full-scale resistance of a marine surface ship in conjunction with model test experiments within 5%. Hence it is proposed as a numerical tool for model test result extrapolation. The predictions were successfully validated for large medium-speed catamarans by comparison with results obtained from full-scale measurements.

The CFD simulations were found to be capable of estimating the drag of medium-speed catamarans at 1:50 and 1:22 model scale, with deviations in resistance being below 8%. Shear force was found to be at an agreed level of accuracy with several friction and model-ship correlation lines for both model-scale and full-scale Reynolds numbers and it was shown that an identical near wall mesh resolution can be used throughout the entire range of Reynolds numbers under consideration ($6.5 < log(Re) < 9.75$). Full-scale Reynolds numbers were

achieved in the simulation by altering viscosity and keeping the linear dimensions at model scale, which allows the use of the same meshes at both model-scale verification and full-scale prediction. Furthermore, the effect of surface roughness was included by shifting the wall functions' velocity profile of the logarithmic region, depending on the desired amount of surface roughness. It was found that for $log(Re) > 8.75$ the impact of roughness on the total drag is more pronounced in CFD simulations when compared to the empirical suggestion from ITTC, while CFD predictions for the flow over a flat plate for fully rough conditions agreed with values found in literature on flow physics.

A validation of the full-scale resistance obtained by CFD simulations was conducted using resistance force derived from sea trials and extrapolated model test data. The full-scale drag derived from sea trials was assumed to be equal to the waterjet thrust, which was obtained from provided thrust curves and the measured shaft power. For $Fr \geq 0.40$ deviation of the CFD result was below 5% from the full-scale reference values; the same agreement was achieved for the different model test extrapolations. For $Fr \leq 0.31$ the CFD prediction was between 5 – 23% below the sea trial estimate, while model test extrapolation was 12 – 44% below values estimated from sea trials. When considering the 130 m catamaran for $Fr = 0.37$ the CFD prediction was 17 – 27% larger than extrapolated model test results, depending on extrapolation method and surface roughness and 11 – 21% larger for $Fr = 0.45$. Full-scale resistance considering a smooth hull was 5 – 13% higher when predicted by CFD at $Fr = 0.37$, while at $Fr = 0.45$ smooth hull resistance varied only from -5 – 2%. Small changes in vessel geometry may be allowed without verifying the CFD set up all over again, which makes this a powerful tool for hull form studies at full scale. However, when significant changes to the ship hull shape are applied, the CFD set up may need to be verified with an applicable model test comparison to assure the delivery of accurate results.

This study underlined the versatility of computational fluid dynamics in the ship design evaluation process and its applicability for full-scale simulations that take surface roughness into account and includes a level of accuracy for resistance prediction which can exceed that of extrapolated of model test results. Furthermore it highlights the importance of, but also the difficulty of, applying an appropriate roughness and correlation allowance to large medium-speed catamarans, especially when Reynolds numbers reach such high values.

3.7.1 Recommendation for Future Work

A method to further refine the validation approach may need to be developed to avoid the uncertainties that are associated to the waterjet system, when deriving the drag force from shaft power measurements.

Also, the allowance for model-ship correlation and surface roughness at Reynolds numbers exceeding $log(Re) > 9.0$ needs to be subject to further investigation.

Where to next?

Now that the new full-scale CFD approach, verified by model test experiments, has been introduced and validated, its accuracy in predicting drag for a vessel operating in restricted water will be investigated in Chapter 4. This is an important issue since limitations in water depth and channel width may significantly influence the drag force of the ship when in operation or when its drag is being predicted in model experiments.

Chapter 4

Full-Scale Resistance Prediction in Finite Waters – A Study Using CFD Simulation, Model Test Experiments and Sea Trial Measurements

This chapter has been submitted for publication and is under peer review. The current citation for the research article is:

M. Haase, G. Davidson, J. Binns, G. Thomas, and N. Bose (2015a). "Full-Scale Resistance Prediction in Finite Waters A Study Using CFD Simulation, Model Test Experiments and Sea Trial Measurements". In: *Proceedings of the Institution of Mechanical Engineers, Part M: Journal of Engineering for the Maritime Environment* under review

---

The current version of this chapter has been modified compared to the submitted version to guide the reader more conveniently through this thesis.

Abstract

Shallow water may considerably amplify the wave-making and hence the overall drag force of catamarans operating around the main drag hump speed. Computational fluid dynamics (CFD) is used to predict the drag force of medium-speed catamarans at model and full scale in infinite and restricted water to study the impact on the resistance. Steady and unsteady shallow water effects that occur in model testing or full-scale operation are taken into account using CFD as they are inherently included in the mathematical formulations. Unsteady effects in the ship model response were recorded in model test experiments, CFD simulations and full-scale measurements and found to agree well with each other. For a medium-speed catamaran in water that is restricted in width and depth, it was found that CFD is capable of accurately predicting the drag with a maximum deviation of no more than 6% when compared to experimental results at model scale. The influences of restricted depth and width were studied using CFD where steady finite width effects in shallow water and finite depth effects at finite width were quantified. Full-scale drag from CFD predictions in shallow water ($h/L = 0.12 - 0.17$) were found to be between full-scale measurements and extrapolated model test results. Finally, it is shown that current extrapolation procedures for shallow water model tests over-estimate residuary resistance by up to 12% and underestimate frictional forces by up to 35% when compared to validated CFD results. This study concludes that CFD is a versatile tool to predict the full-scale ship resistance to a more accurate extent than extrapolating model test data and can also be utilised to estimate model sizes that keep finite water effects to an effective minimum.

4.1 Introduction

Large medium-speed catamarans will be designed to efficiently operate around the main resistance hump where wave-making is the main contributor to the overall resistance. However at this particular speed range vessels are prone to encounter a significant increase in resistance when they operate in shallow water, as the flow field around the vessel changes such that the effective flow velocity and wave-making increases (Schuster, 1956; Tamura, 1972).

When considering the effect of shallow water, the influence of restricted water width should be considered as well. The physical effect of blockage that leads to an increased flow velocity around the hull is influenced by both limited depth and width. Consequently, the influence of finite waters on the vessel performance is addressed in this chapter. Effects of finite water are not only measurable during ship operation, but also during performance prediction where the ship model can encounter steady and unsteady finite water effects which can potentially distort model test results. Steady finite water effects can lead to an increase in resistance due to increasing flow velocities as a result of blockage that is the limited canal cross section with respect to the vessels cross sectional area. Also drag can increase due to increasing wave-making as a result of encountering low water depth that is expressed in terms of depth Froude number $\left(Fr_h = V \;/\; \sqrt{g \times h}\right)$. However, unsteady finite water effects lead to an increase in the period of oscillations in resistance and running attitude, namely sinkage and trim. They are known to occur in model testing and when mathematically describing the transient flow around the vessel (Wehausen, 1964; Day et al., 2009). The oscillation period is dictated by the towing speed, but it can grow in shallow water so that less than one oscillation cycle may be recorded within one run which leads to inaccurate results when averaging the transient data record. According to model test experiments (Davidson et al., 2011a) the required effective power of a medium-speed catamaran can increase up to 55% at $Fr = 0.45$ when the water depth drops to $h/L = 0.24$, and full scale measurements of Griggs and Woo (2005) revealed that the necessary power can more than double if water depth drops to around $h/L = 0.12 - 0.17$. This implies a speed loss of a vessel with a propulsion plant designed to operate in deep water around hump speed of 13% and 25% for $h/L = 0.24$ and 0.14. This emphasises that finite water can have a significant impact on the performance of medium-speed catamarans. Therefore, a reliable and universal prediction tool such as computational fluid dynamics is desirable that inherently includes finite water effects to account for its impact on the vessel's full-scale performance in the early design stage.

4.1.1 Scope of Study

This chapter reports on a study into the steady and unsteady effect of finite water on resistance prediction using physical model testing, numerical simulations, and data from full-scale sea trials of large medium-speed catamarans at varying water depth and width. Towing tank experiments were used to verify the accuracy of numerical resistance predictions in finite water and an approach to utilise these CFD simulations for full-scale drag predictions is introduced. Two case studies featuring 98 m and 130 m catamarans (see Figure 3.2 and 3.1 in the previous Chapter) are presented that show the difficulties that may arise in full-scale drag prediction for vessels in finite waters when using model test experiments and conventional ITTC procedures.

4.2 Numerical Prediction Methodology

In the beginning of this chapter the numerical resistance prediction method is introduced and verified for shallow water applications at model scale. The same approach was presented in an earlier study for deep water cases where a deviations in resistance below 5% were achieved when compared to results from model test experiments.

4.2.1 Numerical Simulation Tool

As introduced in the previous chapter, the current study utilised the solver *interDyMFoam* of the OpenFOAM CFD toolbox (version 2.3) to solve transient RANS (Reynolds-Averaged Navier-Stokes) formulations. It includes motions in 6 degrees of freedom to enable dynamic trim and sink of the vessel travelling in viscous fluid with a free water surface. Close to the hull the flow was modelled by standard wall functions and the $k-\omega-SST$ (shear stress transport) turbulence model. Also a similar mesh generation strategy was applied, with the only difference being that a base mesh with maximum considered width and depth was generated and for smaller required values of width and depth the mesh was trimmed accordingly.

4.2.2 Verification of numerical model

A 1:50 scale model of a 130 m catamaran was used to verify the results of the numerical prediction by comparing them to model test measurements in identical shallow water conditions of $h/L = 0.24$, where a depth Froude number of unity occurs at the resistance hump where

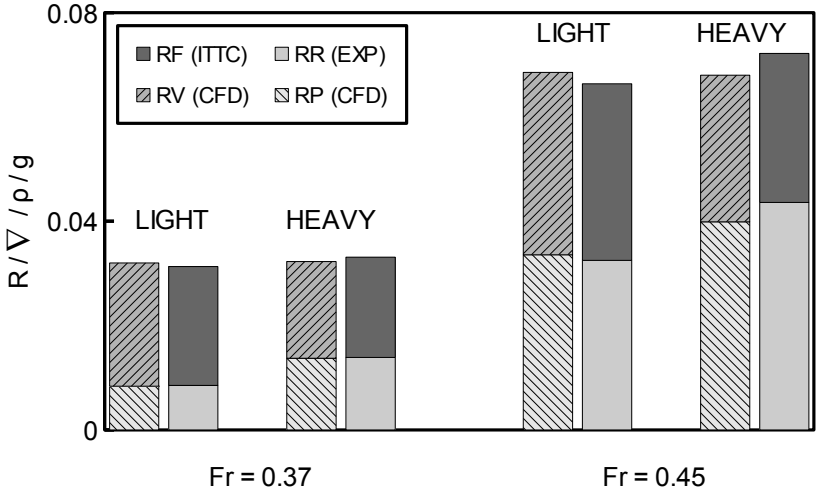

Figure 4.1: Calm water resistance of a 1:50 scale model of the 130m medium-speed catamaran in shallow water ($h/L = 0.24$) for $Fr = 0.37$, 0.45 for heavy and light displacement subdivided into a frictional (RF, RV) and pressure related components (RR, RP).

the length Froude number equals 0.49. This can be considered as the worst case scenario for a vessel operating around hump speed.

The experiments were performed at the AMC towing tank as reported by Davidson et al. (2011a). Here, results at Froude numbers of $Fr = 0.37$ and 0.45, which correspond to depth Froude numbers of $Fr_h = 0.76$ and 0.92, are considered. The results were determined for a light and heavy displacement corresponding to $L/\nabla_{dh}^{1/3} = 10.2$ and 11.7 and results of numerical and experimental predictions can be seen in Figure 4.2. They were non-dimensionalised by displacement, density and gravity ($R' = R \ / \ (\nabla \times \rho \times g)$. The total drag obtained from model test experiments was subdivided into a frictional part (RF, as determined by ITTC model-ship correlation line) and residuary resistance (RR). Numerical results were divided into drag from shear stresses (RV) and normal pressure (RP). Numerical values for the relative difference between CFD and model test predictions with respect to experimental results ($R_{T(CFD)}/R_{T(EXP)} - 1$) are presented in Table 4.1 and a deviation below 6% was achieved. This is as an acceptable accuracy, because the largest deviations occur at $Fr = 0.45$ where the depth Froude number approaches unity ($Fr_h = 0.92$), where uncertainties in model testing increases and the drag force does not converge as it does at lower speeds or deeper water. These unsteady effects are discussed below in section 4.3.2.

Table 4.1: Relative difference between numerical simulations and towing tank results of the 1:50 130 m catamaran. Negative values indicate that the CFD result is below the experimentally determined value.

	Relative deviation of resistance components: CFD vs model scale experiments					
	LIGHT			HEAVY		
Fr	$RT/RT-1$	$RV/RF-1$	$RP/RR-1$	$RT/RT-1$	$RV/RF-1$	$RP/RR-1$
0.37	0.022	0.037	-0.019	0.033	0.033	0.033
0.45	-0.025	-0.036	-0.010	-0.058	-0.016	-0.085

4.3 Finite Water Effects

Water restricted either in depth or width can influence the vessel performance due to an increased flow velocity around the vessel which is considered as blockage. Also increased wave-making will occur if the combination of speed and water depth results in a critical depth Froude number close to unity, which is defined as $Fr_h = V \ / \ \sqrt{g \times h}$ with h being the water depth. While this is a steady effect, an unsteady phenomenon occurs, due to the full-scale ship or towing tank model acceleration, which causes oscillatory behaviour for the drag, sinkage and trim.

4.3.1 Steady Finite Water Effects

A numerical investigation into the effect of restricted water on the steady state drag force in model scale testing is reported in this section. Model scale results from CFD or physical testing may be influenced by the limited width and depth of the experimental facility, which do not concur with the prospective operational conditions of the full-scale vessel. Especially for vessel operation around hump speed, the power requirements may double in shallow water conditions compared to deep water and therefore insights into performance variations due to finite waters are of great importance (Griggs and Woo, 2005). Furthermore, it was found that shallow water effects are more pronounced for vessels at a heavier displacement (Griggs and Woo, 2005; Davidson et al., 2011a).

Finite Width Effects

Firstly, the influence of the domain width on the resistance of a 130 m medium-speed catamaran (Davidson et al., 2011a) was numerically studied for $b/L = 1.4$, 3.5 and 8.75 for a shallow water case at $Fr = 0.37$ and 0.45 with $h/L = 0.24$. This corresponds to depth

Froude numbers of $Fr_h = 0.76$ and 0.92. The resistance was determined at three different domain widths and a value for an infinitely wide tank was determined using the generalised Richardson extrapolation. At $Fr = 0.37$ and $b/L = 1.4$ the residuary resistance was 15% above the value for an infinitely wide tank and below 1% for $b/L = 3.5$ and 8.75. For the higher speed at $Fr = 0.45$ the residuary resistance was above the value for an infinitely wide domain by 39%, 10% and 2% for $b/L = 1.4$, 3.5 and 8.75. At $Fr = 0.45$ the depth Froude number is close to unity, which may cause a significantly lower order of convergence when compared with cases for lower Froude depth numbers. The results are summarised in Table 4.2 where the relative difference in residuary resistance compared to an infinitely wide domain (finite vs. infinite depth) is expressed as: $C_R(b/L)$ / $C_R(b/L = \infty) - 1$. Figure 4.2 shows the convergence of residuary resistance with increasing domain width for $h/L = 0.24$ indicated by dotted lines.

Finite Depth Effects

Secondly, the influence of varying water depth on the resistance was studied at a constant tank width of $b/L = 1.4$. The model of the 130 m medium-speed catamaran (Davidson et al., 2011a) was simulated at $h/L = 0.24$, 0.6 and 1.5 at $Fr = 0.37$ and 0.45 with the effective depth Froude number varying from $Fr_h = 0.30$ to 0.93. A value for infinitely deep water was determined using the generalised Richardson extrapolation.

At $Fr = 0.37$ the residuary resistance was 15% and 2% above that of an infinitely deep tank for $h/L = 0.24$ and 0.60 and 167% and 3% at $Fr = 0.45$. For $h/L = 1.5$ no significant difference was observed in either of the two speeds under investigation. The results are plotted in Figure 4.2 as dashed lines.

For the original tank depth ($h/L = 0.6$) the residuary resistance decreased by 2% and 3% for $Fr = 0.37$ and 0.45 when extending b/L from 1.4 to 2.5. These values were identical to those obtained for the infinitely deep tank. The results are summarised in Table 4.2 where the relative difference in residuary resistance compared to an infinitely deep domain (finite vs. infinite depth) is expressed as:$C_R(h/L)$ / $C_R(h/L = \infty) - 1$. The results lead to the conclusion that the water depth needs to be at least $0.7 \times L$ and $0.8 \times L$ for $Fr = 0.37$ and 0.45 to reduce a deviation of residuary resistance by no more than 1% when compared to an infinitely deep domain at the width of $b/L = 1.4$. In shallow water conditions at $h/L = 0.24$, the width of the fluid domain needs to be at least $1.2 \times L$ for the increase in resistance, compared with an infinitely wide domain, to be less than 1% at $Fr = 0.37$. However, as

shown by the low convergence for $Fr = 0.45$ for $h/L = 0.24$ the domain width is required to be at least $15.6 \times L$ for an increase in residuary resistance not to exceed 1%.

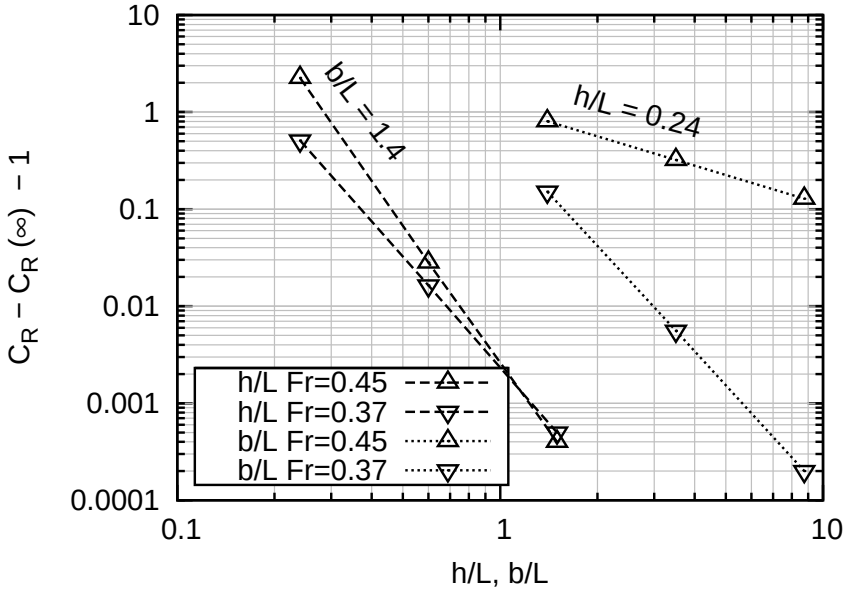

Figure 4.2: Convergence of residuary resistance of a 130 m catamaran at 1:50 model scale with respect to varying tank dimensions for $Fr = 0.37$ and 0.45. The dashed lines show the relative difference of residuary drag at varying tank depth at original tank width ($b/L = 1.4$) compared to an infinitely deep tank. The dotted lines represent the relative difference of residuary drag for different values of tank width in shallow water conditions ($h/L = 0.24$) compared to an infinitely wide tank.

4.3.2 Unsteady Finite Water Effects

The time series of calm water model test data shows a distinct frequency response in unsteady trim and resistance as shown in Figure 4.3 and 4.4. Havelock (1949) derived a closed form solution for the oscillation period of the resistance force of a steadily moving two-dimensional source and Wehausen (1964) for a three-dimensional surface vessel when accelerated from rest. Both concluded that the period of oscillation ($1/f$) of the resistance force can be calculated using:

$$1/f = 8 \times \pi \times V \ / \ g$$

This effect can be explained by waves that are diverging away from the moving vessel which were created by a disturbance, such as due to a change in speed (i.e. model acceleration), wave encounter or trim tab deflection. In deep water, the phase velocity of this wave is always twice the vessel velocity, which results in a following wave situation where the resulting wave encounter period can be estimated by the above formulation. It was shown that the amplitude

Table 4.2: Comparison of drag force at different length and depth Froude numbers of the 130 m catamaran at 1:50 model scale. * Indicates relative difference to $b/L = 3.8$ instead of $b/L = \infty$.

				Relative deviation of C_R:			
				finite vs. infinite width			finite vs. infinite depth
Fr	h/L	Fr_h	b/L :	1.4	3.8	8.75	1.4
	1.50	0.30		-	-	-	0.00
0.37	0.60	0.48		0.02*	-	-	0.02
	0.24	0.76		0.15	0.01	0.00	0.51
	1.50	0.37		-	-	-	0.00
0.45	0.60	0.58		0.03*	-	-	0.03
	0.24	0.92		0.60	0.17	0.05	1.67

of this wave decays at a certain rate (Wehausen, 1964). More recently, Day et al. (2009) investigated the effect of shallow water on the oscillation period and derived a correction for the motion period from model test experiments using a Wigley hull that depends on the depth Froude number (Fr_h) which is applicable for $Fr_h > 0.2$:

$$f \ / \ f_0 = \sum_{0}^{6} \left(a_i \times Fr_h^i \right)$$

with $a_i = (1.273; -4.365; 26.12; -72.29; 95.45; -63.82; 17.64)$. The motion period increases in shallow water with increasing Fr_h and reaches infinity at $Fr_h = 1$, because the model speed and the phase velocity of the wave created by the disturbance are identical. Day et al. (2009) advised that this pitch motion may influence the resistance prediction in a towing tank of finite length, because an integer number of motion cycles need to be resolved to determine a reliable average of the measured resistance force. Furthermore they point out that the decay rate of the oscillations in shallow water is significantly smaller than that in deep water.

The 98 m wave-piercing high-speed catamaran with slender demihulls of 1:22 model scale at water depth of $h/L = 0.35$ was tested in the AMC towing tank at pre-hump speeds as presented in Section 3.3.3. Figure 4.1 and 4.1 show values of trim and resistance for $Fr = 0.31$, 0.39 and 0.44. The data was filtered using a 1 Hz low-pass filter and normalised by the average value. For the pitch motion it can be observed that an increase in velocity leads to an increased motion period ($1/f$ = 6.8, 12.5, 21.4 s for Fr = 0.31, 0.39, 0.44) and reduced motion amplitude. While the pitch amplitude varies up to ± 15% compared to its

average value, for $Fr = 0.44$ it varies up to $\pm$ 40% for $Fr = 0.31$. The resistance fluctuates in phase with the trim, up to $\pm$ 5% for all three speeds under consideration.

Matsubara (2011) reported that distinct pitch motions occur for both the model-scale and full-scale vessel. While the first were recorded using an LVDT (linear variable differential transducer) in towing tank measurements, the latter were obtained from strain gauge measurements of the superstructure of the vessel during sea trials. Figure 4.5 shows the motion frequency normalised by $\sqrt{g \ / \ L}$ of an 112 m wave piercing catamaran at 1:17 and 1:45 model and full scale as well the frequency of a 130 m catamaran at 1:50 model scale and a 98 m catamaran at 1:22 model scale. The water depth varied from $h/L = 0.24 - 1.75$. The motion frequency from CFD results agrees to those obtained by model test experiments. It can be clearly observed that the non-dimensional frequency reduces with increasing length Froude number and decreasing water depth. Also the estimates obtained from Havelock (1949), including shallow water corrections from Day et al. (2009), were plotted in Figure 4.5 and excellent agreement over a wide range of cases can be seen.

However, this oscillation of ship attitude and resistance during the transient resistance prediction process is different from hydrostatically restored ship motion such as the oscillations at zero speed. The oscillations for a steadily moving vessel result from an excitement of the vessel by waves that were created by a disturbance from the vessel due to its acceleration. Additionally, numerical simulations were used to determine the pitch frequency at infinitely deep water conditions. The hull of a 130 m medium-speed catamaran was simulated at $Fr = 0.37$ at three different depths and constant width and the resulting motion frequency measured. It resulted in $T = 14.2$, 6.0 and 4.8 s for $h/L = 0.24$, 0.6 and 1.5. When using generalised Richardson extrapolation a period for infinite depth was estimated to be $^1/_f = 4.6$ s which agrees to the values predicted by Havelock (1949).

It was found that the period for oscillations in model test measurements and CFD simulation results was comparable at identical speeds. This occurs even though in towing tank experiments the model is steadily accelerated from rest, while in the CFD simulations the model is suddenly exposed to a flow at a constant speed. Bucher (2014) showed that applying springs and dampers to the catamaran model in CFD simulations does not affect these oscillations, only reducing the acceleration of the model leads to a decrease in magnitude of the fluctuations of vessel response, not its frequency.

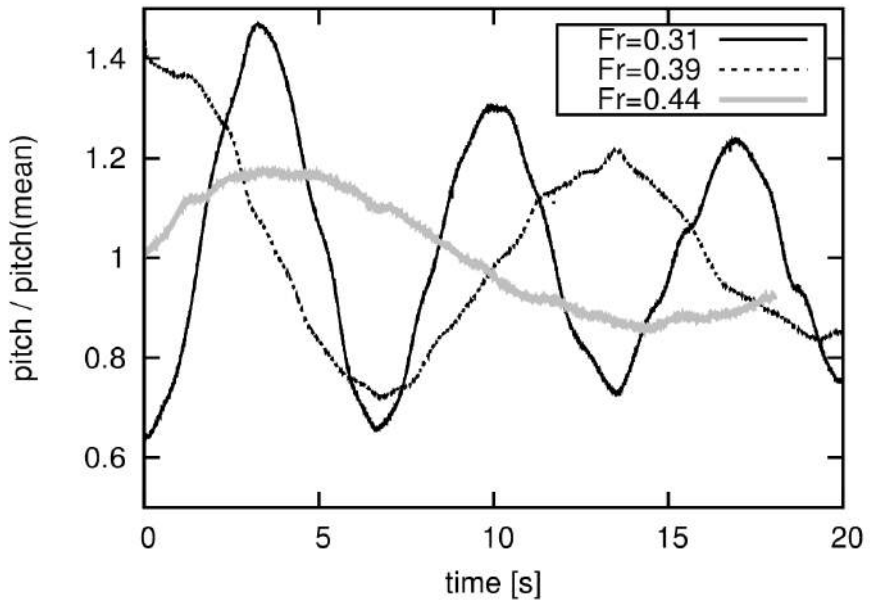

Figure 4.3: Fluctuation of trim for 1:22 model of slender catamaran normalised by its average value for Fr = 0.31, 0.39 and 0.44 during towing tank run.

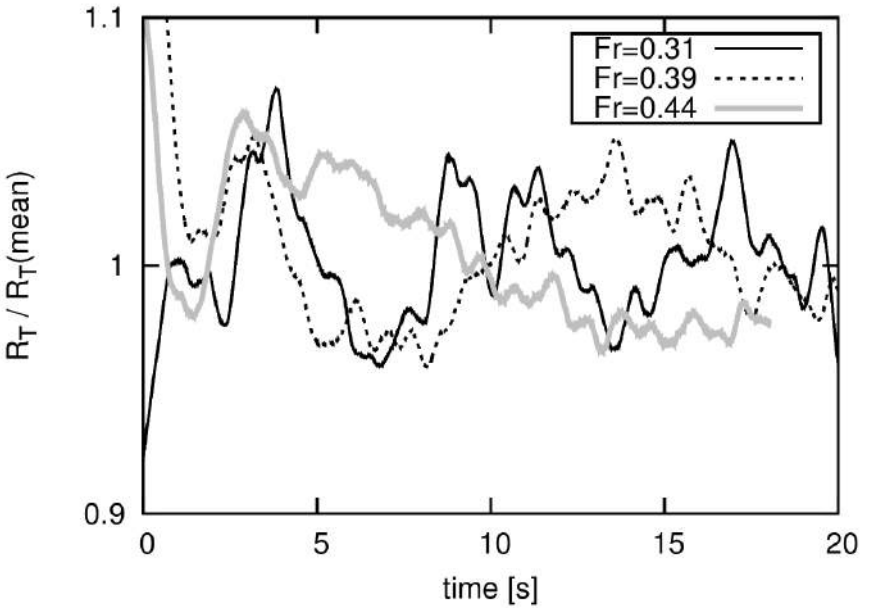

Figure 4.4: Fluctuation of drag force for 1:22 model of slender catamaran normalised by its average value for Fr = 0.31, 0.39 and 0.44 during towing tank run.

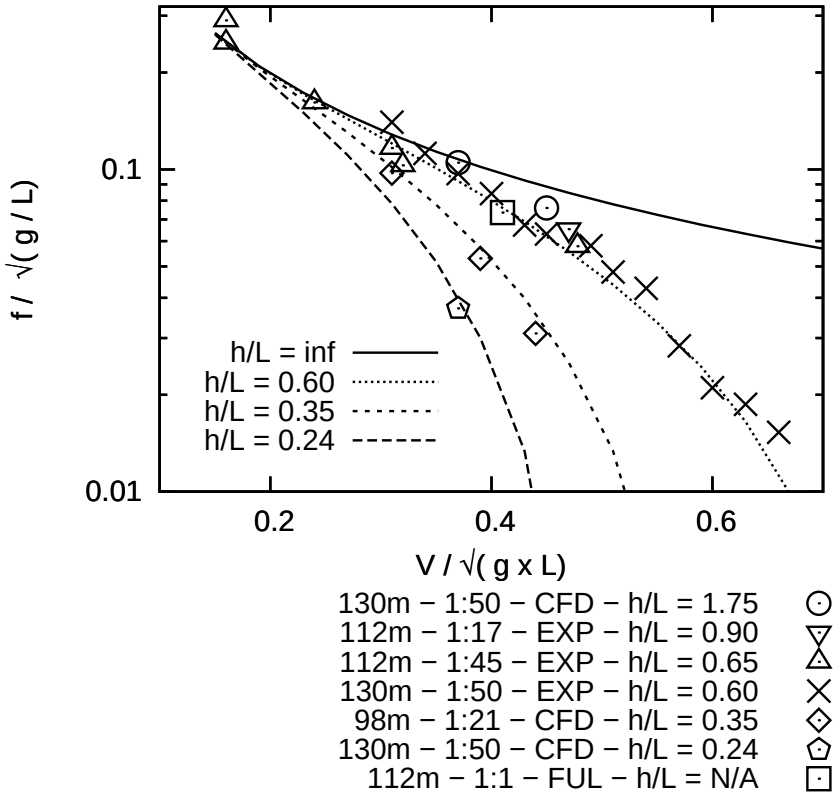

Figure 4.5: Non-dimensional calm water pitch frequency with respect to length Froude number from model test experiments (EXP), numerical simulations (CFD) and full-scale measurements (FUL) for different water depths. The lines present the prediction by Havelock (1949) (solid line) and corrections for shallow water effects as proposed by Day et al. (2009) for $h/L = 0.24$ (long dashed line) $h/L = 0.35$ (normal dashed line) and $h/L = 0.6$ (short dashed line).

4.4 Implications on Full-Scale Resistance

4.4.1 Full-Scale CFD Approach

The methodology to predict the full-scale drag at model-scale dimension proposed in the previous chapter (3) has been extended to take shallow water effects into account. To determine the full-scale resistance of a vessel the fluid domain needs to be modelled in accordance to:

- obtain a near wall modelling that is independent of Reynolds number;
- replicate cross sectional dimensions of towing tank.

The first can be achieved if the first cell height is chosen to be $y_1 = 0.6 \times L \times 10^{-6}$, as shown in Section 3.4, while the latter needs to be fulfilled to account for steady finite water effects such as blockage and increased wave making.

The results from CFD simulations at model scale are compared with model test experiments with corresponding linear dimensions and fluid properties. If the total resistance agrees and the wall shear stress coefficient is close to that of the ITTC model-ship correlation line ($CV = CF$) or established friction lines, the numerical results can be considered as being valid. Therefore, it is assumed that both pressure and viscosity related drag are correctly predicted. Also, it is assumed that the accuracy of the pressure resistance is independent of Reynolds number, hence the same mesh close to the ship hull can be used for full-scale simulations. Full-scale Reynolds numbers are achieved by altering the viscosity of the fluid rather than by scaling linear dimensions. Before conducting the full-scale simulation, steady finite water effects may need to be taken into account and any of the following cases can be considered:

- Model-scale testing and full-scale operation are in finite waters, with relative depth and width being identical at both scales.
- Finite water is present for verification at model scale, but the water can be considered as being infinite for the full-scale ship
- Unrestricted water applies for the verification at model scale, but the full-scale ship operates in finite water.
- Model and full-scale vessel sail in finite waters, but depth and width are not in correlation between scales.

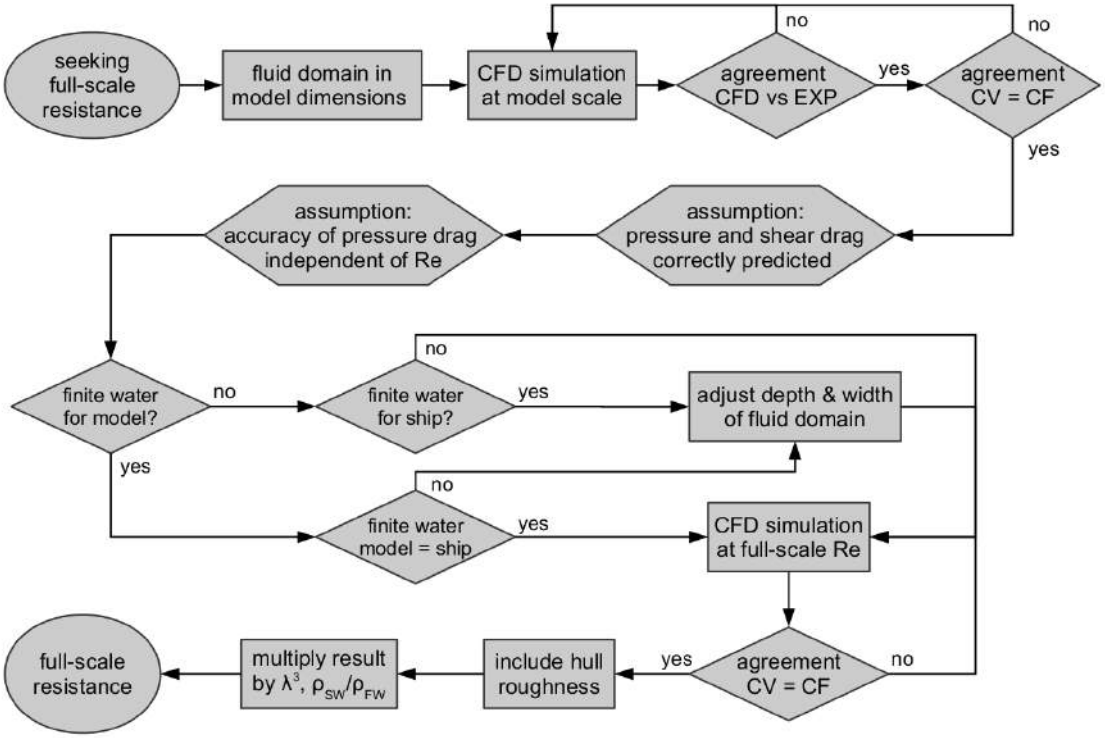

Figure 4.6: Flowchart to obtain full-scale resistance considering shallow water effects using a novel CFD approach in conjunction with model test experiments for verification.

If the first case applies, the identical mesh can be used for model and full-scale simulations, however, if any of the latter three cases apply the absolute dimensions of the computational domain need to be adjusted accordingly to assure that the influence of finite water on the full-scale results is physically correct.

The full-scale simulation can be run for a smooth hull and considered as being accurate when an acceptable agreement of the shear force coefficient with a model-ship correlation line or friction line is achieved ($CV = CF$). If desired, the surface roughness can be taken into account in terms of equivalent sand grain roughness. To finally obtain dimensional full-scale resistance the result needs to be multiplied by scale factor to the power of three and the relative difference of fluid density between model and full scale (ρ_{SW} / ρ_{FW}). The approach is summarised in Figure 4.6.

4.4.2 Case Study of a 98 m Catamaran

In this section the numerically determined full-scale drag of the 98 m catamaran is compared to results from power measurements from sea trials (Griggs and Woo, 2005) and extrapolated model test data. The full-scale resistance from the shaft power measurements was derived

using thrust curves of the waterjet propulsors, neglecting the effects of wake fraction and thrust deduction as shown in Chapter 3. The model test data was extrapolated using ITTC guidelines including shallow water corrections, of Schuster (1956). The validation was performed at a speed of 18 knots which corresponds to a length Froude number of $Fr = 0.31$ and for $h/L = 0.12 - 0.17$ to a depth Froude number of $Fr_h = 0.79 - 0.92$.

Extrapolation of Model Test Data

The model test data of the 98 m catamaran presented in Section 3.3.3 was extrapolated using ITTC procedures (7.5-02-02-01) with $(1 + k) = 1.0$ and the correction of Schuster (1956) applied to account for shallow water effects. The approach was utilised first to obtain data applicable in infinite water from resistance tests that were conducted in finite water $(h/L = 0.35, b/L = 1.4)$. Secondly the resistance for the vessel in infinitely wide, but shallow water $(h/L = 0.12 - 0.17, b/L = \infty)$ was estimated using the approach by Schuster (1956) where the ship speed with respect to the resting water is corrected, which is defined as follows:

$$dv/V = m \ / \ (1 - m - Fr_h^2) + (1 - R_F/R_T) \times 2/3 \times Fr_h^{10} \tag{4.1}$$

with $m = A_X/(b \times h)$ where m is the blockage ratio with A_X being the cross sectional area of the hull. The term $(1 - R_F/R_T)$ predicts the portion of wave-making to which the correction addresses.

Furthermore, an empirically determined roughness and correlation allowance as proposed by ITTC (7.5-02-02-01) was added with 200 μm of equivalent sand grain roughness. Wind drag, based on measurements by Oura and Ikeda (2008), was utilised to make the data comparable to estimates from sea trial measurements.

Comparison of Results

The full-scale resistance of a 98 m high-speed catamaran in shallow water was investigated at $Fr = 0.31$. The sea trials were run at a depth ranging between $0.12 < h/L < 0.17$. The predictions were made at the two extreme values of depth. While a finite depth was modelled in CFD, the correction of Schuster (1956) was applied to the model test data before corrections for shallow water and blockage (to be applicable for deep water) using the same approach.

Relative differences between predictions from CFD and model tests compared to sea trial data were made by $R_{T(CFD)}/R_{T(seatrial)} - 1$, with results presented in Figure 4.7 Table 4.3.

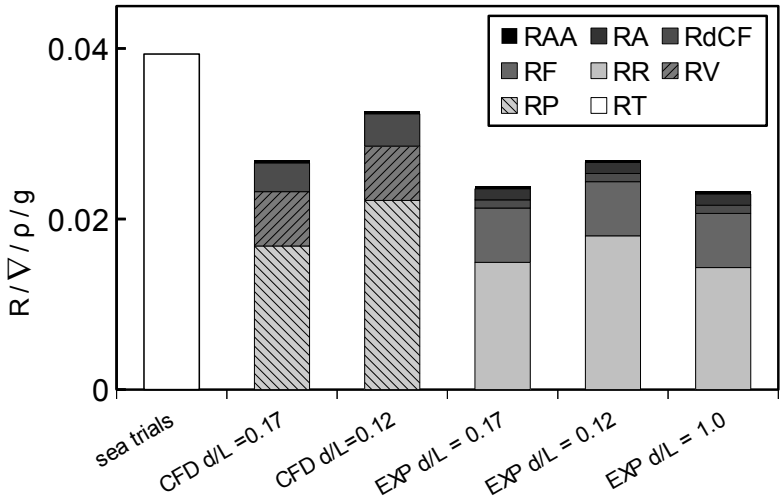

Figure 4.7: Dimensionless drag at Fr = 0.31 obtained from CFD and model test extrapolation for two depths which were stated as extreme values for the sea trial measurements. Drag in deep water was added for comparison.

Table 4.3: Relative deviation of predicted full-scale drag for 98 m catamaran using CFD and extrapolated model test data corrected for shallow water by approach of Schuster (1956) without form factor with respect to drag estimated from full-scale powering measurements.

		Relative deviation of R_T: CFD and model test extrapolations vs. sea trials				
speed		CFD		model test		
[kn]	h/L :	0.17	0.12	0.17	0.12	1.0
18.2		-0.32	-0.17	-0.4	-0.33	-0.42

The drag forces from the CFD predictions were 17% and 32% below the values estimated from the full-scale sea trials, with the extrapolated data being 33% and 40% below the results from sea trials. If no shallow water correction during the extrapolation was applied the deviation reached up to 42%. These differences are significantly larger than those obtained in deep water conditions presented in Section 3.5.4.

Possible reasons for these discrepancies between the results from CFD and sea trials may be again addressed to the possibly invalid assumption of having a thrust drag equilibrium, unsteady effects in finite water, and thus insufficiently long data histories for the current conditions. Based on the successful verification of shallow water drag force, the candidate assumes a comparable accuracy for the full-scale drag when predicted by CFD. Since for $Fr = 0.31$ the deviation in drag increased from 10% in deep water (see Section 3.5.4) to 17%

and 32% in shallow water, the origin may be concluded to result from changing flow into the waterjet units and hence an increased thrust deduction or reduced propulsive efficiency.

Furthermore, the presented results lead to the conclusion that the model test extrapolation, including shallow water corrections, significantly underestimates the full-scale drag, which implies that the approach by Schuster is not necessarily valid to accurately predict shallow water drag of a vessel from data that was recorded in deep water towing tank experiments.

4.4.3 Case Study of the 130 m Catamaran

The full-scale resistance for the 130 m catamaran when considered a smooth hull was predicted in shallow water and compared to extrapolated model test data that was recorded in shallow ($h/L = 0.24$) and deep water condition ($h/L = 0.6$) and extrapolated according to ITTC guidelines (7.5-02-02-01). The deep water data was extrapolated with and without considering shallow water corrections proposed by Schuster (1956).

$$R_R = C_R \times \rho/2 \times (V \times (1 + dv/V))^2 \times S_W \tag{4.2}$$

where $dv/V = 2/3 \times Fr_h^{10}$ as $m = 0$ for an infinitely wide fluid domain. However the numerical simulation revealed that the flow velocity around the vessel can increase up to 6% for $Fr_h = 0.92$ at $h/L = 0.24$ in a sufficiently wide tank of $b/L = 8.75$ where no interaction with the side wall was observed. The model-scale experiments were conducted at a tank width of $b/L = 1.4$, however, due to the findings in Section 4.3.1 the full-scale simulation was conducted at $b/L = 3.8$ and 8.75 for Froude numbers of $Fr = 0.37$ and 0.45.

Comparison of Results for the 130 m Catamaran

Figure 4.8 shows the results for a smooth hull based on numerical simulations and extrapolated model test data from deep and shallow water runs. The experimental data for both speeds was obtained at a tank width of $b/L = 1.4$, while in the numerical simulations the tank width was $b/L = 3.5$ for $Fr = 0.37$ and $b/L = 8.75$ for $Fr = 0.45$ based on the results from the study in section 4.3.1 on finite width effects to minimise their impact. The deviation between the resistance prediction by CFD and shallow water experiments is 11% and -3.5% at $Fr = 0.37$ and 0.45 as summarised in Table 4.4. When considering the resistance components from the data obtained at $h/L = 0.24$ (see Table 4.5), it can be seen that the pressure related drag (RP, RR) is 5% and 12% lower in CFD results while the frictional part (RF, RV) is higher by 35% and 21% in numerical predictions for the lower and higher speeds respectively. In deep water the deviation in pressure related drag was similar, but the

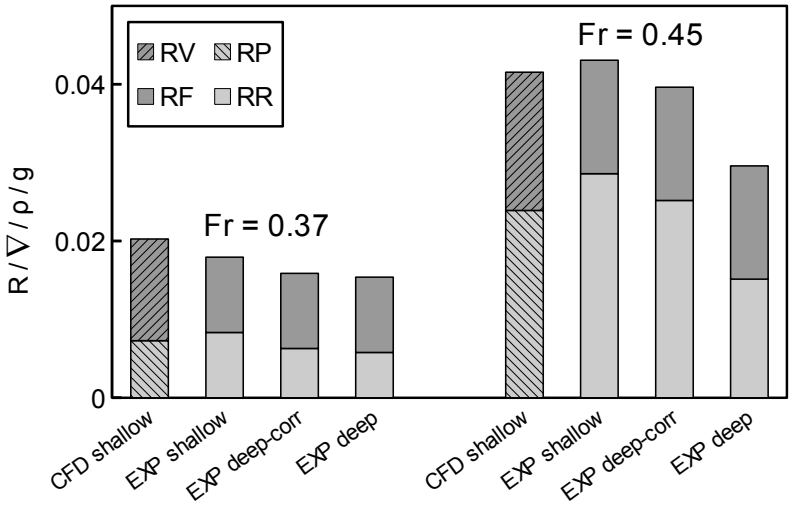

Figure 4.8: Full scale drag predictions for 130 m catamaran from model test experiments and CFD of bare hull with no superstructure of 130 m medium-speed catamaran at Fr = 0.37 and 0.45 in shallow water. Model test results were obtained at shallow water (EXP-shallow) and deep waterwith (EXP-deep-(S)) and without (EXP-deep) correction for shallow water by approach of Schuster (S).

frictional was different only by 1% and -5% when compared to the results of simulations and extrapolated experiments without using a form factor (compare to Section 3.5.4).

The extrapolated resistance data from deep water runs under estimates the numerically predicted drag by up 38% for $Fr = 0.45$ when no shallow water correction is applied.

The CFD-predicted resistance showed larger deviations when compared to extrapolated model test data than it was achieved in deep water conditions as presented in Section 3.5.4. Numerically predicted residuary or pressure drag is lower than that experimentally determined, while the opposite is true for the viscous or frictional resistance part. Since the deviation in drag between model-scale results and CFD simulations is below 3% it can be assumed that CFD is capable of accurately resolving the flow around a vessel in shallow water. The differences in total drag and especially of the frictional component when comparing the results of CFD and extrapolated model tests applicable to the full scale ship may lead to the conclusion that ITTC recommended procedures for model test extrapolation are not readily applicable for shallow water conditions.

4.4.4 Practical Implications

In Section 4.2.2 it was shown that the drag force in towing tank with restricted water can be predicted within 6% for the heavy displacement case and even within 3% for light dis-

Table 4.4: Relative differences of extrapolated model scale results compared to CFD predictions for full-scale resistance of 130 m medium-speed catamaran in shallow water at $h/L = 0.24$. Positive values indicate higher prediction by CFD, model test data has been recorded in shallow $h/L = 0.24$ and deep water $h/L = 0.60$ including the latter corrected by the approach of Schuster (1956).

			Relative deviation of R_T: CFD vs. model test extrapol.		
		depth correction:	none	Schuster	none
Fr	Fr_h	h/L :	0.24	0.6	
0.37	0.58		0.11	0.22	0.24
0.45	0.92		-0.04	-0.05	0.29

Table 4.5: Relative differences of extrapolated model scale results compared to CFD predictions for full-scale resistance of 130 m medium-speed catamaran in shallow water at $h/L = 0.24$. Positive values indicate higher prediction by CFD, model test data has been recorded in shallow $h/L = 0.24$ and deep water $h/L = 0.60$ including the latter corrected by approach of Schuster (1956).

	Relative deviation of resistance components CFD vs. model test extrapol.		
Fr	RT/RT-1	RP/RR-1	RV/RF-1
0.37	0.11	-0.05	0.35
0.45	-0.04	-0.12	0.21

placement case when compared to measurements. Furthermore the CFD approach has been capable of quantifying the influence of limited depth and width on the total drag force compared to an infinitely deep and wide tank (Section 4.3.1). Especially for medium-speed catamarans with high slenderness ratios the effect of blockage is considered as being small as the midship sectional area is small with respect to the towing tank cross section when compared to conventional craft of comparable displacement. Hence the CFD approach can be used to design towing tank experiments so that the influence of the tank bottom or walls is below a specified threshold when a maximum model scale factor is applied. Also the unsteady effects such as the increase in oscillation period of the model response can be considered in the simulations, which allows to estimate if a sufficient number of oscillation cycles will be recorded and thus a converging solution can be achieved. This emphasises the applicability of CFD as a model-ship correlation tool as proposed Chapter 3.

4.5 Conclusions

This study used numerical simulations, model test data and full-scale measurements to investigate steady and unsteady finite water effects. The numerical model was verified using towing test experiments, and CFD underestimated drag at the light displacement condition by as little as 3% for Froude numbers of $Fr = 0.37$ and 0.45 and under estimated the drag by less than 6% at the combination of heavy displacement and higher speed.

Firstly, steady finite water no matter if restricted in depth or width was found to increase the calm water resistance force, an effect that can be attributed to blockage and increased wave making, especially in limited water depth. For a fixed domain or towing tank width of $b/L = 1.4$ a depth of $h/L = 0.7$ and 0.8 is required at Froude numbers of $Fr = 0.37$ and 0.45 for the residuary resistance to be less than 1% above the value for an infinitely deep fluid domain. For shallow water depths such as $h/L = 0.24$ the domain width was found to be at least $b/L = 1.2$ for speeds of $Fr = 0.37$ to not exceed the residuary resistance for an infinitely wide domain by more than 1%, For Froude numbers of $Fr = 0.45$ the required widths increases to $b/L = 15.6$.

Secondly, unsteady finite water effects mainly related to a reduced water depth were found to be of very high importance for large medium-speed vessels. These effects lead to an increase in the oscillation period in resistance and measured heave and trim that occur at periods in excess of the available runtime in towing tank experiments. Therefore, the averaging of the transient data record may lead to inaccurate results. The dimensionless period of these oscillations has been shown to have agreement between numerical predictions, towing tank

experiments and full-scale sea trial measurements. The non-dimensional frequency solely depends on vessel length and depth Froude number.

When comparing full-scale drag for a medium-speed catamaran in limited water depth ($h/L = 0.12 - 0.17$) predictions by CFD to results from sea trials and extrapolated deep water model test data, it was found that CFD estimates are 15% larger than extrapolated model test data, but up to 32% smaller when compared to powering data from sea trials. It has been concluded that shallow water corrections for model test data does not deliver reliable results and that the thrust drag equilibrium is not applicable, thus the propulsor size needs to be larger than the resistance value would suggest.

Full-scale resistance prediction using a novel CFD-approach for 130 m catamaran at Froude number of $Fr = 0.37$ delivered a 13% higher drag when compared to extrapolated model test data recorded at the corresponding water depth, but at the Froude number of $Fr = 0.45$ the CFD prediction was 4% lower. Pressure related forces from CFD predictions for a sufficiently wide fluid domain were up to 12% lower and frictional forces up to 35% higher when compared to extrapolated model-scale data.

This emphasises the requirement for reliable full-scale drag prediction to estimate the power requirements, especially if the ship is operated in shallow water. It has been shown that deep water towing tank tests results corrected for shallow water effects using ITTC recommended procedures underestimated the drag force when compared to CFD predictions. Also, extrapolating shallow water data using approaches mentioned for deep water may lead to an underestimate of the total drag force at full scale.

Finally, it has been suggested that the CFD approach can be utilised to evaluate model sizes for towing tank testing to keep the influence of steady and unsteady finite water effects on the drag force to an agreed minimum.

4.5.1 Recommendations for Future Work

Future work may focus on further validation approaches. These could include modelling the waterjet unit to enhance the methodological correlation when comparing results to full-scale sea trial data or to exactly replicate the acceleration of the towing tank carriage and limited tank length to avoid using time averaged values for validation at model-scale which may lead to inaccurate results as the average may have been determined from too few oscillation cycle of the ship model response.

4.6 Where to next?

This chapter showed that whilst shallow and restricted water complicates the prediction of resistance due to steady and unsteady effects, it is possible to use CFD to determine resistance predictions with acceptable agreement between CFD results and model test data. The final step in investigating the capabilities of this CFD-based approach to resolve the flow around catamarans is to assess its ability to accurately model the ventilation process at the transom, this is the focus of the next chapter.

Chapter 5

Wave-piercing Catamaran Transom Stern Ventilation Process

This Chapter has been submitted for publication and is under peer review. The current citation for the research article is:

M. Haase, J. Binns, G. Thomas, and N. Bose (2015f). "Wave-piercing Catamaran Transom Stern Ventilation Process". In: *Ship Technology Research / Schiffstechnik* in press

---

The current version of this chapter has been modified compared to the submitted version to guide the reader more conveniently through this thesis.

Abstract

An investigation into the transom ventilation of hull forms with a deep transom, such as a wave-piercing catamaran, is reported. Medium-speed catamarans are likely to operate at speeds where the transom is partially or fully ventilated. It is important to understand the flow characteristics in the wake of the transom stern to ensure that numerical tools, used for resistance prediction, are accurately resolving the complex flow phenomena. Unsteady RANS (Reynolds-Averaged Navier Stokes) simulations were used to simulate the flow around a 98 m catamaran, at both model and full scale, and the first compared to model test results for a 1:22 scale model. A non-shedding squashed horseshoe vortex was found to build up in the stagnant zone past the vessel, with the transom running dry at transom draft Froude numbers of $Fr_T = 2.5$ in model test experiments and of $Fr_T = 2.4$ in CFD simulations at the same scale. For full-scale Reynolds numbers the full ventilation occurred at transom draft Froude numbers of $Fr_T = 2.2$. Furthermore, it is shown that unsteady RANS simulations are capable of qualitatively correctly predicting the flow features in the wake of the vessel and that the state of transom ventilation can be reliably predicted, thus the flow features during the quasi-steady ventilation process is visualised.

5.1 Introduction

Large medium-speed catamarans, when compared to high-speed catamarans, will be larger in length and displacement, but operating at lower speeds; thus requiring different design principles. Transom sterns are popular features for fast ships as it reduces the resistance at Froude numbers of $Fr > 0.5$, but can increase the drag for speeds below as shown by O'Dea et al. (1981) and Hadler et al. (2009) and later in Section 6.3.2. However, a transom stern simplifies the vessel's construction (Schneekluth and Bertram, 1998), and it is convenient for accommodating waterjet propulsors (Doctors et al., 2007; Davidson et al., 2011b). Whilst a deep transom is a popular feature for high-speed catamarans, it may not be beneficial for this new class of vessels as they operate at lower Froude numbers, and therefore it is necessary that its effect on the hull is accurately replicated in resistance prediction methods.

In an earlier study (Haase et al., 2012a) it was shown that RANS methods are capable of predicting calm water resistance of medium-speed catamarans for both dry and wet transoms, but also that deviations at low Froude numbers occur when compared to measured data. Build-up of a rooster tail at high speeds and a complex recirculation at low speeds were found, but the accurate prediction of the transition process from fully wet to a fully dry transom was not considered.

5.1.1 Transom Stern Flow Predictions

The flow regime of a surface vessel is usually expressed in terms of length Froude number ($Fr = V \ / \ \sqrt{g \times L}$), V is the ship's velocity, g the gravitational constant and L the ship's waterline length. To characterise the flow past a transom it is appropriate to express it with respect to transom draft Froude number ($Fr_T = V \ / \ \sqrt{g \times T_T}$) where T_T is the draft of the transom with the vessel stationary. Studies by various researchers (Robards and Doctors, 2003; Maki et al., 2006) have shown that the transom reaches a dry state at $Fr_T \approx 2.5$. This value may depend on the stern shape of the hull, its wave-making characteristics, the Reynolds number and dynamic sinkage and trim.

The accurate prediction of the flow past a transom stern of a surface vessel has been of interest for many years. This is primarily due to the significance of the transom flow patterns on the estimate of the resistance force by including the influence on the wave-making, such as studied by Doctors et al. (2007). In addition, the wake generates a highly unsteady flow field, including entrained air, which is an issue for defence vessels if detection is to be avoided. Hence the flow characteristics need to be modelled to a very fine extent (Hendrickson

et al., 2013). The following paragraphs summarise the main achievements in modelling and predicting transom flows.

Experimental Approaches

Transom ventilation was experimentally studied for semi-palning catamarans by Oving (1985) who formulated that the dry state will occur at $Fr_T = 1.95$ with corrections for $B_T/T_T \leq 2.5$. Hadler et al. (2007) presented model test observations of his own experiments, those of Sireli et al. (2000) who utilised NPL hulls, and those of Kiss and Compton (1989) who used combatant hulls. Based on these studies a critical transom depth Froude number at which the transom runs dry was derived as a function of B_T/T_T. For $1 < B_T/T_T < 3.5$ they predicted a dry transom between $2 < Fr_T < 2.5$, where increasing B_T/T_T values led to higher values of critical transom draft Froude number.

Robards and Doctors (2003) and Doctors et al. (2007) used the Baby series, hulls with constant rectangular cross sections and parabolic waterlines at the bow, to derive an empirical formulation to express the ventilation with respect to transom draft Froude number, B_T/T_T, and transom draft Reynolds number ($Re_T = \sqrt{g \times T_T^3/\nu}$. They found that the influence of the transom draft Reynolds number on the ventilation process at the model scale range was small. Alternative coefficients for the empirical formulation were derived for a destroyer hull form by Maki (2005), who also studied the free surface flow past a backward facing step to estimate the flow characteristics of an infinitely wide transom (Maki et al., 2006). Four flow regimes were identified and are presented in Figure 5.1. Firstly, a stagnant area behind the transom that connects through a shear layer to the passing flow (regime A); with transom draft Froude number exceeding unity, a distinctive vortex shedding was observed (regime B); reaching a critical transom Froude number where the transom goes dry and a breaking roller forms behind the separation point characterises the next regime (regime C); with further increasing transom Froude number this breaking roller moves further backwards and finally disappears (regime D). In the same study the process of ventilation was in agreement with the empirical formulation postulated by Doctors et al. (2007).

Computational Approaches

Fluid flow solvers that resolve the flow domain by subdividing it into small control volumes and take viscous effects into account are potentially capable of correctly simulating flows past transom sterns. Lin and Percival (2001) computed the flow around two bare hull transom stern combatant vessels using a steady RANS solver (Reynolds-Averaged Navier-Stokes) and

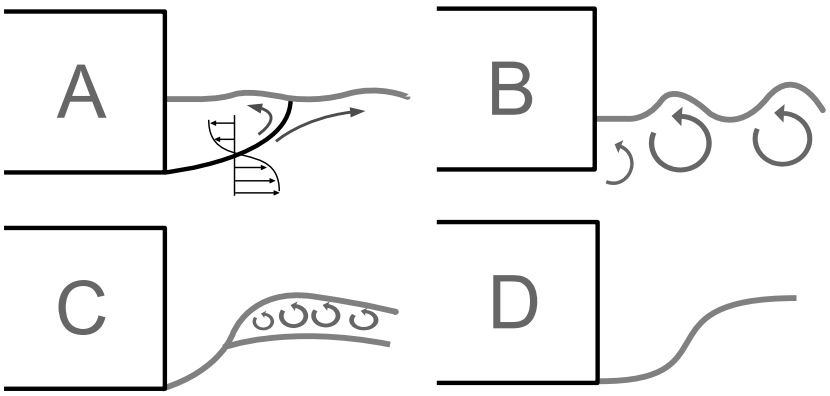

Figure 5.1: Transom flow regimes as identified by Maki (2005) A: $Fr_T < 1$ resulting in a stagnant recirculating flow area that is separated by a shear layer. B: $1 < Fr_T < Fr_T(dry)$ produces an unsteady von-Karman street with large surface fluctuations. C: $Fr_T > Fr_T(dry)$ leads to a dry transom and a breaking roller building up behind separation point. D: $Fr_T >> Fr_T(dry)$ so that the breaking roller past the separation disappears.

implemented a kinematic boundary condition on the free surface to take wave elevations into account. The ability of the method to predict whether the transom was wet, dry or partially wet was reported.

Wilson et al. (2006) used an unsteady RANS solver to compute the flow around the bare hull of the R/V Athena and found periodic vortex shedding at the transom edge for partially wetted states. Eslamdoost et al. (2015) used unsteady RANS and experiments to study the influence transom clearance on the drag force for a hard chine planing hull and identified that entering the full ventilation state coincides with the peak in resistance coefficient curve. Maki (2005) computed the flow past a free surface backward facing step using a 2D unsteady RANS solver utilising a level set approach to capture the free surface effects. Starke et al. (2007) used a 2D steady-state surface-fitting RANS approach to simulate the free surface flow past a backward facing step for Reynolds numbers correlating to both model and full scale vessels. Comparing their computed surface elevation with experimental data from Maki (2005) they obtained accurate solutions for partially and fully ventilated transoms. Scale effects were found such that full ventilation was predicted to occur at lower transom draft Froude number ($Fr_T = 2.0$) for full scale Reynolds numbers, compared to model scale Reynolds number (where $Fr_T = 2.5$). Wyatt et al. (2008) compared two codes, one being a RANS/DES (detached eddy simulation) code using a single phase, level-set method, the other a Cartesian Euler code. Average breaking wave height and corresponding RMS values (root-mean-square) of its fluctuation as well as the frequency domain in the flow past the transom

of R/V Athena were simulated at full scale and compared to full-scale measurements and good overall agreement was reported. The von-Karman-type vortex shedding for a wetted transom was shown using the RANS/DES solver for model and full-scale simulations of the fully appended vessel. Bhushan et al. (2012) investigated vortex structures and instabilities past the wetted transom of the fully appended R/V Athena in full scale and model scale. Using the solvers utilised in the above study, RANS was able to resolve coherent vortex shedding while the DES simulation could resolve much more detailed flow structures. The RANS/DES solver was capable of explaining the wake unsteadiness with the von-Karman-type vortex shedding. Lately, researchers have concentrated on the air entrainment in the wake of a transom stern ship using implicit LES (large eddy simulation) simulations, such as Hendrickson et al. (2013) who investigated the wake past a dry transom. The above studies indicate that a considerable amount of research has been conducted during the last decade to investigate steady and unsteady effects of the flow around a transom stern, However, it was mostly studied on combatant or planing craft hull forms that have a relatively high B_T/T_T ratio, which exceeds that of a typical wave-piercing catamans and hence the three-dimensional structure of the flow in the stagnant zone past a partially ventilated transom is not understood,

In this study, the flow characteristics past a partially ventilated transom were studied numerically and experimentally to quantify the state of transom ventilation at different speeds. A scale model of a 98 m wave-piercing catamaran (Figure 3.2) was used at low to medium speeds of $0.2 < Fr < 0.4$. Compared to previously mentioned studies the current hull has a relatively low B_T/T_T ratio of 1.3. This research aims to assess the capability of unsteady RANS simulations to correctly predict the flow features occurring inside the zone of stagnant flow behind a transom stern. In particular, whether a standard mesh resolution is sufficient or if special attention to local mesh refinements is required in this flow region. Furthermore, there is the desire to quantify differences in transom ventilation between model and full-scale Reynolds numbers. Numerical simulations were validated experimentally using quantitative and qualitative measures including the level of transom ventilation and visualised flow features.

5.2 Methodology

The investigation on the flow past a partially ventilated transom stern was undertaken on a single demihull of a 1:22 scale model of a 98 m wave-piercing catamaran at a 1,500 tonnes displacement at level trim. The transom features a trim tab that was deflected to 5 degrees.

The demihull interaction was taken into account by evaluating the model performance in close proximity to a wall at a distance equal to half the demihull separation. While this is a common approach in numerical simulations due to the symmetry of the flow with respect to the centre plane of the vessel, it is only occasionally used in physical model testing such as by Rovere (1997) and Zürcher et al. (2013).

5.2.1 Numerical Set-up

In this study an unsteady RANS solver *interDyMFoam* from the OpenFOAM toolbox 2.3 utilising a volume of fluid method (VOF) was used to simulate the flow around the vessel. The solver is capable of resolving viscous free-surface flows and the changing attitude of the vessel. $k-\omega-SST$ turbulence model and standard wall functions were applied to model the flow in close proximity to the hull, wall shear stress was computed with OpenFOAM version 2.0. The state of partial transom ventilation was computed from the ratio of wetted transom area (A_{TW}) over total transom area A_T. As expressed by:

$$A_{TW} = \sum(-n_{xi} \times \alpha_i \times A_i) \; \forall \; x \leq x_{transom} \tag{5.1}$$

and

$$A_T = \sum(-n_{xi} \times A_i) \; \forall \; x \leq x_{transom} \; \wedge \; z \leq 0 \tag{5.2}$$

α characterises the volume fraction where unity denotes full of water and zero denotes devoid of water, n_x the longitudinal component of the normal vector and A_i the area of the cell face attached to the hull. Hence the transom ventilation is expressed as:

$$\eta_{dry} = 1 - A_{TW}/A_T \tag{5.3}$$

Positive x is pointing forward and positive z upward with the origin at the transom at still water level. The domain consisted of a block-structured background mesh and an unstructured hedrahedral mesh in close proximity to the hull and for free surface refinement. The mesh in the current study consisted of 900k cells which was found to deliver an acceptable drag force estimate, not exceeding 5% difference when compared to model test experiments for $Fr \geq 0.40$ (see Section 3.3.1) when the transom is clearly dry and no special mesh refinement in the transom area was made. Figure 5.2 shows the structure of the cells at the transom. The cells were stretched by a factor of 4 in the longitudinal direction to account for the governing flow direction around the hull, which results in relatively few cells in the longitudinal direction behind the vessel.

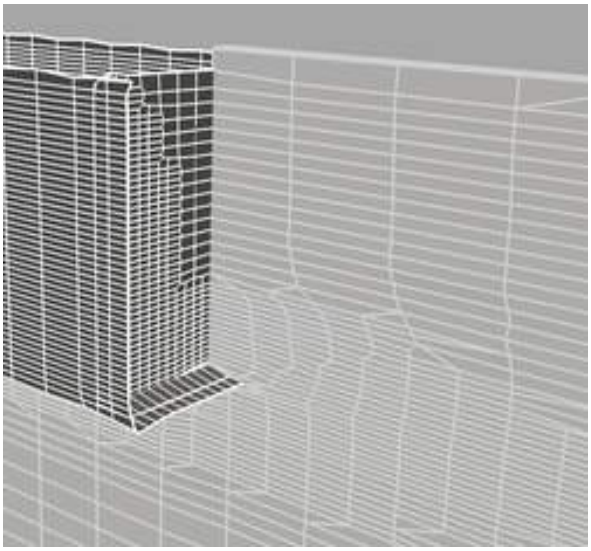

Figure 5.2: Cell structure at the transom stern utilised in this study.

5.2.2 Experimental Set-up

The experiments were carried out in the towing tank of the Australian Maritime College (AMC) at the University of Tasmania having the dimensions of $l \times b \times h = 100$ m $\times$ 3.55 m $\times$ 1.50 m, using a single demihull carbon fibre scale model of a 98 m wave-piercing catamaran of 4.3 m length, which was free to heave and trim. The demihull was employed at half demihull separation distance from the tank wall to take demihull interaction effects into account. The transom immersion was measured visually using rulers with 5 mm increments attached to the transom stern as can be seen in Figure 5.4. To determine the characteristic structures of the flow in the stagnant area behind the transom, polyester stream traces (audio tapes) were attached to the inside of the trim tab and the side hull extensions. At total of 16 polyester tracers were utilised each with a thickness 0.1 mm, width 10 mm, and a length of 240 mm. The observations were made using three commercially available water proof video cameras such as from *GoPro* and *Contour*, which are highlighted in Figure 5.3. One camera was mounted above the stern to monitor the flow past the stern from above the water surface. Another was mounted under water to record the level of ventilation and the flow structures. Finally, the third camera was set up below the transom pointing upwards to videotape the structure of the flow recirculation in the horizontal plane. In addition, the drag force was measured.

The transom ventilation was determined as the ratio of the water level at the aft of the port side wall of the port demihull and the water level at the transom. In contrast to the numerical model, the origin of the vertical axis was ship fixed and originates at the trailing

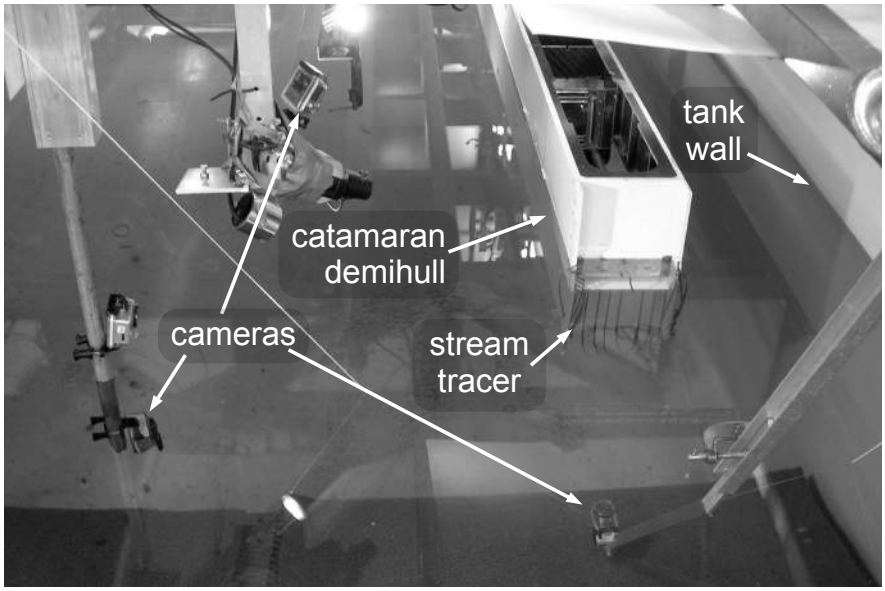

Figure 5.3: Experimental set up in the AMC towing tank. A single catamaran demihull is towed in close proximity to the tank wall. Also the positions of the cameras used and the stream tracers are highlighted.

edge of the stern tab, positive pointing up. Thus the ventilation state was determined as:

$$\eta_{dry} = 1 - z_{side\ wall}/z_{transom} \tag{5.4}$$

5.2.3 Empirical Prediction Method

Doctors et al. (2007) performed a series of model tests on generic hull forms using the so-called Baby series to derive a regression model for predicting the state of transom ventilation as a function of transom Froude number based on transom draft at rest, with and without taking the transom breadth over transom depth ratio (B_T/T_T) into account. Furthermore they included the transom Reynolds number, though this did not influence the results at the model of the size under investigation. Transom ventilation was determined as follows:

$$\eta_{dry} = C_1 \times Fr_T^{C_2} \times (B_T/T_T)^{C_3} \tag{5.5}$$

with values for C_i being $C_i = (0.08057, 2.831, 0)$ for the infinitely wide transom (2D) and $Ci = (0.07340, 2.8356, 0.1247)$ when taking B_T/T_T into account (3D) for $1 < B_T/T_T < 4$.

5.3 Validation of Transom Flow

5.3.1 Physical Model Tests

The model was tested for length Froude numbers of 0.20 to 0.40 in 0.02 increments. The water level at the transom was measured at each run. Figure 5.4 shows the transom at three different speeds: Fr = 0.24, 0.30 and 0.36, corresponding to transom draft Froude numbers of Fr_T = 1.56, 1.97 and 2.38. The state of ventilation, η_{dry}, is 0.24, 0.55 and 0.95 respectively. A complex small-scale flow structure can be observed for Fr = 0.24, which transits towards a rooster tail at Fr = 0.30 where the white portions in the wake can be addressed to wave-breaking. At Fr = 0.36, even though the transom is not fully dry a rooster tail builds up due to a combination of flow uprising from underneath the hull and from flow around the vertical walls pointing towards the centre plane of the wake. Clearly, the wave of the rooster tail breaks to both sides and also sheds portions of water towards the transom. Finally, the transom reaches the dry state at Fr = 0.38 corresponding to Fr_T = 2.50. The dry state for all conditions under consideration can be seen in Figure 5.5, where the error bars represent the smallest increment on the ruler.

5.3.2 Nummerical Prediction at Model Scale

The experiments were replicated at an identical displacement and speeds. Such seen in the physical testing, in the numerical simulations the transom ventilation increased with increasing speed, but reached the dry state ($\eta_{dry} > 0.99$) at Fr_T = 2.42, which corresponds to an under-prediction of dry state transom draft Froude number of 3%. When comparing this result to Eslamdoost et al. (2015), where the RANS-based simulation predicted the dry state at a 5% lower length Froude number when referred to model test experiments, therefore, the result can be considered as being acceptably accurate.

Figure 5.5 shows the transom ventilation state for increasing transom draft Froude numbers for the speeds under consideration predicted by numerical simulation and empirical expressions, and measured in model test experiments. For the CFD predictions no error was specified, even though it was observed that the transom ventilation fluctuated over time, the fluctuation was found to be ± 1% for Fr_T = 1.78 where the transom ventilation was 0.44.

For transom draft Froude numbers exceeding 1.6, an agreement between numerical predictions and measurements was within the specified error of the experimental results, whereas for lower speeds the numerical simulation predicts a $10 - -12\%$ higher water level at the transom.

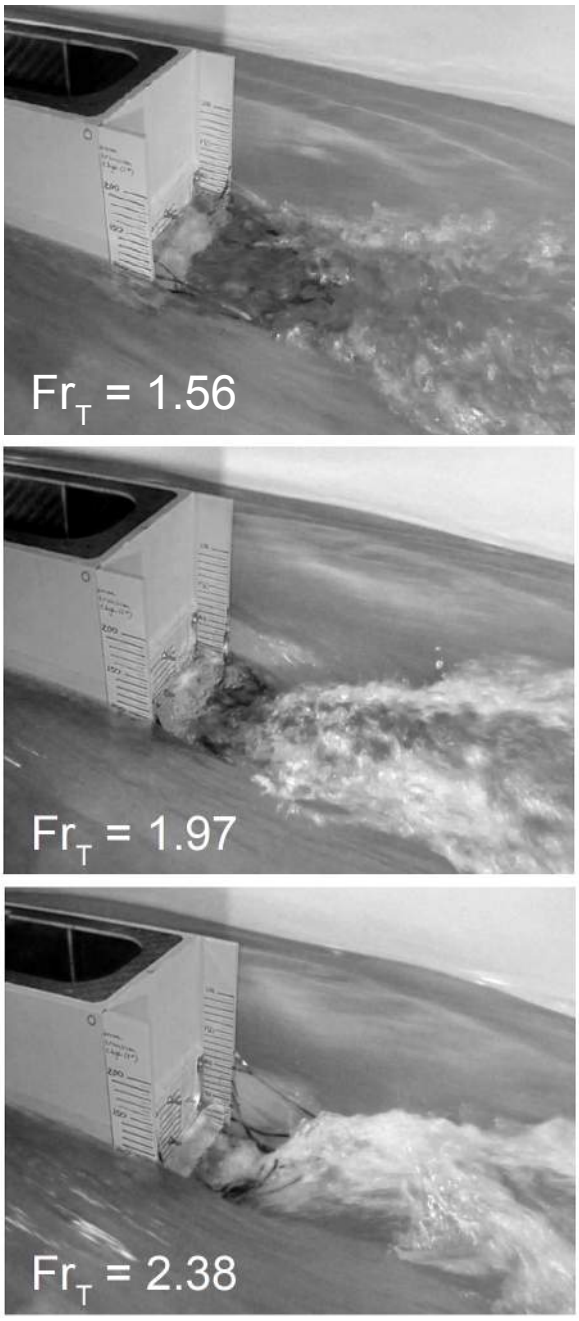

Figure 5.4: Flow past the transom at different speeds of Froude numbers of $Fr = 0.24$, 0.30 and 0.36, corresponding to transom draft Froude numbers of $Fr_T = 1.56$, 1.97 and 2.38.

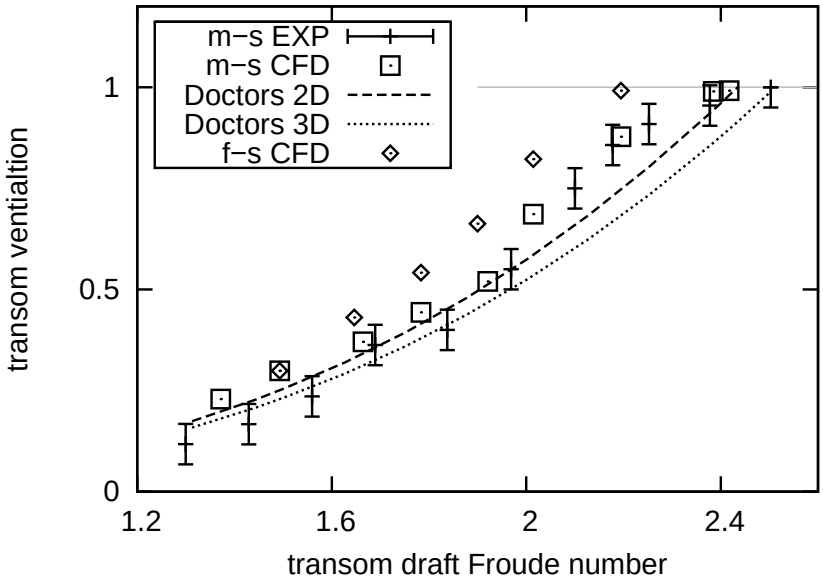

Figure 5.5: State of transom ventilation where 0 means fully wet and unity fully dry with respect to transom Froude number. Results are based on CFD simulation at model and full scale, experimental measurements and empirical predictions using Doctors et al. (2007) with and without taking limited B_T/T_T values into account.

5.3.3 Emperical Prediction

The empirical prediction by Doctors et al. (2007) using the static transom draft as measured at the physical model scale testing reached the dry state at $Fr_T = 2.56$ when considering an infinitely wide transom (2D) and at $Fr_T = 2.43$ when taken the B_T/T_T ratio into account (3D). Both empirical approaches predict the level of transom ventilation within the experimental error for $Fr_T \leq 2$ and matched the dry state at a transom draft Froude number less than 1% (3D) and 3% (2D) different from the measured value. Between these speeds the empirical formulation underestimated the ventilation state, which is in accordance with the original experiments from which the regression was derived.

5.3.4 Qualitative Validation of Transom Flow

In the post-processing of the CFD simulations the stream tracers were seeded to correlate to the experimental model set-up. The length and width of the virtual stream tracers were matched with the experimental stream tracers to study if the numerical simulation is capable of predicting flow characteristics that are comparable to the experimentally observed ones.

5.3.5 Steady Observations

Two speeds were used to compare the flow features between simulations and model test experiments. Firstly $V = 1.30$ and 1.95 m/s corresponding to $Fr_T = 1.37$ and 1.29 for the lower speed and $Fr_T = 2.01$ and 1.97 for the higher speed at CFD simulations and in the experiment due to different transom drafts despite identical model length and mass displacement, which most likely results from model building imperfections. The perspective of the experimental image was matched in the CFD post-processor and the results compared as shown in Figures 5.6 and 5.7. For the lower speed it can be seen that in the experiment most of the tracers follow the recirculation of the flow and have their tips pointing towards the transom, while a few align with the continuing flow and their tips point away from the vessel. The same behaviour can be observed in the image generated by the numerical simulation, especially the point from where the streamlines either point towards the stern or away from it is well predicted in CFD when comparing to the experimental snap shot. Additional features of the flow can be observed in Figure 5.6: the intersection of water level and tank wall, due to capillary deformation of the water surface as marked by (A); the bumpy small-scale wake features due to wave breaking marked by (B); and the distance between the water level around the stern and at the transom has been marked (C). Subjectively, the numerical approach is capable of replicating these features. For the higher speed shown in Figure 5.7 the stagnant area as determined by model test experiments is clearly smaller when compared to the lower speed shown in Figure 5.6. As for the lower speed, most stream tracers are experiencing recirculation, while single ones may follow the main flow. The depression of the free surface (C) at the transom can be seen to be more pronounced. When comparing the CFD-produced image to the experimental one, a similar alignment of the stream tracers can be observed. Also the water level at the tank wall (A), and the turbulent wake structures (B) are well reproduced in CFD compared to the experimental observations.

The bottom view of the stagnant zone has been visualised for the slow speed only due to vibrations and asymmetric forces on the camera at higher speeds. Nevertheless, at $V = 1.30\ m/s$ good agreement between the numerical visualisations and experimental results can be seen in Figure 5.8. Either the stream tracers appear as straight lines until they start to wiggle and eventually point towards the vessel and indicate recirculation, or they randomly point somewhere due to the unsteadiness of the flow in this area. Otherwise when they align with the surrounding flow they point away from the vessel. The distance until the stream tracers start oscillating is comparable between the two images.

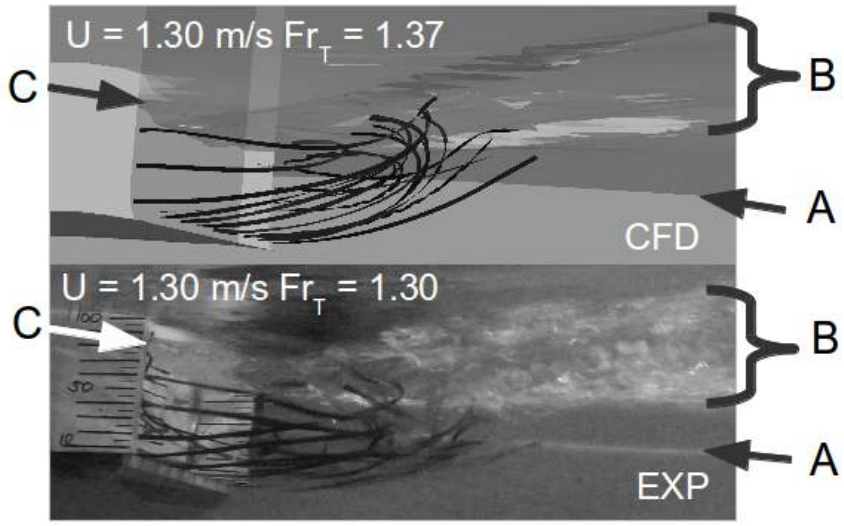

Figure 5.6: Side view: Comparison of flow past partially ventilated transom at transom draft Froude number $Fr_T = 1.30$ and 1.37 between physical experiment (bottom) and numerical simulation (top).

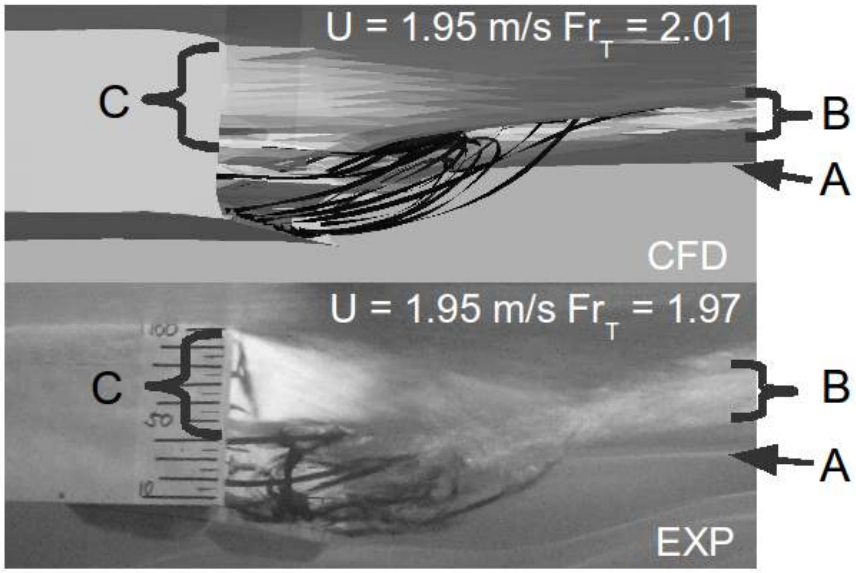

Figure 5.7: Profile view: comparison of flow past partially ventilated transom at transom draft Froude number $Fr_T = 1.97$ and 2.01 between physical experiment (bottom) and numerical simulation (top).

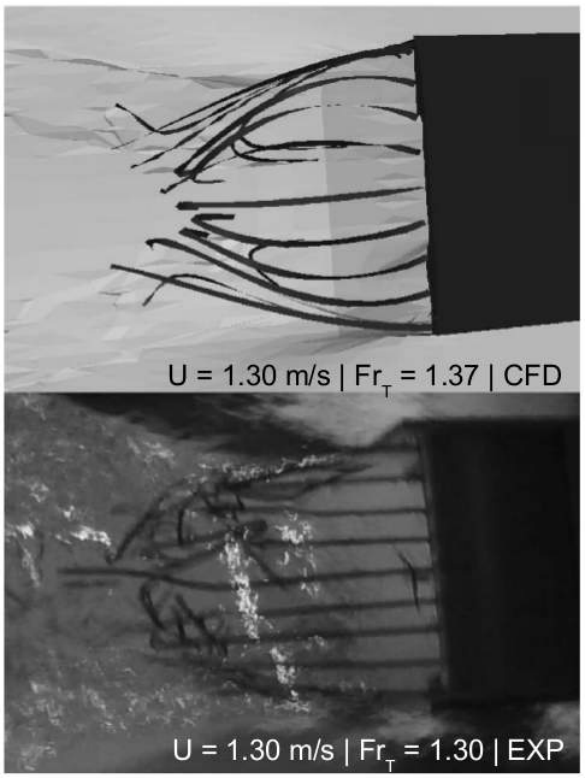

Figure 5.8: Bottom view: comparison of flow past partially ventilated transom at transom draft Froude number $Fr_T = 1.30$ and 1.37 between physical experiment (bottom) and numerical simulation (top).

Unsteady Observations

From visual observations of the model test experiments it was seen that the root part of the stream tracers were almost steadily aligned with the flow while the tips underwent random oscillations due to the unsteadiness of the wake. These observations were made in the unsteady RANS simulations too, however they were less pronounced when compared to the experiment. Maki et al. (2006) and Bhushan et al. (2012) predicted a von-Karman-type vortex shedding for transom draft Froude numbers exceeding unity at an infinitely wide transom, but such unsteady behaviour was neither identified in the numerical simulation nor seen in the physical model testing for $Fr_T > 1.0$. In the experiments an unsteady fluctuation for $Fr_T > 2.10$ was seen that could be explained by a von-Karman-type shedding, however it could have also been induced by portions of water that were shed from the rooster tail towards the transom. It is assumed that the contribution of the flow from the sides of the vessel influences the flow features inside the stagnant zone so that a stable and non-shedding structure builds up for the majority of the speed range between $1.0 < Fr_T < Fr_T(dry)$.

5.4 Characteristics of Flow Past Transom

In Section 5.3.4 it was shown that the state of transom ventilation predicted by the numerical simulation was within the experimental error for $Fr_T > 1.6$. Also, the numerically determined flow structure was found to be in good qualitative agreement with that experimentally observed. Therefore the flow structure obtained from CFD can be assumed as being physically correct and the numerical results can be used to describe the flow feature in more detail and undertake further investigation.

5.4.1 Flow in Stagnant Area

The number of stream traces used in the post-processing of the simulation was increased to visualise the flow structure with greater resolution. As can be seen in Figure 5.9, the flow can be described as a squashed horseshoe vortex (Figure 5.9 a). From the profile view (Figure 5.9 b) it can be seen that a recirculating roller occurs where the flow at the bottom part is aligned with the surrounding bulk flow, while the plan view shows that two counter rotating vortical structures are present (Figure 5.9 c). At the end of the stagnant area the flow rises and turns towards the stern of the vessel. In the aft perspective (Figure 5.9 d) it can be seen that the stagnant flow structure points up to the centre plane of the demihull, which is where the rooster tail shoots up in the wake of the vessel. Finally, if the flow in the stagnant area is

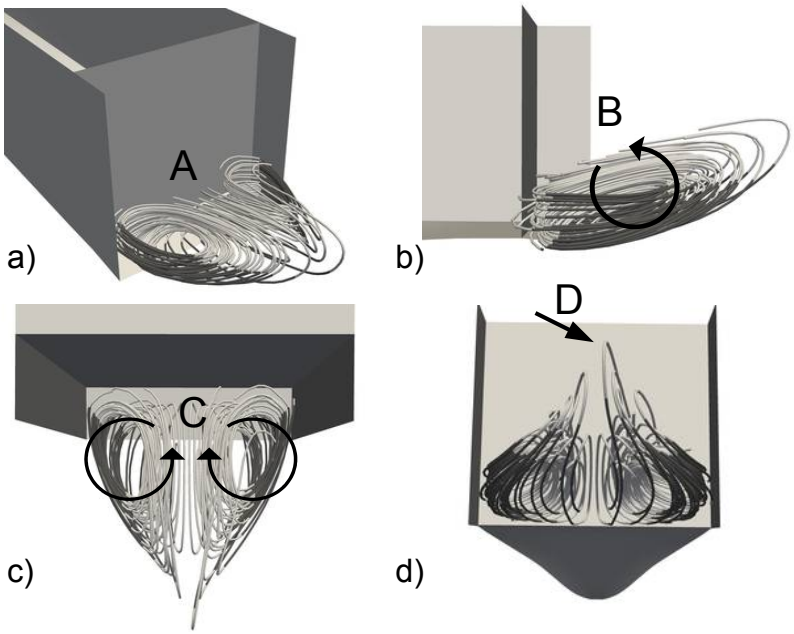

Figure 5.9: a) Squashed horseshoe structure of the flow inside the stagnant area behind the transom (A) at $Fr_T = 1.66$; b) Profile view indicates the reversing behaviour (B) of the stagnant flow; c) Plan view shows the two counter rotating vortices at the upper side of the stagnant area; d) Aft view indicates the rising streamlines (D) that will potentially form the characteristic rooster tail in the wake.

looked at from an angle (Figure 5.9 a), it can be seen that it is a single coherent structure that combines both features and hence can be best described as a squashed horseshoe vortex. When the speed increases the length and height of the squashed horseshoe decreases, but the principal features remain.

5.4.2 Process of Transom Ventilation

The quasi-steady process of transom ventilation is presented as illustrated in Figure 5.11. The flow structure, as well as the free surface, is presented, with the latter only shown for the starboard side of the port side demihull. The free surface was assumed to be where the value for volume fraction equals 0.5. However, when wave breaking happens volume fractions between zero and unity may occur over a wide range of cells and the interface between air and water is not sharp. Therefore the streamlines were scaled with respect to volume fraction, so that a reduced diameter of the streamline indicates wave breaking in the recirculating flow. The recirculating part is represented by red lines, while the water moving away from the transom is shown by blue lines. Figure 5.11 shows the flow structure and free surface for $1.37 \leq Fr_T \leq 2.42$. It can be seen that the size of the stagnant flow area reduces,

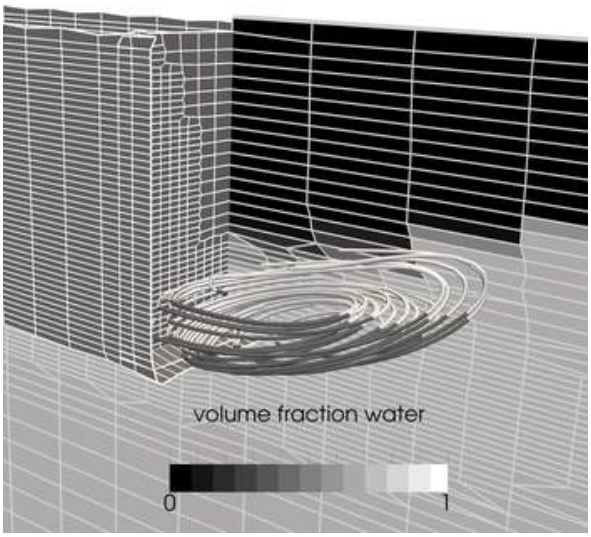

Figure 5.10: Mesh structure and predicted flow past transom and the distribution of volume fraction at the centre plane of the demihull.

firstly in height due to the decreasing water level at the transom at $Fr_T = 1.37 - 2.01$ and secondly in length which may be explained by the reduced height of the flow structure. At $Fr_T = 1.92$ it can be seen that the free surface suffers from wave breaking which results in an uncertain interface. A similar effect happens at $Fr_T = 2.01$ too, but to a larger extent as a reduced diameter of streamlines in the recirculating flow further supports the wave breaking occurrence. At $Fr_T = 2.19$ the transom ventilation is 0.88; it is the highest speed with a partially wet transom and very thin recirculating streamlines indicate strong wave braking. This behaviour was also seen in the experiment as shown in Figure 5.12. The white arrow points to a fluid portion that occurs in breaking waves and splashes towards the transom, the majority of the recirculation happens by this kind of wave breaking. Of course this process is highly unsteady and the image just presents a snapshot of the phenomenon. At $Fr_T = 2.28$ and 2.42 the flow clearly separates and leaves the transom dry. In contrast, in the experiment at $Fr_T = 2.25$ and 2.38 the transom ventilation was 0.91 and 0.95 respectively. This discrepancy may be explained by the reduced size of the flow structures of the breaking wave that are unresolved by the computational mesh. These will shed off from the rooster tail and roll down towards the transom, as characterised as flow regime C in Figure 5.1.

5.4.3 Results at Full-Scale

For the current case the simulations were repeated at hydrodynamic full scale and the transom ventilation analysed as specified in Section 5.3.2. The results are presented in Figure 5.5, together with the model-scale results. It can be observed that the transom for $Fr_T < 1.6$ is

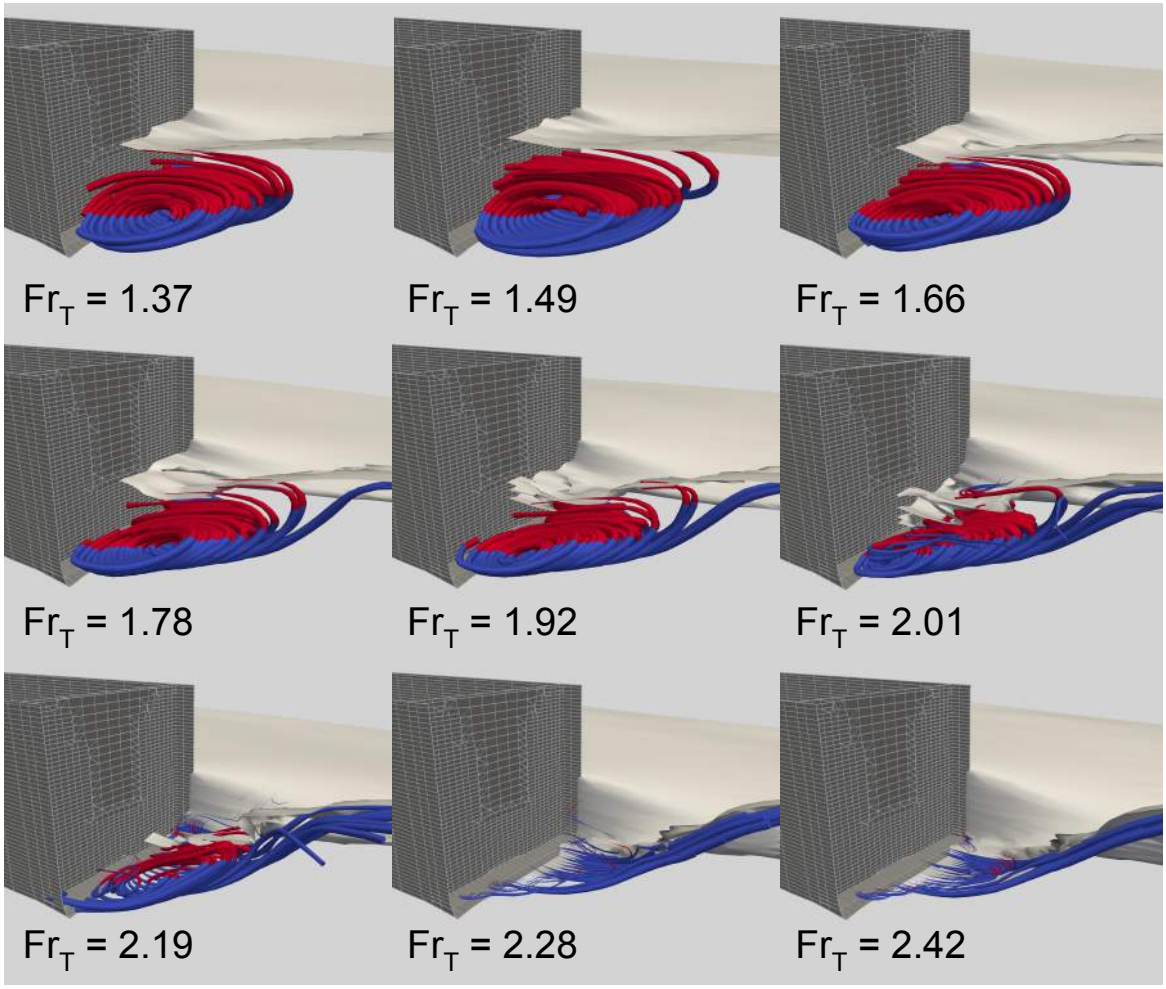

Figure 5.11: Flow structure and free surface behind the transom undergoing the ventilation process at model scale. Red streamlines present recirculating flow and and a reduced streamline diameter indicates wave breaking.

Figure 5.12: Image of the transom including the built-up of a rooster tail at $Fr_T = 2.19$. The arrow points at a fluid portion that represents breaking flow recirculation.

more ventilated at larger Reynolds numbers and hence the dry state is reached earlier. At transom draft Froude numbers below 1.6 the change in Reynolds number does not influence the ventilation state. With the values from the current investigation it can be concluded that the full-scale transom becomes dry at $Fr_T = 2.2$, in contrast to $Fr_T = 2.4$ in the model-scale simulations.

This difference can be explained by the reduced boundary layer thickness at full-scale Reynolds numbers. Therefore, the full-scale flow induces a lower pressure than the model-scale flow and hence will reduce the water level at the transom to a larger extent. This presents another example why it may not be feasible to linearly scale ship hydrodynamic properties from model-scale observations to the full-scale ship (Cusanelli, 2011). Therefore non-linear tools for resistance extrapolation, such as the CFD-based approach in conjunction with model test experiments as postulated in Chapter 3, may be superior for accurate full-scale drag prediction when compared to traditional ITTC extrapolation methods.

5.4.4 Impact of Transom Ventilation on Drag Force

A deviation in drag force between the numerical prediction and experimental measurement for the partially wetted transom was observed and reached up to 10%. However valid conclusions on the accuracy of the numerical approach cannot be drawn, as the transom draft between both cases varied too. Despite an identical mass displacement, the transom draft was 110 mm in experiments while it was 100 mm in the simulations. Possible reasons for this difference are model-building imperfections, because the draft in the simulations adhered with the original

hydrostatics. The numerical simulation revealed that for the speed range under consideration, the hydrostatic drag due to the transom contributes 50% to the total drag of the vessel at model scale and even up to 70% for the full-scale ship. Its impact reduces with increasing speed, as it is a hydrostatic phenomenon the transom drag force is purely dependent on the water level at the stern and does not increase with velocity squared, such as wave-making or friction drag do (Starke et al., 2007).

This may explain why quite substantial deviations in drag force occur for vessel speeds that feature a partially wet transom, as reported in Chapters 3, 4 and 6 as deviations in transom draft and ventilation state have a significant impact on the vessel's drag force and hence powering requirements.

5.5 Conclusions

This study has shown that the flow in the stagnant area could be best described as a non-shedding squashed horseshoe vortex, which behaves like a recirculating roller at the centre plane of the stagnant zone and two counter rotating vortices at the top of the stagnant zone. Other researchers predicted a periodic von-Karman vortex shedding from the transom edge for transom draft Froude numbers exceeding unity for transom flows of infinitely wide transoms, or those of combatant hull forms. However, for the wave-piercing hull form under consideration no such periodic shedding was observed, neither in experiments nor numerical simulations. This may be due to the three-dimensional nature of the flow. For a transom draft Froude number exceeding 2.2, an unsteady fluctuation occurs, but cannot be clearly identified as the von-Karman-type shedding.

Also the process of transom ventilation has been visualised in a quasi-steady manner and shows the transition from a partially wetted state to a fully dry state including a recirculation in the form of a squashed horseshoe vortex and breaking waves just before the fully dry state occurs. These three phenomena of partially wet, breaking recirculation, and fully dry obtained through numerical simulation qualitatively agreed to observations from model test experiments.

Furthermore, it has been demonstrated that the unsteady RANS-based simulations are capable of quantitatively predicting the flow past a partially ventilated transom for a wave-piercing catamaran hull form. The agreement has been within the experimental error of 4.5% between numerical predictions and experimental measurements for transom draft Froude numbers exceeding 1.6 has been achieved on a standard mesh with no additional refinements in the

vicinity of the transom. Increasing speed and therefore an increasing transom draft Froude number leads to a reduction in the water level at the transom, until it reaches dry state at transom Froude number of $Fr_T = 2.50$ as determined in physical model test experiments. The numerical simulation predicted the dry state transom Froude number of $Fr_T = 2.42$ at model scale and at $Fr_T = 2.20$ at full-scale Reynolds numbers which leads to the fact that model-scale results cannot be directly applied to a full-scale ship.

The drag due to the transom stern can be the main contributor to the total drag, in the current study it contributed 50% at model-scale and even 70% at full-scale to the total vessel drag. Hence inaccuracies or deviations in modelling the transom and predicting the flow around can have a large impact on the total drag force.

Despite the encouraging results of this study one has to bear in mind that the flow past a transom stern features some highly unsteady small-scale flow features that are neither resolved on a standard mesh, nor by unsteady RANS simulations. Hence the appropriate simulation techniques depends on the application and the scope of the study, however for simulating the water level at the transom and resolving the macro flow features past the transom the presented method can be considered as being adequate.

5.5.1 Recommendations for Future Work

In future studies the simulation should be validated at identical transom draft to assure its capability to correctly predict the drag force during the partially wetted transom stage. Furthermore, the effect of a waterjet propulsor or a propeller may be considered, as this will influence the flow around the hull before reaching the transom and therefore the ventilation process. Also the jet of water leaving the waterjet nozzle will change the flow characteristics in the stagnant zone during non to partially ventilated conditions and potentially the build-up of the rooster tail for partially to fully ventilated conditions.

5.6 Where to next?

In this chapter the ability of the CFD-based approach to accurately predict the flow past a partially ventilated transom of a wave-piercing catamaran demihull has been demonstrated. Thus, there is a sufficient level of confidence to apply this methodology to perform a hull form design study for large medium-speed catamarans to minimise calm water drag. In the next chapter a comprehensive study of varied hull form features including demihull slenderness ratio and draft, at a range of medium-speed Froude numbers, is performed to derive guide-

lines for the hull form design of these craft with maximum transport efficiency and hence minimising emissions and fuel costs.

Chapter 6

Hydrodynamic Hull Form Design Space Exploration of Large Medium-Speed Catamarans Using Full-Scale CFD

This Chapter has been accepted for publication and the current citation for the research article is:

M. Haase, G. Davidson, S. Friezer, J. Binns, G. Thomas, and N. Bose (2015c). "Hydrodynamic Hull Form Design Space Exploration of Large Medium-Speed Catamarans Using Full-Scale CFD". in: *Transaction of the Royal Institution of Naval Architects, Part A - International Journal of Maritime Engineering* 157.A3, pp. 161–174

The current version of this chapter has been modified compared to the accepted version to guide the reader more conveniently through this thesis.

This chapter has been removed for copyright or proprietary reasons.

Chapter 7

Conclusions

The primary motivation for this work was to establish design guidelines and to quantify the fuel-saving potential of large medium-speed catamarans to promote economically viable and environmentally sustainable fast sea transportation. The available literature has been surveyed to derive initial design guidelines and identify appropriate hull form parameters such as demihull slenderness ratio and demihull separation ratio. These required more detailed investigation to obtain values applicable to large medium-speed catamarans to provide minimum drag and maximum transport efficiency. A novel approach based on computational fluid dynamics (CFD) has been developed to accurately predict the hull performance at full scale, including the evaluation of its capability to assess the drag properties in restricted water and to investigate characteristic flow features such as the recirculation past a deep transom. Finally, this new CFD-based technique has been used to study a wide range of hull forms to identify the most applicable hull properties for fuel-efficient fast sea transportation.

7.1 Achievements

Guidelines for full form parameters such as prismatic coefficient, hull slenderness ratio and transom immersion with values for lowest drag at a certain Froude number have been derived by analysing the current knowledge in ship design. However, a case study based on available extrapolated model test data revealed that demihull slenderness ratios exceeding a value of 10 can lead potentially to further reductions in drag for speeds beyond 25 knots. However, sufficient reference data for design purposes was not available and to further interrogate the design space for values of slenderness ratios providing the lowest possible drag. Numerical simulations have the potential to directly predict the performance of the full-scale vessel without relying on empirical linear extrapolation methods, such as those proposed by the

International Towing Tank Conference (ITTC). Therefore a novel CFD-based approach has been proposed which utilises model test experiments for verification and employs the same mesh for drag prediction at model-scale and at full-scale Reynolds number. This is achieved by altering fluid viscosity to change Reynolds numbers instead of linear dimensions.

A flat plate study has revealed that consistent first cell height of $y_1 = 0.6 \times L \times 10^{-6}$ can be used for model and full-scale Reynolds numbers, without compromising the accuracy of the predicted wall shear stress on a smooth surface. This flat plate study also showed that effects of surface roughness on the shear force are accurately predicted when compared to theoretical values. The full-scale CFD approach has been successfully validated for a 98 m catamaran for Froude numbers of 0.40 and 0.43 including surface roughness effects where variations in resistance have been as low as 5% when compared to full-scale drag derived from existing sea trials using measured shaft power and the characteristic thrust curves of the waterjet unit. Using empirical correlation and roughness allowance for ship hulls predicts a lower impact of roughness on the drag force than the CFD results for Reynolds numbers of $log(Re) > 8.75$, which would be applicable for a 130 m medium-speed catamaran. It has been shown that this difference can lead to a 20% higher total drag prediction by the CFD simulations when compared to empirically extrapolated resistance data, while the deviation for a smooth hull has been within $\pm$ 5%.

This numerical approach can also be utilised for the extrapolation of model test data without relying on the assumptions made by ITTC procedures, such as linear resistance decomposition, a form factor, empirical model-ship correlation lines, or empirical corrections for roughness and correlation allowance which may not be correct. For example, it has been shown that certain flow phenomena do not scale linearly, such as the shear force which is sensitive to both Reynolds and Froude numbers, or full transom ventilation which occurs at lower speeds at full-scale Reynolds numbers when compared to model scale investigations.

Furthermore, effects of restricted waters on the drag force, which may occur during physical model testing, ship operation or both can be accurately predicted with the proposed numerical approach. In shallow water with a depth of 0.24 times model length, the experimental test results were matched with deviations in drag not exceeding 3% in design conditions, and a shear force coefficient within 4% of the ITTC correlation value. However at full scale, CFD predicts up to 35% larger frictional drag component when compared to the correlation line value of ITTC which may result from the higher velocity of the surrounding flow due to the close proximity of the sea bed, an effect that is not incorporated in current extrapolation approaches of ITTC. In addition it was found that at Froude numbers of $Fr = 0.45$, in shallow

water with a depth of 0.24 times the vessel length, the required width of the fluid domain needs to be more than 10 times wider when compared to a speed at a Froude number of $Fr = 0.37$ to avoid an increase in residuary resistance by more than 1% when compared to an infinitely wide domain. This shows clear advantages of using a flow resolving approach to extrapolate model test data and implies that this prediction methodology can also be used to determine model sizes for towing tank experiments while keeping the effects of restricted water to an agreed minimum.

These finite water effects are not only of steady nature, the oscillation period of the ship response in model testing have been shown to increase for increasing speed and decreasing depth to an extent that less than a full motion cycle was resolved during a run of the full length of the towing tank. This effect is physical as it has been shown to occur in experiments, numerical simulations and full-scale sea trials.

Another capability of CFD simulations is to correctly predict the flow past the partially ventilated transom of a wave-piercing catamaran hull and to identify characteristic flow features which were found to agree with observations in model test experiments. It has been found that for catamaran demihulls of wave-piercing type, the von-Karman-type vortex shedding off the transom edge does not occur as expected for an infinitely wide transom. The flow inside the stagnant zone has been identified as a non-shedding squashed horseshoe vortex. Variations in transom draft may lead to deviations in drag force of up to 10% for the same vessel at speeds where the transom is only partially ventilated.

Finally, the developed numerical tool has been utilised to compare the drag force and transport efficiency of catamarans of 110 m to 190 m in length with constant overall width and comparable deadweight capacities. Each length represents a different value of demhill slenderness ratio. It was found that demihull slenderness ratios of $L/\nabla_{dh}^{1/3} = 11 - 13$ will provide the most favourable resistance properties. This is close to recommendations in literature where appropriate values for lowest resistance were stated for overall slenderness ratios of $L/\nabla_{dh}^{1/3} = 8 - 10$, which corresponds, for a catamaran, to a demihull slenderness ratios of $L/\nabla_{dh}^{1/3} = 10 - 12.5$. For the demihull separation ratios under consideration, it was found that changing the demihull separation by the beam of a demihull has no significant effect on the drag force.

Appropriate vessel lengths for highest transport efficiency at service speeds of 20 – 35 knots at different loading conditions have been determined, and for speeds of 25 knots and below a hull length of 130 m and 150 m provided the highest transport efficiency at light displacement conditions at a draft of 3.1 m. If exceeding 28 knots, hull lengths of 150 m and 170 m were

most beneficial for delivering the lowest fuel consumption per deadweight carried, a figure that shifts towards longer hulls if the draft and hence displacement increased: At a draft of 3.6 m, hull lengths of 150 m and 170 m provided the highest transport efficiency for speed of 28 knots and below, while for higher speeds hull lengths of 170 m and 190 m are the best choice from a fuel consumption perspective.

If the derived transport efficiencies for large medium-speed catamarans are then set in relation to those of currently operating large fast catamarans, a 67% increase in transport efficiency can be achieved if a 170 m hull is used when compared to a contemporary 112 m hull. This saving equals a 40% reduction in fuel consumption per deadweight tonnes per distance travelled. Consequently, it also means 40% of savings in emissions and fuel costs and proves that the concept of large medium-speed catamarans has the potential to provide an energy-efficient alternative to current modes of fast sea transportation.

Despite these encouraging results it should be noted that the achieved values for demihull slenderness ratios which provided the lowest drag may not be universally valid, as the optimum value may change if the applicable Reynolds number of the vessel under consideration is different by an order of magnitude to those presented in this study. For example, if significant changes in demihull separation are applied, either far apart or very close to each other, or possibly if general hull form features change. Similarly, the values for hull form parameters determined in a literature survey may not be providing the lowest drag as they are: based on built ships, may not have been optimised for resistance; or changes in production technology may have influenced optimum values of hull form parameters for lowest drag.

The validity of the full-scale drag predictions using CFD cannot be generally concluded and may only be accepted for the current type of vessel and if it is assured that all significant physical flow phenomena are sufficiently accurately resolved. When performing a verification at model scale, only model-scale flow phenomena are taken into account. This may be incorrect for a ship if, for example, strong wave-breaking or spray occurs at the full-scale vessel but not at model scale. Satisfyingly, for large wave-piercing catamarans the drag due to wave breaking and spray can be assumed as being negligible.

For transient resistance prediction in shallow water, long-period oscillations and slow convergence behaviour in the ship response during towing tank tests and numerical simulations has been observed. Hence to accurately replicate model test experiments using CFD the acceleration phase and the limited length of the towing tank may be taken into consideration to decrease the deviation between numerical and experimental results.

Lastly, the flow features presented for the transom stern flow can be considered as being valid as long as no propulsor is present. A waterjet or a propeller may induce high velocities in longitudinal direction below or above the transom edge, which may considerably influence the shape of the stagnant flow feature and level of transom ventilation.

7.2 Recommendations for Future Studies

This research has found the answer to many questions related to contemporary ship design, but also has raised several more that should be answered in future research studies. From a full-scale resistance prediction perspective it is important to investigate if the proposed approach is applicable to other types of ships, especially where effects that influence the full-scale drag may occur differently at model scale, such as that of wave-breaking at the bow.

The validation of the CFD-based approach at full-scale relied on a series of assumptions, with the most critical being the drag thrust equilibrium. Therefore for a waterjet powered vessels, new ways of resistance prediction from sea trials need to be explored, such as possible correlations between flow rate and ship speed, two quantities that can be directly measured or determined at the full-scale vessel or in the numerical simulation. This approach would require integrating a computational model of the waterjet system into the hull.

The numerical design space exploration concluded only on appropriate slenderness ratios and that minor changes in demihull separation do not significantly influence the drag force. Although other parameters are likely to have a second order effect, it is not known how the results may change if parameters such as prismatic coefficient are altered, in addition to slenderness ratio. The study could be repeated where the most appropriate values of prismatic coefficient based on findings from the literature survey are applied at each speed.

The exploration of the design space took varying light ship weight into account when establishing the resulting transport efficiency. It has to be kept in mind that a longer vessel will imply much higher initial costs and that vessels should be compared using full life cycle costs, rather than drag to lift ratios such as drag non-dimensionalised by displacement force or dead weight to quantify the complete economic feasibility of different hull designs.

Chapter 8

APPENDIX

Simulation Set-up

This appendix summarises the most important setting for performing the numerical simulation using OpenFOAM. Each case consist of a time, constant and system directory. The time directory, contains the boundary and initial condition of the different field variables, and the constant directory features all constant parameters, such as fluid and transport properties, mass and inertia information and most importantly, the mesh. The system directory contains all variables to solve the equations, including time step and numerical schemes.

Time Directory

The *time* directory includes files specifying the boundary conditions on the boundary patches (INLET, OUTLET, SYM, FARPS, TOP, BOTTOM, SHIP). The initial quantities were defined in the *flowVelocity* file in the main directory. These files include:

- *alpha.water*: Volume fraction
- k: Kinetic turbulent energy
- *nut*: Eddy viscosity
- *p_rgh*: Dynamic pressure
- *pointDisplacement*: Displacement of mesh points due to dynamic mesh motion
- *omega*: Dissipation rate
- U: Flow velocity

```
/*--------------------------------*- C++ -*----------------------------------*\
| =========                 |                                                 |
| \\      /  F ield         | OpenFOAM: The Open Source CFD Toolbox           |
|  \\    /   O peration     | Version:  2.3.0                                 |
|   \\  /    A nd           | Web:      www.OpenFOAM.com                      |
|    \\/     M anipulation  |                                                 |
\*---------------------------------------------------------------------------*/
FoamFile
{
    version     2.0;
    format      ascii;
    class       volScalarField;
    location    "0";
    object      alpha1;
}
// * * * * * * * * * * * * * * * * * * * * * * * * * * * * * * * * * * * * * //

dimensions      [0 0 0 0 0 0 0];

internalField   uniform 0 ;

boundaryField
{
    INLET
    {
        type            fixedValue;
        value           $internalField
    }
    FARPS
    {
        type            zeroGradient;
    }
    OUTLET
    {
        type            variableHeightFlowRate;
        lowerBound      0;
        upperBound      1;
        value           $internalField;
    }
    BOTTOM
    {
        type            zeroGradient;
    }
    SYM
    {
        type            symmetryPlane;
    }
    TOP
    {
        type            inletOutlet;
        inletValue      $internalField;
        value           $internalField;
    }
    SHIP
    {
        type            zeroGradient;
    }
}


// ************************************************************************* //
```

Figure 8.1: Set-up for volume fraction.

```
/*--------------------------------*- C++ -*----------------------------------*\
| =========                 |                                                 |
| \\      /  F ield         | OpenFOAM: The Open Source CFD Toolbox           |
|  \\    /   O peration     | Version:  2.3.0                                 |
|   \\  /    A nd           | Web:      www.OpenFOAM.com                      |
|    \\/     M anipulation  |                                                 |
\*---------------------------------------------------------------------------*/
FoamFile
{
    version     2.0;
    format      ascii;
    class       volScalarField;
    location    "0";
    object      k;
}
// * * * * * * * * * * * * * * * * * * * * * * * * * * * * * * * * * * * * * //
#include "../flowVelocity"

dimensions      [0 2 -2 0 0 0 0];

internalField   $k;

boundaryField
{
    INLET
    {
        type            fixedValue;
        value           uniform $k;
    }
    OUTLET
    {
        type            zeroGradient;
    }
    TOP
    {
        type            zeroGradient;
    }
    BOTTOM
    {
        type            zeroGradient;
    }

    FARPS
    {
        type            zeroGradient;
    }
    SYM
    {
        type            symmetryPlane;
    }
    SHIP
    {
        type            kqRWallFunction;
        value           uniform $k;
    }
}


// ************************************************************************* //
```

Figure 8.2: Set-up for kinetic turbulent energy.

```
/*--------------------------------*- C++ -*----------------------------------*\
| =========                 |                                                 |
| \\      /  F ield         | OpenFOAM: The Open Source CFD Toolbox           |
|  \\    /   O peration     | Version:  2.3.0                                 |
|   \\  /    A nd           | Web:      www.OpenFOAM.com                      |
|    \\/     M anipulation  |                                                 |
\*---------------------------------------------------------------------------*/
FoamFile
{
    version     2.0;
    format      ascii;
    class       volScalarField;
    location    "0";
    object      nut;
}
// * * * * * * * * * * * * * * * * * * * * * * * * * * * * * * * * * * * * * //
#include "../flowVelocity"

dimensions      [0 2 -1 0 0 0 0];

internalField   uniform $nut;

boundaryField
{
    INLET
    {
        type            calculated;
        value           uniform 0;
    }
    OUTLET
    {
        type            calculated;
        value           uniform 0;
    }
    TOP
    {
        type            calculated;
        value           uniform 0;
    }
    BOTTOM
    {
        type            calculated;
        value           uniform 0;
    }
    FARPS
    {
        type            calculated;
        value           uniform 0;
    }
    SYM
    {
        type            symmetryPlane;
    }
    SHIP
    {
        type            nutkWallFunction;
        value           uniform $nut;
    }
}


// ************************************************************************* //
```

Figure 8.3: Set-up for eddy viscosity.

```
/*--------------------------------*- C++ -*----------------------------------*\
| =========                 |                                                 |
| \\      /  F ield         | OpenFOAM: The Open Source CFD Toolbox           |
|  \\    /   O peration     | Version:  2.3.0                                 |
|   \\  /    A nd           | Web:      www.OpenFOAM.com                      |
|    \\/     M anipulation  |                                                 |
\*---------------------------------------------------------------------------*/
FoamFile
{
    version     2.0;
    format      ascii;
    class       pointVectorField;
    location    "0.01";
    object      pointDisplacement;
}
// * * * * * * * * * * * * * * * * * * * * * * * * * * * * * * * * * * * * * //

dimensions      [0 1 0 0 0 0 0];

internalField   uniform (0 0 0);

boundaryField
{
    #include "${WM_PROJECT_DIR}/etc/caseDicts/setConstraintTypes"

    INLET
    {
        type            fixedValue;
        value           uniform (0 0 0);
    }
    OUTLET
    {
        type            fixedValue;
        value           uniform (0 0 0);
    }
    BOTTOM
    {
        type            fixedValue;
        value           uniform (0 0 0);

    }
    TOP
    {
        type            fixedValue;
        value           uniform (0 0 0);
    }
    SYM
    {
        type            symmetryPlane;

    }
    FARPS
    {
        type            fixedValue;
        value           uniform (0 0 0);

    }
    SHIP
    {
        type            calculated;
    }
}


// ************************************************************************* //
```

Figure 8.4: Set-up for point displacement.

```
/*--------------------------------*- C++ -*----------------------------------*\
| =========                 |                                                 |
| \\      /  F ield         | OpenFOAM: The Open Source CFD Toolbox           |
|  \\    /   O peration     | Version:  2.3.0                                 |
|   \\  /    A nd           | Web:      www.OpenFOAM.com                      |
|    \\/     M anipulation  |                                                 |
\*---------------------------------------------------------------------------*/
FoamFile
{
    version     2.0;
    format      ascii;
    class       volScalarField;
    location    "0";
    object      p_rgh;
}
// * * * * * * * * * * * * * * * * * * * * * * * * * * * * * * * * * * * * //

dimensions      [1 -1 -2 0 0 0 0];

internalField   uniform 0;

boundaryField
{
    INLET
    {
     type               fixedFluxPressure;
        value           $internalField;

        }
    OUTLET
    {
        type            zeroGradient;
    }
    TOP
    {
        type            totalPressure;
        U               U;
        phi             phi;
        rho             none;
        psi             none;
        gamma           1;
        alpha1           1;
        p0              uniform 0;
        value           uniform 0;
    }
    BOTTOM
    {
        type            zeroGradient;
    }

    FARPS
    {
        type            zeroGradient;
    }
    SYM
    {
        type            symmetryPlane;
    }
    SHIP
    {
        type            fixedFluxPressure;
        value           $internalField;
    }
}
```

Figure 8.5: Set-up for dynamic pressure.

```
/*--------------------------------*- C++ -*----------------------------------*\
| =========                 |                                                 |
| \\      /  F ield         | OpenFOAM: The Open Source CFD Toolbox           |
|  \\    /   O peration     | Version:  1.7.0                                 |
|   \\  /    A nd           | Web:      www.OpenFOAM.com                      |
|    \\/     M anipulation  |                                                 |
\*---------------------------------------------------------------------------*/
FoamFile
{
    version     2.0;
    format      ascii;
    class       volScalarField;
    location    "0";
    object      omega;
}
// * * * * * * * * * * * * * * * * * * * * * * * * * * * * * * * * * * * * * //
#include "../flowVelocity"

dimensions      [0 0 -1 0 0 0 0];

internalField   uniform $omega;

boundaryField
{
    INLET
    {
        type            fixedValue;
        value           uniform $omega;
    }
    OUTLET
    {
        type            zeroGradient;
    }
    TOP
    {
        type            zeroGradient;
    }
    BOTTOM
    {
        type            zeroGradient;
    }
    FARPS
    {
        type            zeroGradient;
    }
    SYM
    {
        type            symmetryPlane;
    }
    SHIP
    {
        type            omegaWallFunction;
        value           uniform $omega;
    }
}


// ************************************************************************* //
```

Figure 8.6: Set-up for dissipation rate.

```
/*--------------------------------*- C++ -*----------------------------------*\
| =========                 |                                                 |
| \\      /  F ield         | OpenFOAM: The Open Source CFD Toolbox           |
|  \\    /   O peration     | Version:  2.3.0                                 |
|   \\  /    A nd           | Web:      www.OpenFOAM.com                      |
|    \\/     M anipulation  |                                                 |
\*---------------------------------------------------------------------------*/
FoamFile
{
    version     2.0;
    format      ascii;
    class       volVectorField;
    location    "0";
    object      U;
}
// * * * * * * * * * * * * * * * * * * * * * * * * * * * * * * * * * * * * * //
#include "../flowVelocity";
#include "../fV";

dimensions      [0 1 -1 0 0 0 0];

internalField   uniform $flowVelocity;

boundaryField
{
    BOTTOM
    {
        type            fixedValue;
        value           $internalField;
    }
    TOP
    {
        type            fixedValue;
        value           $internalField;
    }
    OUTLET
    {
        type            outletPhaseMeanVelocity;
        alpha           alpha.water;
        Umean           $fV;
        value           $internalField;
    }
    FARPS
    {
        type            fixedValue;
        value           $internalField;
    }
    INLET
    {
        type            fixedValue;
        value           $internalField;
    }
    SYM
    {
        type            symmetryPlane;
    }
    SHIP
    {
        type            uniformFixedValue;
        uniformValue    tableFile;
        tableFileCoeffs
        {
         fileName       "URamp"
         outOfBounds    clamp;
        }
}

// ************************************************************************* //
```

Figure 8.7: Velocity set-up. A time varying boundary condition at the vessel resembles a steady acceleration until the desired speed was achieved as defined in the *URamp* file.

Constant Directory

The *constant* directory includes files specifying the time independent simulation parameters. These include:

- *dynamicMeshDict*
- *g*
- *RASProperties*
- *transportProperties*
- *turbulenceProperties*

```
/*--------------------------------*- C++ -*----------------------------------*\
| =========                 |                                                 |
| \\      /  F ield         | OpenFOAM: The Open Source CFD Toolbox           |
|  \\    /   O peration     | Version:  2.3.0                                 |
|   \\  /    A nd           | Web:      www.OpenFOAM.org                      |
|    \\/     M anipulation  |                                                 |
\*---------------------------------------------------------------------------*/
FoamFile
{
    version     2.0;
    format      ascii;
    class       dictionary;
    object      dynamicMeshDict;
}
// * * * * * * * * * * * * * * * * * * * * * * * * * * * * * * * * * * * * * //
#include "../mass"
#include "polyMesh/pointDisplSquat"

dynamicFvMesh       dynamicMotionSolverFvMesh;

motionSolverLibs    ("libsixDoFRigidBodyMotion.so");

solver              sixDoFRigidBodyMotion;

sixDoFRigidBodyMotionCoeffs
{
    patches         (SHIP);
    innerDistance   0.5;
    outerDistance   2;

    centreOfMass    $centreOfMass;
    mass            $mass;
    momentOfInertia $momOfInertia;
    rhoInf          1;
    report          on;
    accelerationRelaxation 0.3;
    value           uniform (0 0 0);

    constraints
    {
        zAxis
        {
            sixDoFRigidBodyMotionConstraint line;
            direction     (0 0 1);
        }
        yPlane
        {
            sixDoFRigidBodyMotionConstraint axis;
            axis          (0 1 0);
        }
    }

    restraints
    {
        translationDamper
        {
            sixDoFRigidBodyMotionRestraint linearDamper;
            coeff         5000;
        }
        rotationDamper
        {
             axis            (0 1 0);
             stiffness       0;
             damping         5000;

            sixDoFRigidBodyMotionRestraint linearAxialAngularSpring;
    }

}


//* ************************************************************************* //
```

Figure 8.8: Set-up for mesh motion restraints and constraints.

```
/*--------------------------------*- C++ -*----------------------------------*\
| =========                 |                                                 |
| \\      /  F ield         | OpenFOAM: The Open Source CFD Toolbox           |
|  \\    /   O peration     | Version:  2.3.0                                 |
|   \\  /    A nd           | Web:      www.OpenFOAM.com                      |
|    \\/     M anipulation  |                                                 |
\*---------------------------------------------------------------------------*/
FoamFile
{
    version     2.0;
    format      ascii;
    class       uniformDimensionedVectorField;
    location    "constant";
    object      g;
}
// * * * * * * * * * * * * * * * * * * * * * * * * * * * * * * * * * * * * * //

dimensions      [0 1 -2 0 0 0 0];
value           ( 0 0 -9.81 );


// ************************************************************************* //
```

Figure 8.9: Set-up for gravitational acceleration.

```
/*--------------------------------*- C++ -*----------------------------------*\
| =========                 |                                                 |
| \\      /  F ield         | OpenFOAM: The Open Source CFD Toolbox           |
|  \\    /   O peration     | Version:  1.5                                   |
|   \\  /    A nd           | Web:      http://www.OpenFOAM.org               |
|    \\/     M anipulation  |                                                 |
\*---------------------------------------------------------------------------*/
FoamFile
{
    version     2.0;
    format      ascii;
    class       dictionary;
    object      RASProperties;
}
// * * * * * * * * * * * * * * * * * * * * * * * * * * * * * * * * * * * * * //

RASModel            kOmegaSST;

turbulence          on;

printCoeffs         on;

// ************************************************************************* //
```

Figure 8.10: Set-up for turbulence properties using a Reynolds-Averaged Stress model.

```
/*--------------------------------*- C++ -*----------------------------------*\
| =========                 |                                                 |
| \\      /  F ield         | OpenFOAM: The Open Source CFD Toolbox           |
|  \\    /   O peration     | Version:  2.3.0                                 |
|   \\  /    A nd           | Web:      www.OpenFOAM.org                      |
|    \\/     M anipulation  |                                                 |
\*---------------------------------------------------------------------------*/
FoamFile
{
    version     2.0;
    format      ascii;
    class       dictionary;
    location    "constant";
    object      transportProperties;
}
// * * * * * * * * * * * * * * * * * * * * * * * * * * * * * * * * * * * * * //
#include "../flowVelocity"
phases (water air);

water
{
    transportModel  Newtonian;
    nu              nu [ 0 2 -1 0 0 0 0 ]  $nu;
    rho             rho [ 1 -3 0 0 0 0 0 ] 1000;
}

air
{
    transportModel  Newtonian;
    nu              nu [ 0 2 -1 0 0 0 0 ]  1.48e-05;
    rho             rho [ 1 -3 0 0 0 0 0 ] 1;
}

sigma           sigma [ 1 0 -2 0 0 0 0 ] 0;

// ************************************************************************* //
```

Figure 8.11: Set-up for fluid properties.

```
/*--------------------------------*- C++ -*----------------------------------*\
| =========                 |                                                 |
| \\      /  F ield         | OpenFOAM: The Open Source CFD Toolbox           |
|  \\    /   O peration     | Version:  2.3.0                                 |
|   \\  /    A nd           | Web:      www.openfoam.com                      |
|    \\/     M anipulation  |                                                 |
\*---------------------------------------------------------------------------*/
FoamFile
{
    version     2.0;
    format      ascii;
    class       dictionary;
    object      RASProperties;
}
// * * * * * * * * * * * * * * * * * * * * * * * * * * * * * * * * * * * * * //
simulationType      RASModel;

// ************************************************************************* //
```

Figure 8.12: Set-up for turbulence properties.

System Directory

The *system* directory includes the following files specifying the main simulation parameters.

- *controlDict*
- *fvSchemes*
- *fvSolution*

```
/*--------------------------------*- C++ -*----------------------------------*\
| =========                 |                                                 |
| \\      /  F ield         | OpenFOAM: The Open Source CFD Toolbox           |
|  \\    /   O peration     | Version:  2.3.0                                 |
|   \\  /    A nd           | Web:      www.OpenFOAM.org                      |
|    \\/     M anipulation  |                                                 |
\*---------------------------------------------------------------------------*/
FoamFile
{
 class dictionary;
 format ascii;
 object controlDict;
 version 2.0;
}
#include "../endTime"

application interDyMFoam;

startFrom latestTime;
startTime 0;
stopAt endTime;
endTime $eT;
deltaT $dT;

writeControl adjustableRunTime;
writeInterval 0.5;
purgeWrite 2;
writeFormat ascii;
writePrecision 6;
writeCompression uncompressed;

timeFormat general;
timePrecision 9;
runTimeModifiable yes;
adjustTimeStep no ;//

maxCo 8.0;
maxAlphaCo 9.0;

functions
  {
    forces

    {
      type forces;
      functionObjectLibs
        (
          "libforces.so"
        );
      patches
        (
          SHIP
        );
      rhoInf 1000.0;
      CofR (1.25 0 0);
      outputControl timeStep;
      outputInterval 10;
      log true;
    }
  }

libs
(
    "libOpenFOAM.so"
    "libincompressibleRASModels.so"
    "libfvMotionSolvers.so"
    "libforces.so"
);
```

Figure 8.13: Set-up for control parameters.

```
/*--------------------------------*- C++ -*----------------------------------*\
| =========                 |                                                 |
| \\      /  F ield         | OpenFOAM: The Open Source CFD Toolbox           |
|  \\    /   O peration     | Version:  2.3.0                                 |
|   \\  /    A nd           | Web:      www.OpenFOAM.org                      |
|    \\/     M anipulation  |                                                 |
\*---------------------------------------------------------------------------*/
FoamFile
{
    version     2.0;
    format      ascii;
    class       dictionary;
    location    "system";
    object      fvSchemes;
}
// * * * * * * * * * * * * * * * * * * * * * * * * * * * * * * * * * * * * * //

ddtSchemes
{
    default         Euler;
}

gradSchemes
{
    default         Gauss linear;
}

divSchemes
{
    div(rhoPhi,U)  Gauss vanLeerV;
    div(phi,alpha)  Gauss vanLeer;
    div(phirb,alpha) Gauss linear;
    div(phi,k)      Gauss upwind;
    div(phi,omega) Gauss upwind;
    div((muEff*dev(T(grad(U))))) Gauss linear;
}

laplacianSchemes
{
    default         Gauss linear corrected;
}

interpolationSchemes
{
    default         linear;
}

snGradSchemes
{
    default         corrected;
}

fluxRequired
{
    default         no;
    p_rgh;
    pcorr;
    alpha.water;
}


// ************************************************************************* //
```

Figure 8.14: Specification of solvers.

```
/*--------------------------------*- C++ -*----------------------------------*\
| =========                 |                                                 |
| \\      /  F ield         | OpenFOAM: The Open Source CFD Toolbox           |
|  \\    /   O peration     | Version:  2.3.0                                 |
|   \\  /    A nd           | Web:      www.OpenFOAM.org                      |
|    \\/     M anipulation  |                                                 |
\*---------------------------------------------------------------------------*/
FoamFile
{
    version     2.0;
    format      ascii;
    class       dictionary;
    location    "system";
    object      fvSolution;
}
// * * * * * * * * * * * * * * * * * * * * * * * * * * * * * * * * * * * * //

solvers
{
    "alpha.water.*"
    {
        nAlphaCorr      3;
        nAlphaSubCycles 3;
        cAlpha          1;
        icAlpha         0;

        alphaOuterCorrectors  yes;

        MULESCorr       yes;
        nLimiterIter    10;
        alphaApplyPrevCorr  yes;

        solver          smoothSolver;
        smoother        symGaussSeidel;
        tolerance       1e-10;
        relTol          0;
        minIter         1;
    }

    "pcorr.*"
    {
        solver          GAMG;

        smoother        DIC;
        agglomerator    faceAreaPair;
        mergeLevels     1;
        nCellsInCoarsestLevel 10;
        cacheAgglomeration true;

        tolerance       0.1;
        relTol          0;
    };

    p_rgh
    {
        solver          GAMG;

        smoother        DIC;
        agglomerator    faceAreaPair;
        mergeLevels     1;
        nCellsInCoarsestLevel 10;
        cacheAgglomeration true;

        tolerance       5e-8;
        relTol          0.001;
    };

    p_rghFinal
    {
        $p_rgh;
        relTol          0;
    }
```

Figure 8.15: Set-up for solver parameters 1/2.

```
    "(U|k|omega).*"
    {
        solver          smoothSolver;

        smoother        symGaussSeidel;
        nSweeps         1;

        tolerance       1e-7;
        relTol          0;
        minIter         1;
    };
}

PIMPLE
{
    momentumPredictor no;

    nOuterCorrectors 1;
    nCorrectors      3;
    nNonOrthogonalCorrectors 0;

    correctPhi      yes;
    moveMeshOuterCorrectors yes;
    turbOnFinalIterOnly yes;
}

relaxationFactors
{
    fields
    {
    }
    equations
    {
        ".*" 1;
    }
}

cache
{
    grad(U);
}


// ************************************************************************* //
```

Figure 8.16: Set-up for solver parameters 2/2.

Bibliography

Armstrong, T. (2003). "The Effects of Demihull Separation on the Frictional Resistnce of Catamarans". In: *Proceedings of 7th International Conference on Fast Sea Transportation*. Ischia, Italy, pp. 47–56.

Armstrong, T. and T. Clark (2009). "On the Effect of Hull Shape on the Performance of Some Existing High-Speed Ferries". In: *Proceedings of 10th International Conference on Fast Sea Transportation*. Athens, Greece, pp. 21–32.

Austal (2011). *Commercial Products: Ferries - Vehicle/Passenger*. www.austal.com.

Bailey, D. (1976). *The NPL High-Speed Round Bilge Displacement Hull Series*. Vol. No. 4. Royal Institution of Naval Architects.

Banawan, A. A., M. Mosleh, and I. S. Seddiek (2013). "Prediction of the Fuel Saving and Emissions Reduction by Decreasing Speed of a Catamaran". In: *Journal of Marine Engineering and Technology* 12.3, pp. 40–48.

Bertram, V. (2000). *Practical Ship Hydrodynamics*. Butterworth-Heinemann.

Bhushan, S., T. Xing, and F. Stern (2012). "Vortical Structures and Instability Analysis for Athena Wetted Transom Flow with Full-scale Validation". In: *Journal of Fluids Engineering* 134.3, 031201:1–031201:12.

Broglia, R., B. Jacob, S. Zaghi, F. Stern, and A. Olivieri (2014). "Experimental Investigation of Interference Effects for High-speed Catamarans". In: *Ocean Engineering* 76, pp. 75–85.

Bucher, J. (2014). "Calm Water Pitch Motions of Large Medium-speed Catamarans". BEng Thesis. Launceston Australia: Australian Maritime College.

Bulten, N. W. H. (2006). "Numerical Analysis of Waterjet Propulsion System". PhD thesis. Eindhoven University of Technology.

Caprio, F. and C. Pensa (2007). "Experimental Investigation on two Displacement Catamarans: Systematic Variation of Displacement, Clearance and Stagger". In: *Transaction oo the Royal Institution of Naval Architects - Part B1: International Journal of Small Craft Technology* 149, pp. 23–32.

Cusanelli, D. S. (2011). "Hydrodynamic and Supportive Structure for Gated Ship Sterns - Amphibious Ship Stern Flap". In: *Proceedings of the 11th International Conference on Fast Sea Transportation*. Honolulu, Hawaii, US.

Davidson, G., T. R. Roberts, S. Friezer, G. Thomas, N. Bose, M. R. Davis, and R. Verbeek (2011a). "130 m Wave Piercer Catamaran: A New Energy Efficient Multihull Operating at Critical Speeds". In: *Proceedings of 9th International RINA Conference on High Speed Marine Vehicles*. Naples, Italy, pp. 61–72.

Davidson, G., T. R. Roberts, S. Friezer, M. R. Davis, N. Bose, G. Thomas, J. Binns, and R. Verbeek (2011b). "Maximising Efficiency and Minimising Cost in High Speed Craft". In: *International Conference on Fast Sea Transportation*. Vol. 11. Honolulu, US, pp. 727–734.

Day, A. H., D. Clelland, and L. J. Doctors (2009). "Unsteady Finite-Depth Effects During Resistance Tests on a Ship Model in a Towing Tank". In: *Journal of Marine Science and Technology* 14.3, pp. 387–397.

de Cock, J., T. van Beck, L. Muilwijk, R. Verbeek, and J. Poelmann (2011). "Wärtsilä Waterjets Offer Powerful and Versatile Propulsion Solutions ". In: *Wärtsilä Technical Journal*.

Doctors, L. J. (1993). "The Influence of Demihull Separation and Riverbanks on the Resistance of a Catamaran". In: *Proceedings of 2nd International Conference on Fast Sea Transportation*. Yokohama, Japan, pp. 1231–1244.

Doctors, L. J., G. J. Macfarlane, and R. Young (2007). "A Study of Transom-Stern Ventilation". In: *International Shipbuilding Progress* 54.2, pp. 135–145.

Dubrovsky, V. A. and A. G. Lyakhovitsky (2001). *Multi Hull Ships*. Backbone Publishing Company.

Eca, L. and M. Hoekstra (2008). "The Numerical Friction Line". In: *Marine Science and Technology* 13, pp. 328–345.

Eggers, K. (1955). "Über die Widerstandsverhältnisse von Zweikörperschiffen (in German)". In: *STG Jahrbuch*. Julius Springer Verlag, pp. 516–537.

Eslamdoost, A., L. Larsson, and R. Bensow (2015). "On Transom Clearance". In: *Ocean Engineering* 99, pp. 55–62.

Everest, J. T. (1968). "Some Research on the Hydrodynamics of Catamarans and Multi-Hulled Vessels in Calm Water". In: *Transaction of NECI* 84, pp. 129–148.

Faltinsen, O. M. (2005). *Hydrodynamics of High-speed Marine Vehicles*. Cambridge University Press.

Froude, W. (1874). *On Experiments with H.M.S. Greyhound*. Royal Institution of Naval Architects.

Fry, E. D. and T. Graul (1972). "Design and Application of High-Speed Catamarans". In: *Marine Technology*, pp. 345–357.

Gee, N. (2008). "The Fast and the Furious". In: *Ship and Boat International* Diamond Jubilee, pp. 10–12.

Gorski, J., S. Turnock, B. Allesandrini, H. Chun, U. Hollenbach, T. Mikkola, Y. Tahara, J. Valle, and L. Ying (2011). *The Resistance Committee - Final Report and Recommendations to the 26th ITTC*. Tech. rep.

Griggs, D. and E. Woo (2005). *HSV-2 SWIFT Combined Standardization and Powering Trials Results*. Tech. rep. Naval Surface Warfare Center, Carderock Division.

Grigson, C. W. B. (1999). "A Planar Friction Algorithm And Its Use In Analysing Hull Resistance". In: *Transactions RINA*, pp. 76–115.

Guiard, T., S. Leonard, and F. Mewis (2013). "The Becker Mewis Duct: Challenges in Full-Scale Design and New Developments for Fast Ships". In: *Proceedings of the 3rd International Symposium on Marine Propulsor*. Launceston, Australia, pp. 519–527.

Guldhammer, H. E. and S. A. Harvald (1965). *Ship Resistance. Effect on Form and Principal Dimensions*. Copenhagen: Akademisk Forlarg.

Haase, M., S. Winkler, R. Bronsart, and N. Kornev (2011). "Experimental Validation of Viscous Free Surface Flow Computation Around Fast NPL Catamarans at Large Drift Angles". In: *Proceedings of 1st International Symposium on Naval Architecture and Maritime*. Istanbul, Turkey, pp. 1–13.

Haase, M., F. Iliopulos, G. Davidson, S. Friezer, G. Thomas, J. Binns, N. Bose, J. Lavroff, and M. R. Davis (2012a). "Application of RANSE Based Simulations for Resistance Prediction of Medium-speed Catamarans at Different Scales". In: *Proceedings of 18th Australasian Fluid Mechanics Conference*. Launceston, Australia, p. 270.

Haase, M., G. Davidson, G. Thomas, J. Binns, and N. Bose (2012b). "On the Design and Resistance Prediction of Large Medium-Speed Catamarans". In: *Proceeding of International Conference on High-Performance Vehicles*. Duisburg, Germany, pp. 78–89.

Haase, M., G. Davidson, S. Friezer, J. Binns, G. Thomas, and N. Bose (2012c). "On the Macro Hydrodynamic Design of Highly Efficient Medium-speed Catamarans with Minimum Resistance". In: *Transaction of the Royal Institution of Naval Architects, Part A - International Journal of Maritime Engineering* 154.A3, pp. 131–142.

Haase, M., J. Binns, G. Thomas, and N. Bose (2012d). "Resistance Prediction of Medium-speed Catamarans Using Free-surface Viscous Flow Simulations". In: *15th Numerical Towing Tank Symposium*. Cortona, Italy, pp. 1–6.

Haase, M., G. Davidson, J. Binns, G. Thomas, and N. Bose (2013). "Practical Design Aproach and Resistance Prediction of Large Medium-speed Catamarans". In: *Ship Technology Research / Schiffstechnik* 60, pp. 4–12.

– (2015a). "Full-Scale Resistance Prediction in Finite Waters A Study Using CFD Simulation, Model Test Experiments and Sea Trial Measurements". In: *Proceedings of the Institution of Mechanical Engineers, Part M: Journal of Engineering for the Maritime Environment* under review.

Haase, M., G. Davidson, S. Friezer, J. Binns, G. Thomas, and N. Bose (2015b). "Full-Scale Simulation-based Hull Form Design of Large Medium-speed Catramarans with High Fuel

Efficiency". In: *Proceedings of the 13th International Conference on Fast Sea Transportation*. Washington, D.C., US.

Haase, M., G. Davidson, S. Friezer, J. Binns, G. Thomas, and N. Bose (2015c). "Hydrodynamic Hull Form Design Space Exploration of Large Medium-Speed Catamarans Using Full-Scale CFD". In: *Transaction of the Royal Institution of Naval Architects, Part A - International Journal of Maritime Engineering* 157.A3, pp. 161–174.

– (2015d). "Maximising Transport Efficiency by Utilising Full-Scale CFD for the Initial Ship Design Process Validation and Application for Large Catamarans". In: *Proceedings of International Maritime Conference PACIFIC*. Vol. I. Sydney, Australia.

Haase, M., K. Zürcher, G. Davidson, J. Binns, G. Thomas, and N. Bose (2015e). "Novel CFD-Based Full-Scale Resistance Prediction for Large Medium-Speed Catamarans". In: *Ocean Engineering* under review.

Haase, M., J. Binns, G. Thomas, and N. Bose (2015f). "Wave-piercing Catamaran Transom Stern Ventilation Process". In: *Ship Technology Research / Schiffstechnik* in press.

Hadler, J. B., J. L. Kleist, and M. L. Unger (2007). "On the Effect of Transom Area on the Resistance of Hi-Speed Monohulls". In: *Proceedings of 9th International Conference on Fast Sea Transportation*. Shanghai, China, pp. 176–183.

Hadler, J. B., K. M. Cain, and E. M. Singleton (2009). "On the Effect of Transom Area on the Resistance of high-Speed Catamaran Hulls". In: *Proceedings of 10th International Conference on Fast Sea Transportation*. Athens, Greece, pp. 573–588.

Havelock, T. H. (1949). "The Wave Resisitance of a Cylinder Started from Rest". In: *Oxford University Press*.

He, W., T. Castiglione, M. Kandasamy, and F. Stern (2011). "URANS Simulations of Catamaran Interference". In: *Proceedings of the 11th International Conference on Fast Sea Transportation*. Honolulu, US, pp. 145–152.

Hendrickson, K., G. Weymouth, S. Banerjee, and D. K. P. Yue (2013). "Air Entrainment and Multiphase Turbulence in the Bubbly Wake of a Transom Stern". In: *International Shipbuilding Progress* 60.1, pp. 375–401.

Hochkirch, K. and B. Mallol (2013). "On the Importance of Full-Scale CFD Simulations for Ships". In: *International Conference on Computer Applications and Information Technology in Maritime Industries*. Cortona, Italy, pp. 85–95.

Hughes, G. (1954). "Friction And Form Resistance In Turbulent Flow And A Proposed Formulation For Use In Model And Ship Correlation". In: *RINA* 96, pp. 314–376.

Iliopulos, F., J. Lavroff, M. R. Davis, J. Binns, G. Davidson, and R. Verbeek (2013). "Validation for Full Scale RANSE Simulation of Resistance Prediction for High Speed Catamarans". In: *Proceedings of the 12th International Conference on Fast Sea Transportation*. Amsterdam, The Netherlands, pp. 1–8.

Incat (2011). *Fleet*. INCAT website: www.incat.com.au.

Insel, M. (1990). "An Investigation into the Resistance Components of High Speed Catamarans". PhD thesis. Department of Ship Science, University of Southampton, UK.

Insel, M. and A. F. Molland (1991). "An Investigation Into the Resistace Components of High Speed Displacement Catamarans". In: *Transaction of the Royal Institution of Naval Architects, Part A - International Journal of Maritime Engineering* 134, pp. 1–20.

Itabashi, M. and R. Michida (2001). "Performance of SSTH-70 after Delivery and Future of SSTH". In: *Japan Papers for 24th US Japan Cooperative Program in Natural Resources*.

Jensen, G. (1994). "Handbuch der Werften XXII: Moderne Schiffslinien (in German), Hansa". In:

Katsui, T., H. Asai, Y. Himeno, and Y. Tahara (2005). "The Proposal of a New Friction Line". In: *5th Osaka Colloquium on Advanced CFD Applications to Ship Flow and Hull Form Design*. Japan, pp. 76–83.

Kiss, T. K. and R. H. Compton (1989). "The Effects of Transom Geometry on the Resisitance of Large Surface Combatants". In: *Transactions SNAME* 97.

Kouh, J. S., Y. J. Chen, and S. W. Chau (2009). "Numerical Study on Scale Effect of Form Factor". In: *Ocean Engineering* 36, pp. 403–413.

Lafeber, F. H., R. Hulshof, J. H. Allema, and J. H. de Jong (2008). *Calm Water Test for the JHSV Wave Piercing Catamaran Final Report*. Tech. rep. MARIN.

Lazauskas, L. and E. O. Tuck (1996). *Small, Low Drag, Solar-Powered Monohulls and Multihulls*. Tech. rep. The University of Adelaide, Dept. Applied Mathematics.

Lewis, E. V., ed. (1988). *Resistance, Propulsion and Vibration*. Principals of Naval Architecture. Society of Naval Architects and Marine Engineers.

Lin, C. W. and S. Percival (2001). "Free Surface Viscous Flow Computation Around a Transom Stern Ship by Chimera Overlapping Scheme". In: *Proceedings of 23rd Symposium on Naval Hydrodynamics*. Val de Reuil, France, pp. 171–183.

Lingwood, J. (1996). *Significant Ships*. Royal Institution of Naval Architects. ISBN: 9780903055239.

Maki, K. J. (2005). "Transom Stern Hydrodynamics". PhD thesis. University of Michigan.

Maki, K. J., L. J. Doctors, R. F. Beck, and A. W. Troesch (2006). "Transom-stern Flow for High-speed Craft". In: *Australian Journal of Mechanical Engineering* 3.2, pp. 191–199.

Martinez de Oses, F. X. and M. La Castalls (2005). "High Speed Craft Viability Analysis". In: *Journal of Maritime Research* II.3, pp. 59–76.

Matsubara, S. (2011). "Ship Motions and Wave-Induced Loads on High Speed Catamarans". PhD thesis. University of Tasmania.

Matsui, S. (1993). "The Experimental Investigations on Resistance and Seakeeping Qualities of High-Speed Catamarans". In: *Proceedings of 2nd International Conference on Fast Sea Transportation*. Yokohama, Japan, pp. 1245–1255.

McKesson, C., Remley B., and Z. Karni (2000). "Ferry Environmental Impact". In: *Canadian Institute of Marine Engineers High Performance Vehicles Conference*. Institute of Marine Engineers.

Michel, W. H. (1961). "The Sea-going Catamaran Ship and its Features and its Feasibility". In: *International Shipbuilding Progress* 8, pp. 390–401.

Millward, A. (1992). "The Effects of Hull Separation and Restricted Water Depth on Catamaran Resistance". In: *RINA Transactions*, pp. 341–349.

Miyata, H., H. Nogami, M. Shirai, and Y. Shirose (1991). "Fast Ferry by Super-slender Twin Hull". In: *Proceedings of High-Speed Marine Transportation - International Maritime Shipping Conference*. Sydney, Australia, pp. 23–27.

Miyazawa, M. (1979). "A Study on the Flow around a Catamaran". In: *Journal of the Society of Naval Architects of Japan* Vol. 145, pp. 26–53.

Molland, A. F. and A. R. Lee (1995). *Resistance Experiments on as Series of High Speed Displacement Catamarans Forms: Variation of Prismatic Coefficient*. Tech. rep. University of Southampton.

Molland, A. F., J. F. Wellicome, and P. R. Couser (1994). *Resistance Experiments on as Series of High Speed Displacement Catamarans Forms: Variation of Length-Displacement Ratio and Breadth-Draught Ratio*. Tech. rep. 71. University of Southampton.

Murdijanto, K. Utama, and A. Jamaluddin (2011). "An Investigation into the Resistance/Powering and Seakeeping Characteristics of River Catamaran and Trimaran". In: *Makara, Teknologi* 15.1.

O'Dea, J., D. Jenkins, and T. Nagle (1981). *Flow Characteristics of a Transom Stern Ship*. Tech. rep. 81/1057. David W. Taylor Naval Ship Research and Development Center.

Oura, T. and Y. Ikeda (2008). "Manoeuvrability of a Wavepiercing High-Speed Catamaran at Low Speed in Strong Wind". In: *Proceedings of International Conference on Marine Research and Transportation*. Italy, pp. 17–20.

Oving, A. J. (1985). *Resistance Prediction Method for Semi-Planing Catamarans with Symmetrical Demihulls*. Tech. rep. MARIN.

Psaraftis, H. N., C. A. Kontovas, and N. M. Kakalis (2009). "Speed Reduction as an Emission Reduction Measure for Fast Ships". In: *Proceedings of the 10th International Conference on Fast Sea Transportation*.

Raven, H. C., A. van der Ploeg, A. R Starke, and L. Eca (2008). "Towards a CFD-based Prediction of Ship Performance - Progress in Predicting Full-scale Resistance and Scale Effects". In: *Proceedings of RINA International Conference Marine CFD*, pp. 31–42.

Rawson, K. J. and E. C. Tupper (2001). *Basic Ship Theory*. Butterworth-Heinemann.

Robards, S. and L. J. Doctors (2003). "Transom-Hollow Prediction for High-Speed Displacement Vessels". In: *Proceedings of 7th International Conference on Fast Sea Transportation*. Ischia, Italy, A1.19–A1.26.

Rovere, J. E. (1997). "Catamaran Resistance from Tests on a Single Demihull". In: *Proceedings of 4th International Conference on Fast Sea Transportation*. Sydney, Australia, pp. 737–741.

Sahoo, P. K., S. Mason, and A. Tuite (2008). "Practical Evaluation of Resistance of High-speed Catamaran Hull FormsPart II". In: *Ships and Offshore Structures* 3.3, pp. 239–245.

Salas, M., R. Luco, P. K. Sahoo, N. Browne, and M. Lopez (2004). "Experimental and CFD Resistance Calculation of a Small Fast Catamaran". In: *Proceeding of International Conference on High-Performance Marine Vehicles*. Rome, Italy.

Sato, R., H. Nogami, Y. Shirose, A. Ito, H. Miyata, K. Masaoka, E. Kamal, and Y. Tsuchiya (1991). "Hydrodynamic Design of Fast Ferries by the Concept of Super-Slender Twin Hull". In: *Proceedings of 1st International Conference on Fast Sea Transportation*. Trondheim, Norway, pp. 523–528.

Saunders, H. E. (1957). *Hydrodynamics for Ship Design*. Society of Naval Architects and Marine Engineers.

Schlichting, H. (1979). *Boundary Layer Theory*. McGraw-Hill.

Schneekluth, H. and V. Bertram (1998). *Ship Design for Efficiency and Economy*. Butterworth-Heinemann.

Schuster, S. (1956). "Beitrag zur Frage der Kanalkorrektur bei Modellversuchen (in German)". In: *Schiffstechnik*, pp. 93–96.

Sireli, M. E., Insel M., and Ö. Gören (2000). "The Effect of Transom Stern on the Resistance of High Speed Craft". In: *IX. Congress International Maritime Association of Mediterranean*. Vol. I. Ischia, Italy, A40–A47.

Söding, H. (1997). "Drastic Resitance Reduction in Catamarans by Staggered Hulls". In: *Proceedings of 4th International Conference on Fast Sea Transportation*. Sydney, Australia, pp. 225–230.

Souto-Iglesias, A., D. Fernandez-Gutierrez, and L. Perez-Rojas (2012). "Experimental Assessment of Interference Resistance for a Series 60 Catamaran in Free and Fixed Trim-sinkage Conditions". In: *Ocean Engineering* 53.

Starke, A. R, H. C. Raven, and A. van der Ploeg (2007). "Computation of Transom-stern Flows using a Steady Free-surface Fitting RANS Method". In: *Proceeding of 9th International Conference on Numerical Ship Hydrodynamics*. Ann Abour, US.

Stern, F., J. Yang, Z. Wang, M. Sadat-Hosseini, S. Bhushan, and T. Xing (2013). "Computational Ship Hydrodynamics: Nowadays and Way Forward". In: *International Shipbuilding Progress* 60, pp. 3–105.

Tamura, K. (1972). "Study of the Blockage Correction". In: *Journal of the Society of Naval Architects of Japan* 131, pp. 17–28.

Tapia, X. P. (2009). "Modelling of Wind Flow Over Complex Terrain using OpenFoam". MA thesis. University of Gävle.

Tasaki, R. (1962). *A Note on Wavemaking Resistance of Catamarans*. Tech. rep. University of Michigan, Ann Abour, MI.

Taylor, W. D. (1943). *The Speed and Power of Ships*. United States Maritime Commission.

Thomas, G., P. Tomic, and A. Tuite (2007). "High-speed Catamaran or Monohull? How Do You Choose?" In: *Ships and Offshore Structures*, pp. 137–147.

Trillo, R. L. (1991). "High Speed over Water, Ideas from the Past, the Present and for the Future". In: *Proceedings of 1st International Conference on Fast Sea Transportation*. Trondhein, Norway, pp. 17–34.

Tuck, E. O. and L. Lazauskas (1998). "Optimum Hull Spacing of a Family of Multihulls". In: *Ship Technology Research* 45, pp. 180–195.

Tupper, E.C. (2004). *Introduction to Naval Architecture: Formerly Muckle's Naval Architecture for Marine Engineers*. Elsevier Science.

Turner, H. and A. Taplin (1968). "The Resistance of Large Powered Catamarans". In: *SNAME Transactions* 76, pp. 180–203.

Utama, K., .A Jamaluddin, and W. Aryawan (2012). "Experimental Investigation into ihe Drag Interference of Symmetrical and Asymmetrical Staggered and Unstaggered Catamarans". In: *Journal of Ocean Technology* 7.1, pp. 48–58.

Vollheim, R. (1968). "Über Formgebung und Widerstand von Katamaranen (in German)". In: *Schiffbauforschung* 7.

Walker, J. M., M. P. Schultz, and K. A. Flack (2014). "Skin-friction Drag Measurements on Ship Hull Coating Systems". In: *Proceedings of 30th Symposium on Naval Hydrodynamics*. Hobart, Australia.

Wehausen, J. V. (1964). "Effect of the Initial Acceleration Upon the Wave Resistance of Ship Models". In: *Journal of Ship Research* 7.3, pp. 38–50.

White, F. M. (2003). *Fluid Mechanics*. McGraw-Hill Education - Europe.

Wilson, R. V., P. M. Carrica, and F. Stern (2006). "URANS Simulations for a High-speed Transom Stern Ship with Breaking Waves". In: *International Journal of Computational Fluid Dynamics* 20.2, pp. 105–125.

Wyatt, D., T. Fu, G. Taylor, E. Terrill, T. Xing, S. Bhushan, T. O'Shea, and D. Dommermuth (2008). "Comparison of Full-scale Experimental Measurements and Computational Predictions of the Transom-stern Wave of the R/V Athena". In: *Proceedings of 27th Symposium on Naval Hydrodynamics*. Seoul, Korea.

Yeung, R. and H. Wan (2008). "Multihull and Surface-Effect Ship Configuration Design: A Framework for Powering Minimization". In: *Journal of Offshore Mechanics and Arctic Engineering* 130.

Yun, L. and A. Bliault (2010). *High Performance Marine Vehicles*. Springer.

Zaghi, S., R. Broglia, and A. Di Mascio (2011). "Analysis of the InterferenceEffects for High-speed Catamarans by Model Tests and Numerical Simulations". In: *Ocean Engineering* 38, pp. 2110–2122.

Zürcher, K. (2015). "Waterjet Testing Techniques for Powering Performance Estimation using a Single Catamaran Demihull". PhD thesis. University of Tasmania.

Zürcher, K., N. Bose, J. Binns, G. Thomas, and G. Davidson (2013). "Design and Commissioning Tests for Waterjet Self-Propulsion Testing of a MediumSpeed Catamaran Ferry using a Single Demihull". In: *Proceedings of the 3rd International Symposium on Marine Propulsor*. Launceston, Australia, pp. 97–103.